Biomaterials for In Vivo Genome Editing and Endovascular Embolization

by

Ruosen Xie

The dissertation is submitted in partial fulfillment of
the requirements for the degree of

Doctor of Philosophy
(Materials Science and Engineering)

at the
University of Wisconsin-Madison
2021

Date of final oral examination: 08/23/2021

The dissertation was approved by the following members of the Final Oral Committee:

Shaoqin Sarah Gong, Professor, Department of Biomedical Engineering
Weibo Cai, Professor, Department of Radiology
Xudong Wang, Professor, Department of Materials Science and Engineering
Wendy C. Crone, Professor, Department of Biomedical Engineering
Glen S. Kwon, Professor, School of Pharmacy

Abstract

Biomaterials play a key role for many biomedical applications. In this dissertation, two types of biomaterials were developed. One is a self-assembled polymeric nanoparticle that can deliver CRISPR-Cas9 for in vivo genome editing for the treatment of various genetic diseases (e.g., Duchenne muscular dystrophy, **Chapter 2**). The other is an injectable dual-crosslinking network (DCN) hydrogel capable of endovascular embolization for the treatment of vascular abnormalities (e.g., abdominal aortic aneurysm, **Chapter 3**).

CRISPR-Cas9 may offer new therapeutics for genetic diseases through gene disruption via nonhomologous end joining (NHEJ) or gene correction via homology-directed repair (HDR). However, clinical transition of CRISPR technology is limited by a lack of safe and efficient delivery systems. Here, we report facilely fabricated pH-responsive polymer nanoparticles capable of safely and efficiently delivering Cas9 ribonucleoprotein alone (termed NHEJ-NP, diameter = 29.4 nm), or together with donor DNA (termed HDR-NP, diameter = 33.3 nm). Moreover, intravenously and intramuscularly injected NHEJ-NP induced efficient gene editing in mouse liver and skeletal muscle, respectively. Intramuscularly injected HDR-NP also led to muscle strength recovery in a Duchenne muscular dystrophy mouse model. NHEJ-NP and HDR-NP possess many desirable properties including high payload loading content, small and uniform sizes, high editing efficiency, good biocompatibility, low immunogenicity, and ease of production, storage, and transport, making them great interest for various genome editing applications with clinical potentials.

Vascular embolization provides an effective approach for the treatment of hemorrhage, aneurysms, and other vascular abnormalities. However, current embolic materials, such as metallic coils and

liquid embolic agents, are limited by their inability to provide safe, consistent, and controlled embolization. Here, we report an injectable hydrogel that can remain at the injection site and subsequently undergo in situ covalent crosslinking, leading to the formation of a dual-crosslinking network (DCN) hydrogel for endovascular embolization. The DCN hydrogel is simple to prepare, easy to deploy via needles and catheters, and mechanically stable at the target injection site thereby avoiding embolization of non-target vessels. It possesses efficient hemostatic activity and good biocompatibility. The DCN hydrogel is also clearly visible under X-ray imaging, thereby allowing for targeted embolization. In vivo tests in a rabbit artery model demonstrates that The DCN hydrogel is effective in achieving immediate embolization of the target artery with long-term occlusion by inducing luminal fibrosis. Collectively, the DCN hydrogel provides a viable, biocompatible, and cost-effective alternative to existing embolic materials with clinical translation potential for endovascular embolization.

Acknowledgements

First, I would like to express my sincere and deep gratitude to my advisor, Dr. Shaoqin Sarah Gong, for her willingness to offer me a precious opportunity to study and work in her research group, for her invaluable supervision, support and tutelage throughout my entire PhD life, for her patience, encouragement and trust every time when I was struggling, for her inspiring conversations and guidance for my projects, for her thoughtful considerations and insightful suggestions for my career, and for her extraordinary efforts in maintaining a wonderful academic environment in our research group. There is no doubt that without her mentorship, it would be impossible for me to complete my PhD study.

I would like to thank all my committee members, Dr. Weibo Cai, Dr. Xudong Wang, Dr. Wendy Crone, and Dr. Glen Kwon. I am very grateful for their insightful guidance for my research and constructive comments and suggestions for my presentations and dissertation.

I would also like to thank all my collaborators, Dr. Dai Yamanouchi, Dr. Yu-Chung Chen, Dr. Zhenqiang Ma, Dr. David Gamm, Dr. Nihal Ahmad, Dr. Masatoshi Suzuki, Dr. David McCulley, Dr. Amr Abdeen, Dr. Yei Hwan Lee, Dr. Juhwan Lee, Mr. Inkyu Lee, Mr. Seunghwan Min, Dr. Gagan Chhabra, and Ms. Mary Ndiaye for their tremendous contribution to my projects.

I would also like to thank all my former and current colleagues in Dr. Gong's research group, Dr. Yuyuan Wang, Dr. Xiuxiu Wang, Dr. Mingzhou Ye, Dr. Yi Zhao, Dr. Ying Zhang, Ms. Nisakorn Yodsanit, Mr. Min Zhu, Ms. Yao Tong, Mr. Jingcheng Zhu, Dr. Xianghui Xu, Dr. Guojun Chen, Dr. Qifeng Zheng, Dr. Ben Ma, Dr. Liming Fang, Dr. Min Wu, and Mr. Joseph Kraft for their kind guidance, support, assistance, and encouragement.

Particularly, I would like to thank Dr. Xiuxiu Wang, Dr. Yuyuan Wang, Dr. Mingzhou Ye, and

Dr. Yi Zhao for their contribution to the work presented in Chapter 2. I would also like to thank Dr. Yu-Chung Chen (Kawasumi Laboratories, Inc.), Dr. Yi Zhao, Ms. Nisakorn Yodsanit, Dr. Yuyuan Wang, Mr. Naoaki Yamamoto (Kawasumi Laboratories, Inc.), and Dr. Dai Yamanouchi (UW-Madison) for their contribution to the work presented in Chapter 3.

I would also like to thank the University of Wisconsin-Madison, the Wisconsin Institute for Discovery, the Department of Materials Science and Engineering at UW-Madison, the National Institutes of Health (NIH), and Kawasumi Laboratories, Inc. (Japan).

I would also like to thank my friends both in the US and in China, especially Mr. Jinrong Ma, Mr. Chuanhong Liu, Dr. Han Xiao, and Dr. Jianhai Yang.

Finally, I would like to dedicate my PhD dissertation to my mother, Ms. Yongheng Shao, my grandfather, Mr. Weiti Shao, my girlfriend, Ms. Zhaoyi Ren, and other family members.

Table of Contents

List of Figures

List of Tables

Chapter 1. Introduction

Biomaterials have been instrumental for various biomedical applications. In this dissertation, two types of biomaterials were developed. In **Chapter 2**, a self-assembled polymeric nanoparticle that can deliver CRISPR-Cas9 for in vivo genome editing for the treatment of various genetic diseases (e.g., Duchenne muscular dystrophy). In **Chapter 3**, an injectable dual-crosslinking network (DCN) hydrogel capable of endovascular embolization for the treatment of vascular abnormalities (e.g., abdominal aortic aneurysm).

The CRISPR (clustered regularly interspaced short palindromic repeat)-Cas9 (CRISPR-associated protein 9) system is a powerful genome editing tool which can lead to new therapeutic strategies for genetic diseases [1-4]. Guided by a single-guide RNA (sgRNA), Cas9 nuclease induces a double-strand DNA break at the target locus in the genome. Cells try to repair the double-strand DNA break via a number of pathways including nonhomologous end joining (NHEJ), homology-directed repair (HDR), and less frequently, microhomology-mediated end joining (MMEJ) and single-strand annealing (SSA) [4-7]. Gene disruption via NHEJ and gene correction via HDR are of great interest and in high demand as potential therapeutics for genetic diseases. Non-viral delivery of Cas9 ribonucleoprotein (RNP) for NHEJ or Cas9 RNP plus the donor DNA for HDR is preferable for in vivo genome editing because Cas9 RNP does not rely on transcription or translation machinery and thus provides high catalytic activity, low off-target effects, low risk of insertional mutagenesis, and ease of production and storage [8]. However, while a number of non-viral vectors have been developed for Cas9 RNP delivery in recent years [8-14], to date, few non-viral nanoplatforms have been developed for co-delivery of these payloads [15-20]. Moreover, the non-viral vectors reported previously typically require a laborious fabrication and purification

process, which complicates their clinical translation. We thus sought to develop a new nanosystem that only requires a single component and a simple process to produce, meanwhile provides well-defined morphology, safe and efficient delivery capability for in vitro and in vivo gene editing applications.

Endovascular embolization has been a standard of care and well-established technique to treat internal bleeding, aneurysm, and vascular malformation, in which an occlusive material or agent is delivered into the target vessel through the catheter [21, 22]. Solid embolic materials (e.g., metallic coils) are effective in controlled and precise deployment into the target vessel [23, 24]. However, it is difficult to achieve complete thrombosis of the vessel, and it requires lengthy and costly procedures for embolization of large vessels and aneurysms [25]. Complications can occur after embolization with metallic coils, including coil migration and coil compaction. In contrast to solid embolic materials, liquid embolic materials (e.g., Onyx^{TM}) can quickly induce thrombosis of the target vessel, occlude large vessels and arteriovenous malformations and manage endoleak during or after endovascular aortic aneurysm repair (EVAR) [26-29]. However, liquid embolic materials are difficult to deploy in a controlled manner. They may incidentally embolize non-targeted vessels [30], and/or cause dangerous entrapment of the delivering catheter which may lead to surgical difficulties [31]. Complications including recanalization and incomplete embolization can happen. To resolve limitations of solid embolic materials and liquid embolic agents, we sought to develop an embolic material that can (1) be deployed via needles or catheters; (2) maintain mechanical stability and integrity and remain at the injection site after deployment; (3) rapidly induce blood coagulation and thrombosis; (4) gradually induce fibrosis for permanent embolization and tissue regeneration; (5) allow visibility during endovascular surgery by X-ray imaging for target deployment; and (6) possess good biocompatibility. One type of materials that

are of particular interest for our design criteria is hydrogel. Injectable hydrogels and in situ gelling hydrogels formed by liquid precursors can potentially fulfill these requirements, taking advantages of their tunable viscoelastic nature and chemical versatility. Up to date, several hydrogel systems have been reported for endovascular embolization [25, 32-37]. However, previously reported hydrogel systems still have room to improve to fulfill clinical requirements. Hydrogels that are formed in situ typically require two respective injections or a double-lumen syringe to administrate liquid hydrogel precursors, which can complicate the deployment process and induce undesirable off-target embolization. Hydrogels formed only by physical interactions for crosslinking are less reliable than the ones with covalently crosslinked structures in terms of mechanical stability for long-term embolization. Additionally, embolization that relies on tissue fibrosis instead of physical occlusion by embolic materials is more desirable for permanent embolization and tissue regeneration.

Chapter 2. pH-Responsive Polymer Nanoparticles for Efficient Delivery of Cas9 Ribonucleoprotein With or Without Donor DNA

2.1 Introduction

The CRISPR (clustered regularly interspaced short palindromic repeat)-Cas9 (CRISPR-associated protein 9) system is a powerful genome editing tool for genetic manipulation, which can lead to new therapeutic strategies for genetic diseases [1-4]. The Cas9 ribonucleoprotein (RNP), consisting of a Cas9 nuclease in complex with a single-guide RNA (sgRNA), induces a double-strand DNA break at the target locus in the genome. Cells can repair the double-strand DNA break via multiple pathways including nonhomologous end joining (NHEJ), homology-directed repair (HDR), and other pathways such as microhomology-mediated end joining (MMEJ) and single-strand annealing (SSA) [4-7]. NHEJ induces small insertions or deletions to permanently silence the gene that causes diseases. HDR occurs when a donor DNA template is present and it can precisely correct the gene mutations to their wild-type sequences [4, 15]. Gene disruption via NHEJ and gene correction via HDR are thus of great interest and in high demand as therapeutics for genetic diseases.

Non-viral delivery of Cas9 RNP for NHEJ or Cas9 RNP plus the donor DNA for HDR is preferable for in vivo genome editing because Cas9 RNP does not rely on transcription or translation machinery and thus provides high catalytic activity, low off-target effects, low risk of insertional mutagenesis, and ease of production and storage [8]. However, although non-viral vectors have been developed for Cas9 RNP delivery in recent years [8-14], to date, few non-viral nanoplatforms have been developed for co-delivery of these payloads [15-20]. This can be attributed to the different physical natures of Cas9 RNP and donor DNA both in terms of morphology and surface

charge. Moreover, the non-viral vectors reported previously typically require a laborious fabrication and purification process. This complicates their clinical translation. We thus sought to develop a new nanosystem that only requires a single component and a simple process to produce, meanwhile provides well-defined morphology, safe and efficient delivery capability for in vitro and in vivo gene editing applications.

Anionic charges on sgRNA can shield cationic charges on Cas9 nuclease, and thus Cas9 RNP exhibits a negative net charge. We and others found that when complexing Cas9 nucleases and sgRNAs in a molar ratio of Cas9/sgRNA > 1, the negatively charged Cas9 RNP and positively charged Cas9 nuclease (without sgRNA) aggregated quickly leading to sedimentation (**Figure 2.6c**) [38]. This phenomenon is attributed to the charge neutralization between the anionic Cas9 RNP and the cationic Cas9 nuclease, leading to increased hydrophobicity of the complex. Furthermore, a number of hydrophobic amino acids including phenylalanine, proline, leucine are present on the *Streptococcus pyogenes* Cas9 nuclease surface (**Figure 2.6a**) [39]. We hypothesized that these hydrophobic moieties on the Cas9 nuclease surface can be employed for complexation with hydrophobic polymers via hydrophobic interactions. Meanwhile, the anionic sgRNA (i.e., the exposed sgRNA portions after binding to Cas9 nuclease) and donor DNA (i.e., single-strand oligonucleotides, ssODN) can be complexed with cationic polymers through electrostatic interactions. We further hypothesized that by utilizing both types of interactions, we would be able to address the heterogeneity of hydrophobicity (or hydrophilicity) and charges within the Cas9 RNP, and between Cas9 RNP and ssODN, to encapsulate these payloads in a non-viral vector. Therefore, we sought to use a pH-responsive amphiphilic polymer that carries both hydrophobic and cationic groups. The tertiary amine group is a good candidate, because depending on the pH conditions, it can become more hydrophobic when being deprotonated, or more cationic when

being protonated, a desirable property for this application. Moreover, tweaking the extent of hydrophobicity and cationic charge density of the polymer by varying pH would allow the same polymer to deliver either Cas9 RNPs for NHEJ or Cas9 RNPs with ssODNs for HDR.

2.2 Result and Discussion

2.2.1 mPEG-PC7A self-assembled with the Cas9 RNP and the ssODN for delivery.

As a proof of concept, we selected methoxy-poly(ethylene glycol)-*b*-poly(2-(azepan-1-yl)ethyl methacrylate) (mPEG-PC7A), a diblock pH-responsive amphiphilic copolymer with a pKa at ~6.7 (**Figure 2.1a**). At physiological pH, mPEG-PC7A has both protonated and deprotonated tertiary amine groups, and thus the ionizable PC7A block is composed of cationic and hydrophobic side groups [40, 41]. mPEG-PC7A can be synthesized via facile chemical reactions (**Figure 2.7**). mPEG-PC7A efficiently complexes with either Cas9 RNPs (termed as "NHEJ-NP") or Cas9 RNPs with ssODNs (termed as "HDR-NP") to form nanoparticles via a straightforward self-assembly process (**Figure 2.1a**). Upon endocytosis, mPEG-PC7A becomes highly protonated in the acidic endosomal/lysosomal environment at pH 5.5-6.5, converting the hydrophobic PC7A polymer segment to a highly cationic and hydrophilic PC7A segment. This dramatic change in charges and hydrophilicity facilitates the endosomal escape of the payloads via the "proton sponge" effect, the NP disassembly, and the release of the payloads into the cytoplasm. Thereafter, facilitated by the nuclear localization signals (NLS), the NLS-conjugated Cas9 RNP and the ssODN can enter the cell nucleus for genome editing via NHEJ or HDR (**Figure 2.1b**).

Transmission electron microscopy (TEM) and dynamic light scattering (DLS) revealed well-defined spherical NP shape and average hydrodynamic diameters of 29.4 nm (PDI of 0.18) and 33.3 nm (PDI of 0.21) for NHEJ-NP and HDR-NP, respectively (**Figure 2.1c, d**). NHEJ-NP and

HDR-NP with zeta-potentials at +0.2 and -0.3 mV suggested the surface charge of payloads (i.e., Cas9 RNPs and ssODNs) were completely shielded, demonstrating efficient payload encapsulation and the formation of NPs (**Figure 2.1f**). Gel electrophoresis further verified payload encapsulation (**Figure 2.1e**), where no observable band migration was found from both types of NPs, in strong contrast to the naked payloads. To determine the interactions between the polymer and Cas9 RNP, Tween 20, NaCl, and urea were mixed with NHEJ-NP, and the size variations of NHEJ-NP were monitored by DLS [42]. As shown in **Figure 2.1g**, the size of NHEJ-NP in the presence of Tween 20 was reduced from 28.8 nm to 8.5 nm after one hour, suggesting rapid and complete NP dissociation attributed to competitive hydrophobic interactions. NHEJ-NP swelled in the NaCl solution over time and increased to 80 nm after 24 h, indicating that electrostatic interaction plays a role in the formation of NHEJ-NP. In contrast, urea, which disturbs hydrogen bonding, did not cause any significant size change. These results support our hypothesis that the interaction between mPEG-PC7A and Cas9 RNPs is a combination of hydrophobic and electrostatic interactions.

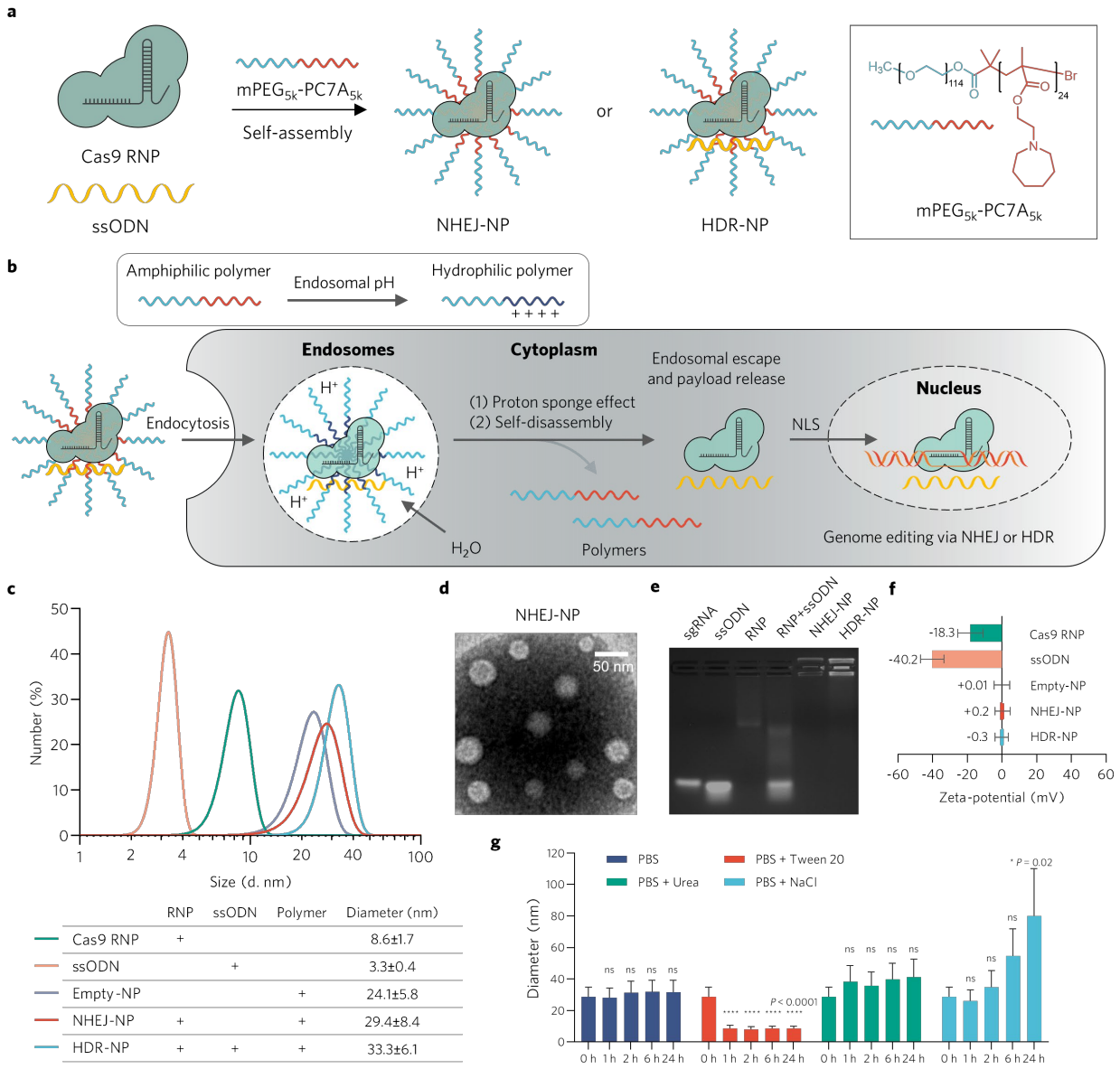

	RNP	ssODN	Polymer	Diameter (nm)
Cas9 RNP	+			8.6±1.7
ssODN		+		3.3±0.4
Empty-NP			+	24.1±5.8
NHEJ-NP	+		+	29.4±8.4
HDR-NP	+	+	+	33.3±6.1

Figure 2.1 | Design and characterization of NHEJ-NP and HDR-NP.

a, The pH-sensitive mPEG-PC7A polymer forms nanoparticle (NP), through a self-assembly process, with either Cas9 RNP alone to enable genome editing via NHEJ (termed NHEJ-NP), or with both Cas9 RNP and ssODN (a donor DNA) to enable genome editing via HDR (termed HDR-NP). **b,** NPs are taken up by cells typically via an endocytosis process. The PC7A polymer segments become protonated in the acidic endosomal compartments, thereby triggering the

disassembly of the NPs, and enabling the release and endosomal escape of the payload, and ultimately its delivery to the cytoplasm. Thereafter, the Cas9 RNP or Cas9 RNP with ssODN enters the nucleus, facilitated by NLS presented on Cas9, for genome editing. **c,** The hydrodynamic diameters of Cas9 RNP, ssODN, empty-NP, NHEJ-NP, and HDR-NP were measured by DLS. Data are presented as mean ± s.d. **d,** A representative TEM image of NHEJ-NP. Scale bar: 50 nm. **e,** Zeta-potentials of the Cas9 RNP, ssODN, empty-NP, NHEJ-NP, and HDR-NP indicate that the anionic charges of Cas9 RNP and ssODN were neutralized after being encapsulated inside the NPs. Data are presented as mean ± s.d. **f,** An electrophoresis assay in 2% agarose gel for sgRNA, ssODN, Cas9 RNP, Cas9 RNP with ssODN, NHEJ-NP, and HDR-NP indicates efficient complexation between the payloads (i.e., Cas9 RNP for Cas9 RNP with ssODN) and mPEG-PC7A. **g,** The size of NHEJ-NP varied in the PBS solution containing either Tween 20 (red) or NaCl (light blue), but remained stable in the PBS solution (dark blue) or the PBS solution containing urea (green) at 37 ^{o}C. This study demonstrates that NHEJ-NP was formed by both hydrophobic and electrostatic interactions between the polymer and the Cas9 RNP. Data are presented as mean ± s.d. Statistical significance with the size of fresh NHEJ-NP was calculated via one-way ANOVA with Tukey's post hoc test. *$P < 0.05$, **$P < 0.01$, ***$P < 0.001$, ****$P < 0.0001$. ns, not significant. NLS, nuclear localization signal.

2.2.2 NHEJ-NP and HDR-NP delivered genome editors and edited human cells in vitro via NHEJ and HDR.

The formulations of NHEJ-NP were first optimized using green fluorescent protein (GFP) expressing human embryonic kidney cells (GFP-HEK293), where successful gene disruption leads

to silence of GFP expression and can be detected by flow cytometry. We hypothesized that the degree of protonation for the tertiary amine groups in the polymer is crucial to encapsulate the Cas9 RNP as they are cationic and hydrophilic when protonated and hydrophobic when deprotonated. As a matter of fact, the pH value for nanoparticle formation plays a key role in delivery efficiency. A series of NHEJ-NPs were prepared at different pH values and used to treat the cells (**Figure 2.2a**). NHEJ-NP formed at pH 8.0 exhibited comparable gene editing efficiency with Lipofectamine 2000. NHEJ-NPs formed at pH < 8.0 showed lower editing efficiencies, likely due to poor nanoparticle stability resulting from insufficient hydrophobic interactions between the polymer and Cas9 RNP. Similarly, NHEJ-NPs prepared at pH > 8.0 had lower gene editing efficiencies, likely due to lower RNP encapsulation efficiency resulting from insufficient cationic charges of the PC7A polymer at a higher pH (hence a higher degree of deprotonation). Additionally, a series of NHEJ-NPs with different polymer/Cas9 RNP weight ratios were prepared in order to optimize the loading content (LC) of NHEJ-NP. Higher polymer/Cas9 RNP ratio led to less band migration in gel electrophoresis, suggesting more efficient encapsulation (**Figure 2.8b**). Based on this study, considering both genome editing efficiency and payload loading content, polymer/Cas9 RNP ratio at 5/1 (LC% = 17%) was selected as our final formulation for further studies.

The formulation and editing efficiency of HDR-NPs were evaluated using blue fluorescent protein (BFP) expressing HEK293 (BFP-HEK293) cells. BFP-HEK293 cells contain a missense Y66H mutation of GFP. Therefore, gene correction via HDR (correcting CAT to TAC) leads to GFP expression and gene disruption via NHEJ leads to silence of BFP expression. The HDR and NHEJ efficiency can be thus quantified by flow cytometry. Similar to NHEJ-NP, an optimal pH value was determined for the HDR-NP preparation (**Figure 2.2b**). HDR-NP formed at pH 7.0 exhibited a significantly higher HDR efficiency than Lipofectamine 2000, as measured by flow cytometry.

As expected, the optimal pH for preparing HDR-NP was lower than the one for NHEJ-NP because ssODNs, 100-nt oligonucleotides bearing anionic charges, require more cationic (protonated) groups in the polymer to form stable HDR-NP. Notably, the HDR/NHEJ ratio induced by HDR-NP at pH of 7.0 (i.e., HDR/NHEJ = 1.1) was about 1.8-fold higher than that of Lipofectamine 2000 (i.e., HDR/NHEJ = 0.6), likely owing to more efficient codelivery of Cas9 RNP and ssODN at the same time (**Figure 2.9a**). The optimal molar ratio of ssODN to Cas9 RNP was confirmed at 1/1, demonstrating the unbiased encapsulation of both payloads by HDR-NP under the optimal preparation condition (**Figure 2.9f**). In terms of cell viability, neither NHEJ-NP nor HDR-NP exhibited cytotoxicity at their working concentration (12.5 μg/mL) in HEK293 cells, whereas Lipofectamine 2000 and Lipofectamine CRISPRMAX both showed significant cytotoxicity at the dosage used to deliver the same amount of the payload (**Figure 2.2d**).

To demonstrate the capability of HDR-NPs in editing hard-to-transfect cells and the versatility of ligand conjugation to HDR-NP, we functionalized HDR-NP with cell-penetrating peptides (CPPs) (i.e., TAT (47-57)). CPPs were conjugated to the distal end of the PEG through maleimide-thiol coupling reactions (**Figure 2.7d**). CPP-conjugation significantly enhanced (~2-fold) the HDR efficiency of HDR-NP to 7.0% in BFP-expressing human embryonic stem cells (hESCs), as quantified by flow cytometry (**Figure 2.2c**), while Lipofectamine CRISPRMAX can hardly edit hESCs.

The cellular uptake behaviors of NHEJ-NP and CPP-NHEJ-NP in HEK293 cells at various conditions were studied. The gRNA used to form Cas9 RNP was fluorescently labeled by Atto 550, so the cellular uptake of NHEJ-NP and CPP-NHEJ-NP can be quantified by flow cytometry. To investigate the cellular uptake mechanism, we treated HEK293 cells with NHEJ-NP and CPP-NHEJ-NP respectively, with or without the presence of a series of endocytosis inhibitors at 37 ºC,

or incubation at 4 ºC (**Figure 2.2e**). Chlorpromazine and wortmannin, both of which inhibit clathrin-mediated endocytosis, significantly reduced the cellular uptake of NHEJ-NP. Genistein, an inhibitor for caveolae-mediated endocytosis, and methyl-β-cyclodextrin, a molecule that depletes cholesterol and thus limits cell membrane fluidity, or incubation at 4 ºC, a temperature at which energy-dependent endocytosis is inhibited, also significantly reduced the cellular uptake of NHEJ-NP. This indicates that NHEJ-NP were taken up by cells via both clathrin- and caveolae-mediated endocytosis. However, the cellular uptake of CPP-NHEJ-NP was reduced ~30% when cells were incubated at 4 ºC alone or treated with methyl-β-cyclodextrin at 37 ºC, indicating that CPP conjugation altered the cellular uptake from endocytosis pathways to primary endocytosis-independent pathways [10, 43]. Furthermore, the subcellular localization of the Cas9 RNP delivered by NHEJ-NP in HEK293 cells was studied by confocal laser scanning microscopy (CLSM, **Figure 2.2f**). It was found that Atto 550-labeled Cas9 RNPs (red fluorescence) could escape from endosomes/lysosomes (green fluorescence) barely 0.5 h after the treatment. More RNPs were found in the cytosol, not overlapping with endosomes/lysosomes, 2 h, and 4 h post-treatment, suggesting efficient payload escape from endosomes/lysosomes facilitated by the pH-responsive polymer. Nuclear transport of Cas9 RNPs was also visualized by considerable overlapping of Cas9 RNPs (red fluorescence) with cell nuclei (blue fluorescence) at 4 h post-treatment. The CLSM images were then quantitively analyzed to calculate the Pearson correlation coefficient and Mander's overlap coefficient as proof for efficient endosome/lysosome escape and nuclear transport of Cas9 RNPs (**Figure 2.10**) [44, 45]. Collectively, our cellular uptake and subcellular trafficking studies support the mechanism we outlined in **Figure 2.1b**.

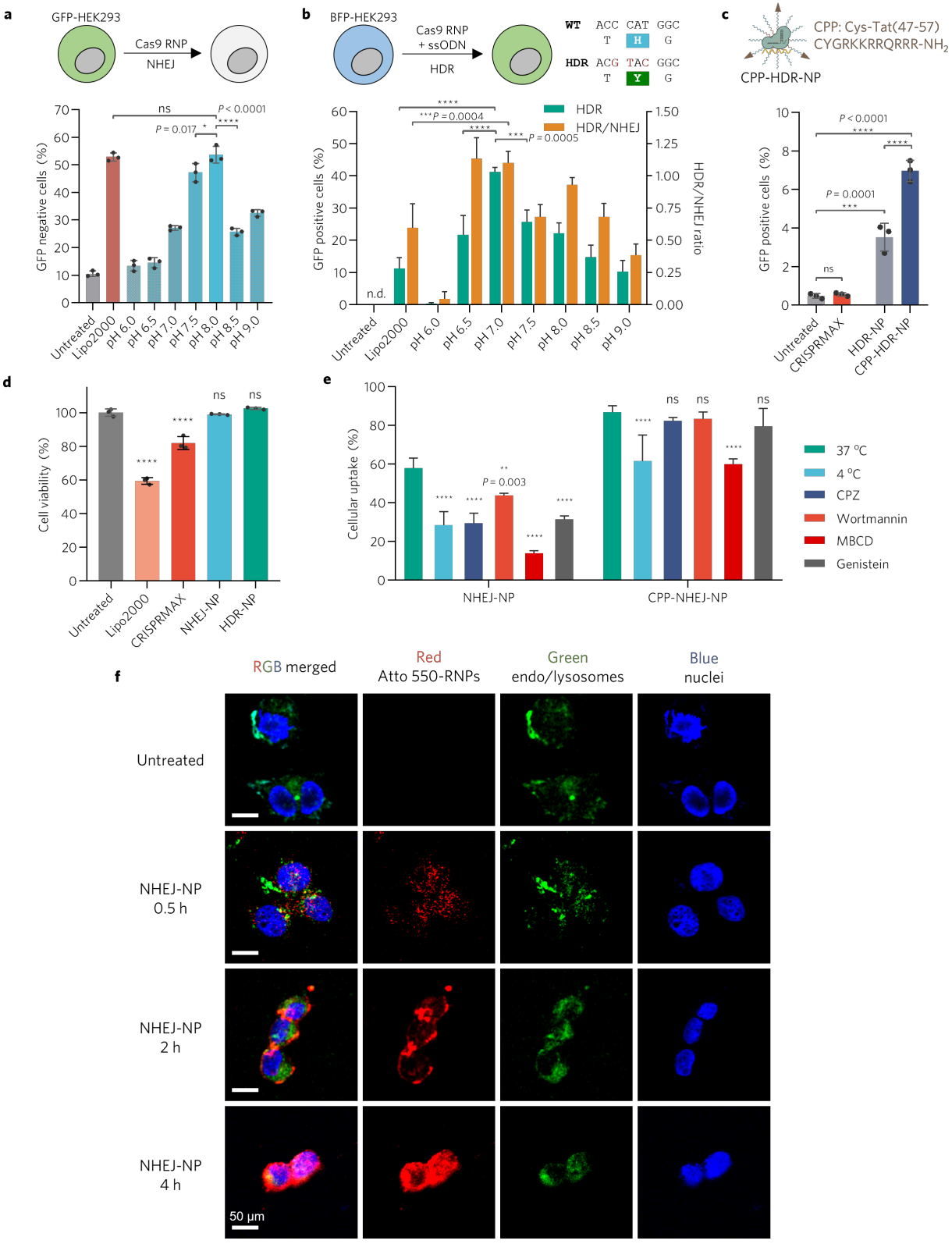

Figure 2.2 | In vitro studies for NHEJ-NPs and HDR-NPs.

a, Optimization of the pH value for preparation of NHEJ-NP for gene editing in GFP-expressing HEK293 cells. Four days after the treatment, the loss of GFP fluorescence was measured by flow cytometry to assay the editing efficiency via NHEJ. Data are presented as mean ± s.d. (n=3). **b,** Optimization of the pH value for preparation of the HDR-NP for gene editing in BFP-expressing HEK293 cells. Gene correction via HDR (correcting CAT to TAC) leads to GFP expression, and gene disruption via NHEJ leads to silence of BFP expression. Four days after the treatment, the gain of GFP and loss of BFP fluorescence were measured by flow cytometry to assay the editing efficiency via HDR and NHEJ, respectively. The HDR efficiency and the HDR/NHEJ ratio are shown. Data are presented as mean ± s.d. (n=3). **c,** HDR efficiency of cell-penetrating peptide-conjugated HDR-NPs (i.e., CPP-HDR-NP) in BFP-expressing H9 hESCs. Four days after the treatment, the gain of GFP fluorescence was measured by flow cytometry to assay the editing efficiency via HDR. Data are presented as mean ± s.d. (n=3). **d,** Cell viability study of NHEJ-NP and HDR-NP in HEK293 cells via CCK-8 assay. Data are presented as mean ± s.d. (n=3). **e,** Study of the endocytosis of NHEJ-NP and CPP-NHEJ-NP. HEK293 cells were first treated with various endocytosis inhibitors at 37 ºC or were incubated at 4 ºC. Cas9 RNPs were labeled with Atto 550-gRNAs and then encapsulated in NHEJ-NP or CPP-NHEJ-NP to treat HEK293 cells. Four hours after treatments, the cellular uptake of Cas9 RNP was quantified by flow cytometry measuring Atto 550^{+} cells. Data are presented as mean ± s.d. (n=4). **f,** Intracellular distribution of NHEJ-NP in HEK293 cells was observed by confocal laser scanning microscopy at different time points after treatments. The Cas9 RNP was labeled with Atto 550-gRNA (red). Cells were stained with LysoTracker Green DND-26 (green) and Hoechst 33342 (blue) for endosomes/lysosomes and nuclei, respectively. Experiments were repeated three times and representative images are shown. Scale bar: 50 μm. Data were analyzed by ImageJ. Statistical significance was calculated via one-

way ANOVA with Tukey's post hoc test. *$P < 0.05$, **$P < 0.01$, ***$P < 0.001$, ****$P < 0.0001$. ns, not significant. n.d., not detected. "Lipo2000" represents Lipofectamine 2000. "CRISPRMAX" represents Lipofectamine CRISPRMAX. CPZ, chlorpromazine. MBCD, methyl-β-cyclodextrin.

2.2.3 NHEJ-NP edited mouse livers after intravenous injection.

The in vivo gene editing efficiency of intravenously injected NHEJ-NP was investigated using transgenic Ai14 mice. The genome of the Ai14 mouse contains a *LoxP*-flanked stop cassette that prevents downstream tdTomato expression (**Figure 2.3a**). The stop cassette is composed of three SV40 polyA transcription terminators that can be targeted by Cas9 RNP. Successful gene editing leads to the excision of the SV40 polyA genetic elements and the expression of tdTomato. Therefore, the gene editing efficiency can be evaluated through tdTomato expression, although tdTomato activation requires removal of at least two of the three SV40 polyA repeat sequences and thus underreports the gene editing efficiency [46]. The Ai14 mice were intravenously injected with NHEJ-NP on Day 0, and their major organs and blood were collected on Day 7 (**Figure 2.3b**). NHEJ-NP targeting SV40 polyA sequences induced significant elevation of tdTomato fluorescence in the livers where gene editing happened, as observed by in vivo imaging system (IVIS) before and after tissue homogenization (**Figure 2.3c, Figure 2.11a-c**). To identify the liver cell types that were edited, we stained the primary cells extracted from the treated Ai14 mice and performed flow cytometry study to quantify the tdTomato-positive cells (**Figure 2.3d**). It revealed that NHEJ-NP induced tdTomato expression in hepatocytes (3.3%), Kupffer cells (4.0%), and endothelial cells (5.2%), respectively. Consistent with the flow cytometry data, immunofluorescence staining demonstrated abundant tdTomato expression in all three major types

of cells in the liver (**Figure 2.3e, Figure 2.11d**).

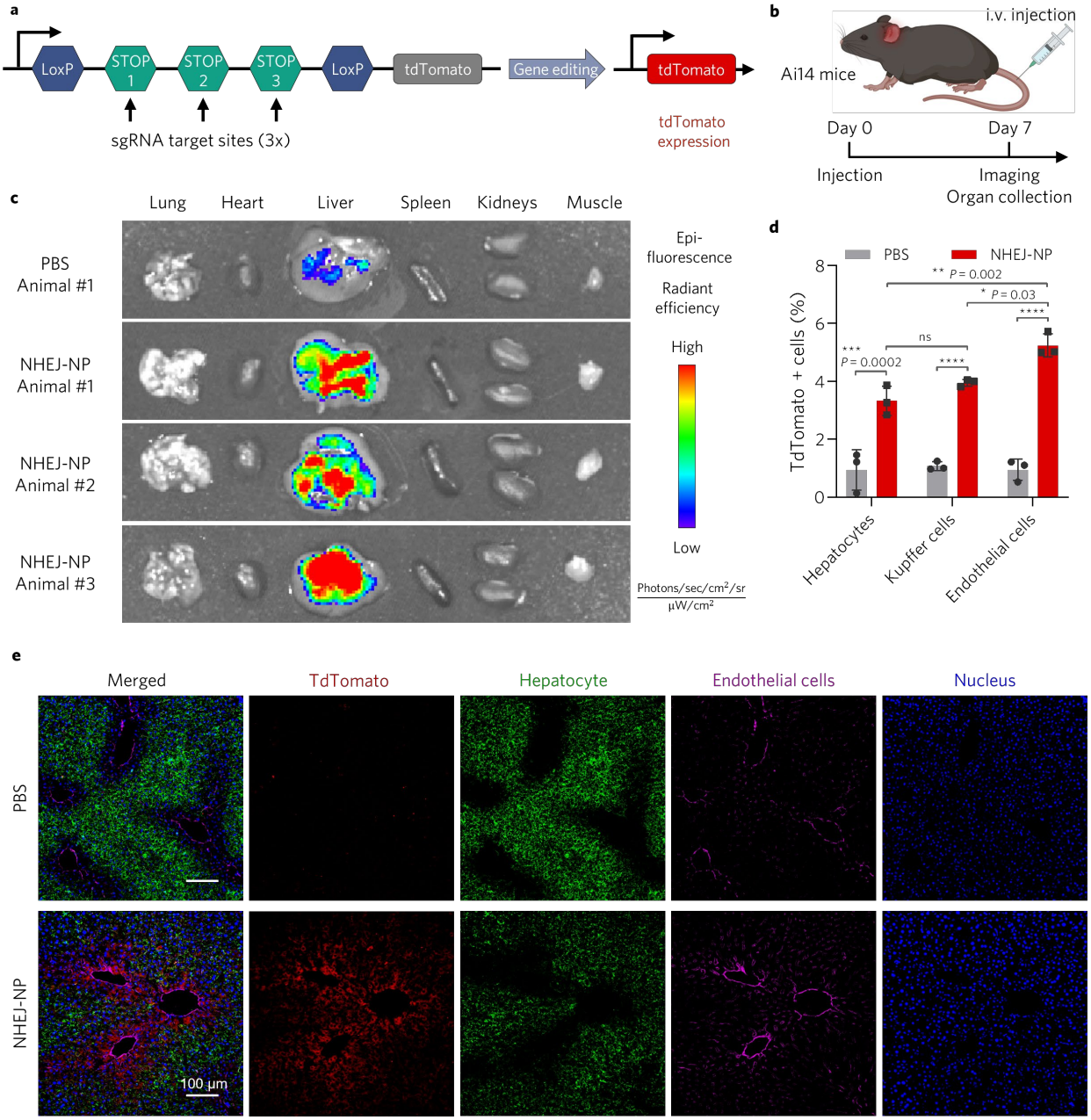

Figure 2.3 | In vivo gene editing with NHEJ-NP in Ai14 reporter mice via intravenous (i.v.) injections.

a, Ai14 mice employ a STOP cassette that consists of three SV40 polyA sequences to prevent transcription of the downstream tdTomato, a red fluorescent protein. Successful gene editing with the Cas9 RNP that targets SV40 polyA sequences leads to excision of the STOP cassette and then the expression of tdTomato, although tdTomato activation requires removal of at least two of the three SV40 polyA repeat sequences and thus underreports the gene editing efficiency. **b,** Ai14 mice were i.v. injected with PBS (n = 3) or NHEJ-NP (n = 3) on Day 0, and the organs and tissues were collected on Day 7 for analysis. **c,** NHEJ-NP selectively edited and induced tdTomato expression in livers after intravenous injection, observed by IVIS. Images acquired from one PBS-injected and three NHEJ-NP-injected mice are presented. **d,** The percentages of tdTomato$^+$ cells within defined cell type populations in liver were quantified by flow cytometry, where tdTomato expression was found in all major cell types in liver. Data are presented as mean ± s.d. (n=3). **e,** Immunofluorescence staining of the liver sections from the PBS-injected and NHEJ-NP-injected mice suggests robust gene editing in liver. Liver sections were stained with anti-RFP antibodies for tdTomato (red), anti-hepatocyte specific antigen (green), anti-CD31 antibodies for endothelial cells (magenta, pseudo-color), and DAPI for nuclei (blue), respectively. Representative images are shown. Scale bar: 100 μm. Statistical significance was calculated via two-way ANOVA with Tukey's post hoc test with PBS group as control. *$P < 0.05$, **$P < 0.01$, ***$P < 0.001$, ****$P < 0.0001$. ns, not significant. IVIS, in vivo imaging systems.

2.2.4 NHEJ-NP edited mouse muscles via intramuscular injection.

The in vivo editing efficiency of NHEJ-NP in skeletal muscles was also investigated using Ai14 mice. For each Ai14 mouse, PBS and NHEJ-NP were intramuscularly injected in its left and right

tibialis anterior muscle, respectively. Tibialis anterior muscles were collected and observed by IVIS to evaluate the fluorescence from tdTomato expression (**Figure 2.4a, b**). In contrast with the PBS-injected muscle from the same mouse, the NHEJ-NP-injected muscle exhibited a considerable amount of tdTomato fluorescence. The editing efficiency was further studied by immunofluorescence staining (**Figure 2.4c, d**). NHEJ-NP led to efficacious tdTomato expression in ~16% of the muscle area, with substantial gene editing induced in myofibers.

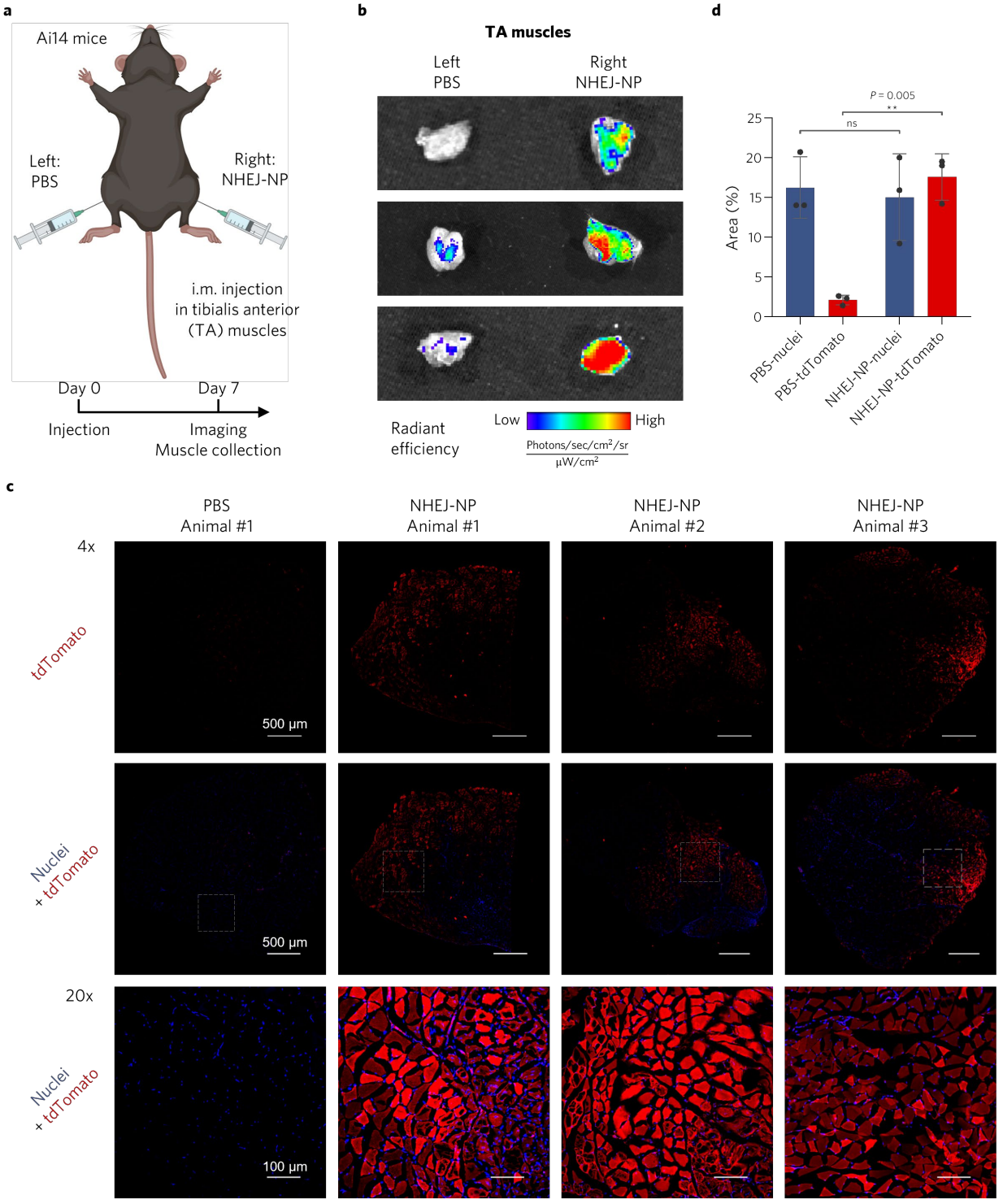

Figure 2.4 | In vivo gene editing with NHEJ-NP in Ai14 reporter mice via intramuscular (i.m.) injections.

a, The Ai14 mouse was i.m. injected with NHEJ-NP in the right side of tibialis anterior (TA) muscle on Day 0. The left side of TA muscle was injected with PBS as control. The muscles were collected on Day 7 for analysis. **b,** NHEJ-NP efficiently edited and induced tdTomato expression in TA muscles after injections. tdTomato fluorescence in TA muscles was measured by IVIS. Images acquired with two magnifications from both the PBS-injected and NHEJ-NP-injected mice are presented (n=3). Scale bar: 500 μm for 4x images and 100 μm for 20x images. **c,** Immunofluorescence staining of the muscle sections from the PBS-injected and NHEJ-NP-injected mice. The muscle sections were stained with anti-RFP antibodies for tdTomato (red) and DAPI for nuclei (blue), respectively. Experiments were repeated three times, and representative images with two magnifications are shown. **d,** Gene editing efficiency was quantified by the percentage area of the whole muscle section with a genome editing reporter (tdTomato+) or nuclei (control), analyzed by ImageJ. Statistical significance was calculated via one-way ANOVA with Tukey's post hoc test. $^{**}P < 0.01$. ns, not significant. IVIS, in vivo imaging systems.

2.2.5 HDR-NPs induced in vivo editing for DMD treatment in *mdx* mice.

Encouraged by the promising gene editing results in Ai14 mice, we conducted experiments to determine the potential of HDR-NPs as a therapeutic strategy for Duchenne muscular dystrophy (DMD), a notorious genetic disease affecting approximately 1 in 3,500 male births [47]. The *mdx* mouse (C57BL/10ScSn-Dmd^{mdx}/J) possesses a nonsense mutation in exon 23 of the *Dmd* gene. Effective gene editing through NHEJ or HDR can disrupt or correct such a point mutation, restore dystrophin expression, and finally improve the muscle strength of the *mdx* mice. HDR-NPs were intramuscularly injected into both sides of the tibialis anterior, gastrocnemius, and triceps brachii

muscles (total 6 injection sites per mouse) of 4-week-old male *mdx* mice, respectively (**Figure 2.5a**). PBS-injected *mdx* mice and untreated wild-type mice were used as the negative and positive control group, respectively. Four-limb hanging tests of the mice were performed to evaluate the therapeutic benefits of HDR-NP. Notably, continuous improvement in muscle strength was observed for the HDR-NP-treated *mdx* mice during the 4-week experiment duration. Such an improvement suggests progressive rescue over time in skeletal muscles after gene editing (**Figure 2.5b, Figure 2.13a-c**). In particular, the HDR-NP-treated *mdx* mice showed 3-fold enhancement of the hanging time in contrast to the PBS-injected *mdx* mice 4 weeks after treatments, with 90% HDR-NP-treated *mdx* mice significantly improving the muscle strength compared with the PBS-injected group, and 45% HDR-NP-treated *mdx* mice performing similarly to wild-type mice (i.e., the hanging time ≥ 10 min). The muscles were harvested for analysis 4 weeks post-treatment. With immunofluorescence staining, robust dystrophin expression was observed in the subsarcolemmal region of myofibers in tibialis anterior, gastrocnemius, and triceps brachii muscles (**Figure 2.5d-f, Figure 2.16-2.18**). The distribution of dystrophin expression within the tibialis anterior muscle was also investigated by sectioning the muscle at different distances from the tendon. Notably, HDR-NP-mediated gene editing led to dystrophin restoration almost throughout the entire tibialis anterior muscle. Considerable dystrophin-positive signals were found in all tibialis anterior muscle sections collected at different distances away from the tendon (**Figure 2.14**). Dystrophin expression was also observed abundantly in most area of the whole section of the HDR-NP-treated tibialis anterior muscle (**Figure 2.15**). This can be attributed to the densely PEGylated NP surface and small NP size (33 nm diameter) that enable efficient diffusion of HDR-NP in the muscle. The pathology of muscle was further studied by trichrome staining (**Figure 2.5g**). HDR-NP-treated *mdx* mouse muscles exhibited less muscle fibrosis and fewer pathological characteristics of

muscular dystrophy, as well as interstitial fibrosis. The restoration of dystrophin expression is attributed to the gene editing on *Dmd* exon 23 via either HDR or NHEJ that corrects or disrupts the nonsense mutation [47]. Sanger sequencing results revealed that 2.6% of HDR and 13.3% of NHEJ were induced by HDR-NPs in the tibialis anterior muscles (**Figure 2.19**). Although HDR-mediated gene correction cannot happen in postmitotic cells (e.g., myofibers) [48], the gene editing via HDR in the muscle can be attributed to HDR that happened in myoblasts which can undergo mitosis. Myoblasts can proliferate and differentiate to myofibers during the muscle growth of mice and the recovery of muscle injuries [15]. Consequently, the corrected gene in myoblasts can finally function in newly generated myofibers to recover dystrophin expression. Collectively, these studies suggest that HDR-NP may offer a promising therapeutic approach to effectively treat DMD.

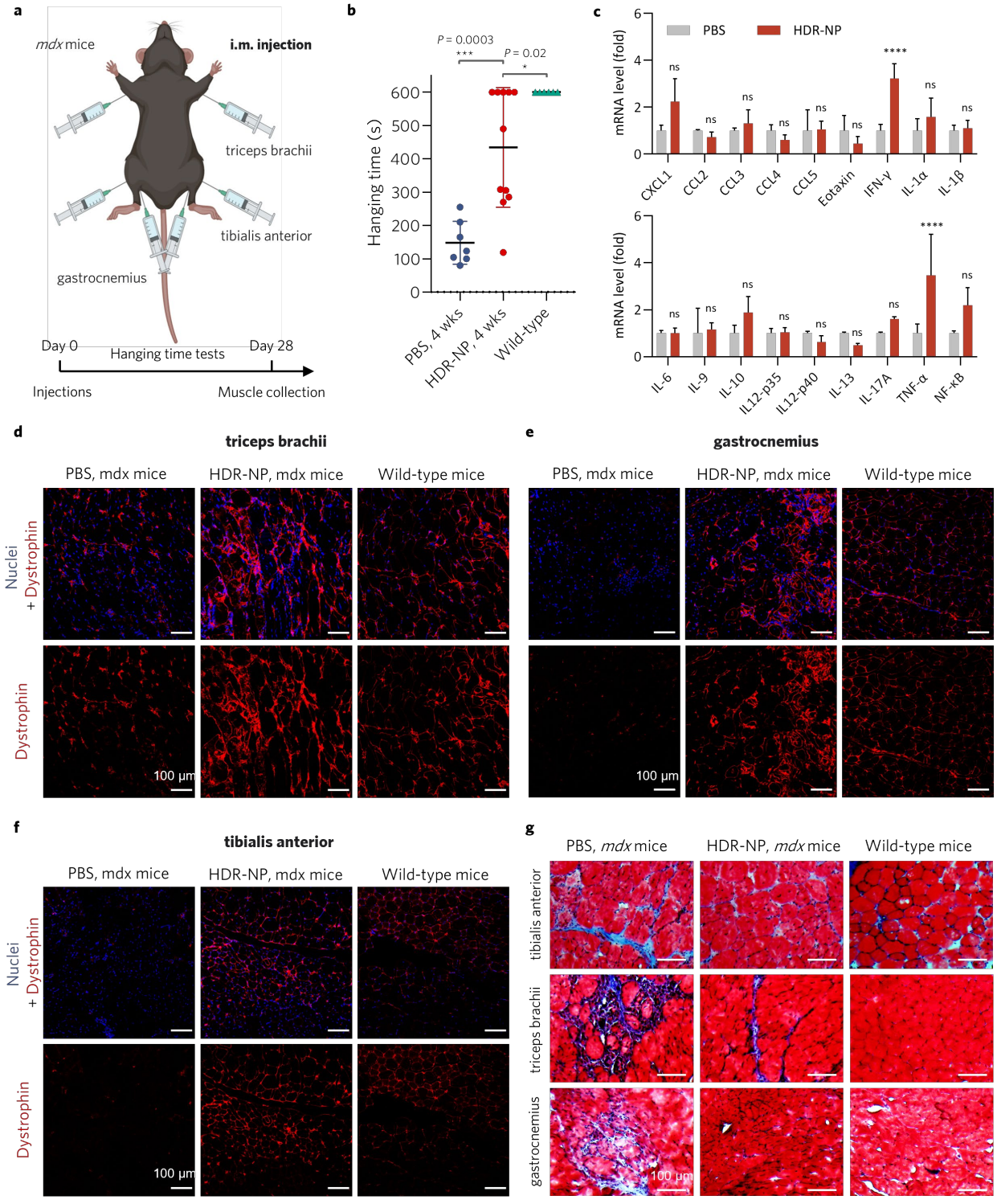

Figure 2.5 | In vivo gene editing with HDR-NP via intramuscular (i.m.) injections for Duchenne muscular dystrophy treatment.

a, The *mdx* mouse was i.m. injected with HDR-NP in triceps brachii, gastrocnemius, and tibialis anterior muscles on Day 0, respectively. Muscles were harvested on Day 28 for analysis. **b,** The four-limb hanging time assay of the PBS-injected mdx mice (n = 7, negative control), HDR-NP-injected mdx mice (n = 11), and untreated wild-type mice (n = 6, positive control) demonstrates the restoration of muscle strength of mdx mice after HDR-NP-mediated gene editing. Data were acquired 28 days after treatments. **c,** Immunogenicity of PBS (as reference) or HDR-NP injection in tibialis anterior muscles of *mdx* mice. Expression levels of cytokines were quantified by RT-PCR. **d-f,** Immunofluorescence staining of (**d**) triceps brachii, (**e**) gastrocnemius, and (**f**) tibialis anterior muscle sections from the PBS-injected and HDR-NP-injected *mdx* mice and untreated wild-type mice. Muscle sections were stained with anti-dystrophin antibodies for dystrophin (red) and DAPI for nuclei (blue), respectively. Results indicate robust restoration of dystrophin expression after HDR-NP treatments. Representative images are presented. Scale bar: 100 μm. **g,** The histology of muscle sections was investigated by Masson's trichrome staining. Reduced muscular dystrophy was observed in HDR-NP-treated mice. Scale bar: 100 μm. Statistical significance was calculated via (**b**) one-way ANOVA or (**c**) two-way ANOVA with a Tukey's post hoc test. $*P < 0.05$, $***P < 0.001$, $****P < 0.0001$. ns, not significant.

2.2.6 NHEJ-NP and HDR-NP exhibited good biocompatibility and negligible immunogenicity.

The in vivo biocompatibility of NHEJ-NP was also evaluated after intravenous or intramuscular injections. A panel of blood biochemical parameters were measured using serum collected from Ai14 mice that received intravenous injection of PBS, intravenous injection of NHEJ-NP, and

intramuscular injection of NHEJ-NP in tibialis anterior muscles, respectively. No significant variations were found in these biochemical parameters (**Figure 2.20**). We also observed major organs and muscles collected from these mice via H&E staining (**Figure 2.21**). Again, no sign of any systemic or local toxicity was found associated with NHEJ-NP treatments. Immunity against CRISPR-Cas9 which is a nuclease from *Streptococcus pyogenes* has been a concern for clinical translation [15, 49].

To analyze the immune response generated by intramuscular administration of HDR-NP, we analyzed a panel of inflammatory cytokine levels in the PBS- or HDR-NP-treated *mdx* mouse muscles by quantitative RT-PCR (**Figure 2.5c**). HDR-NP did not induce significant changes in expression levels of most cytokines analyzed, although elevations of IFN-γ and TNF-α expression were detected. This can be attributed to the enhanced macrophage recruitment and/or activation for clearance of nanoparticles in the muscle, as previously reported [15, 50].

2.2.7 NHEJ-NP and HDR-NP possess desirable characteristics for potential clinical translation.

The mPEG-PC7A polymer can be conveniently scaled up. For instance, using common lab glassware we were able to synthesize >10 grams of mPEG-PC7A for each batch with simple purification (i.e., dialysis). The polymer can be stored at room temperature in its dry powder form for one year without observable changes in its chemical structure. The preparation of NHEJ-NP and HDR-NP only requires mixing, pipetting, and vortexing, which means they can be freshly prepared by a laboratory technician within half an hour. Despite the ease of fabrication and thus making it possible to use freshly made nanoparticles, the stability of pre-made NHEJ-NP stored at different temperatures was also tested. The editing efficiency of NHEJ-NP stored at 4 ºC, -20 ºC,

or -80 ºC was quantified in HEK293 cells weekly. It was found that NHEJ-NP could be stored at 4 ºC, -20 ºC, or -80 ºC for 4 weeks without affecting its gene editing efficiency (**Figure 2.22a**). The stability of NHEJ-NP in serum-containing solutions was also examined. As shown in **Figure 2.22b**, serum did not trigger premature disassembly of NHEJ-NP. Thus, this unique RNP or RNP+ssODN delivery nanosystem is easy to synthesize, fabricate, and scale-up. Moreover, it can be easily stored and transported, making it particularly suitable for clinical translation.

2.3 Conclusion

The pH-responsive amphiphilic polymer, mPEG-PC7A, can accommodate the heterogeneity (e.g., charge and hydrophobicity) of Cas9 RNP and ssODN via both electrostatic and hydrophobic interactions. Through a straightforward preparation process, NHEJ-NP and HDR-NP encapsulating Cas9 RNP and Cas9 RNP + ssODN, respectively, can be formed at the optimal pH conditions. These NPs offer high payload loading contents (17 wt%) and have small (around 30 nm) and uniform sizes. NHEJ-NP and HDR-NP offer a safe and efficient approach for both in vitro and in vivo (via both local or systemic administration) genome editing and possess good biocompatibility and low immunogenicity. The therapeutic efficacy of HDR-NP for treating Duchenne muscular dystrophy was also demonstrated. HDR-NP effectively restored the expression of dystrophin and thus improved the muscle strength of diseased mice. NHEJ-NP and HDR-NP are easy to produce and can be conveniently stored, thus they are of great interest for various in vitro and in vivo genome editing applications with clinical translation potentials. Future work will focus on further optimization of this nanosystem by tailoring the polymer chemical structures to enhance its editing efficiency. In addition, aside from livers and muscles, the in vivo

editing efficiency of NHEJ-NP or HDR-NP in other organs or tissues will be explored by taking the advantage of the chemical versatility in ligand conjugation. The potential of re-engineering this nanosystem for delivery of other genome editors, including Cas12, Cas13, and base editor systems, will be investigated as well.

2.4 Methods

2.4.1 Materials.

Tetrahydrofuran (THF), hexane, ethyl acetate, chloroform, anhydrous dimethylformamide (DMF), tris(2-carboxyethyl)phosphine hydrochloride (TCEP), tris(hydroxymethyl)aminomethane hydrochloride solution (Tris·HCl, 1M), Y-27632 dihydrochloride and bovine serum albumin (BSA) were purchased from Fisher Scientific. Triethylamine, NaOH, NaCl, hydrochloric acid (HCl), methacryloyl chloride, diethyl ether, CuBr, and anhydrous $MgSO_4$ were obtained from Sigma-Aldrich. N,N,N',N",N"-pentamethyldiethylenetriamine (PMDETA) and 2-(azepan-1-yl)ethanol was purchased from Tokyo Chemical Industry Co., Ltd. and ChemScene, LLC, respectively. Methoxy-poly(ethylene glycol)-hydroxy (mPEG-OH, Mw~5kDa) and maleimide-poly(ethylene glycol)-hydroxy (Mal-PEG-OH, Mw~5kDa) were provided by JenKem Technology USA Inc. Cell-penetrating peptide Cys-TAT (47-57) (CPP, sequence: CYGRKKRRQRRR-NH_2) was obtained from GenScript, Inc. Ultrapure water was freshly produced using Milli-Q system (MilliporeSigma).

2.4.2 Synthesis of 2-(azepan-1-yl)ethyl methacrylate (C7A-MA).

Triethylamine (7.0 g, 69 mmol) and 2-(azepan-1-yl)ethanol (5.0 g, 34.5 mmol) were dissolved in anhydrous THF (100 mL) and cooled on ice. Methacryloyl chloride (4.0 g, 38.5 mmol) in

anhydrous THF (15 mL) was added dropwise into the previous solution. The reaction was stirred at 20 ºC for 24 h and then the reaction mixture was filtered to remove triethylamine hydrochloride salt. The resulting filtrate was condensed by rotary evaporation and further purified by column chromatography using hexane/ethyl acetate (3/1, v/v) as the eluent. The product was obtained by removing solvents *in vacuo* and characterized by ^{1}H NMR ($CDCl_3$, 400 MHz).

2.4.3 Synthesis of methoxy-/ maleimide-poly(ethylene glycol)-2-bromoisobutyrate (mPEG-Br and Mal-PEG-Br).

mPEG-OH (1.0 g, 0.2 mmol) was dissolved in chloroform (30 mL) followed by the addition of triethylamine (1 mL). The solution was cooled on ice, and 2-bromoisobutyryl bromide (0.3 mL, 2.4 mmol) in chloroform (10 mL) was added dropwise. The mixture was stirred at 20 ºC for 24 h. The solution was washed with saturated brine (40 mL) three times and dried with anhydrous $MgSO_4$ for 12 h. The supernatant was then concentrated to 5 mL by rotary evaporation and the resulting solution was precipitated in 45 mL of ice-cold diethyl ether to yield the final product (i.e., mPEG-Br). Mal-PEG-Br was synthesized following the same protocol except Mal-PEG-OH was used instead of mPEG-OH. The products were obtained by removing solvents *in vacuo* and characterized by ^{1}H NMR ($CDCl_3$, 400 MHz).

2.4.4 Synthesis of methoxy-/ maleimide-poly(ethylene glycol)-*b*-poly(2-(azepan-1-yl)ethyl methacrylate) (mPEG-PC7A).

mPEG-PC7A was synthesized by atom transfer radical polymerization (ATRP) using mPEG-Br as a macroinitiator. C7A-MA (0.41 g, 2 mmol), CuBr (2.8 mg, 20 μmol), and mPEG-Br (0.2 g, 40 μmol) were dissolved in 1.0 mL of anhydrous THF. After three cycles of freeze-pump-thaw, PMDETA (3.4 mg, 20 μmol) was added. The polymerization was carried out at 70°C for 20 h. The

reaction mixture was dissolved by adjusting pH to ~4 with 1 M HCl aqueous solution and dialyzed with a dialysis membrane tubing (molecular weight cut-off, MWCO ~ 3500 Da) against ultrapure water for 72 h to yield purified mPEG-PC7A. Mal-PEG-PC7A was synthesized following the same protocol using Mal-PEG-Br instead. The products were obtained by lyophilization and characterized by ^{1}H NMR ($CDCl_3$, 400 MHz).

2.4.5 Synthesis of cell-penetrating peptide-conjugated poly(ethylene glycol)-*b*-poly(2-(azepan-1-yl)ethyl methacrylate) (CPP-PEG-PC7A).

CPP was conjugated to Mal-PEG-PC7A through a maleimide-thiol Michael reaction. Cys-TAT (47-57) (1.82 mg, 1.1 μmol) and TCEP (1.58 mg, 5.5 μmol) were dissolved in anhydrous DMF (1 mL). Subsequently, the Mal-PEG-PC7A (10.0 mg, 1.0 μmol) solution (anhydrous DMF (1 mL)) was mixed with this solution. The reaction was conducted under nitrogen at 20 ºC for 12 h. Thereafter, the solution was dialyzed against ultrapure water (MWCO ~ 3500 Da) for 72 h, and the final product was collected by lyophilization.

2.4.6 Preparation of NHEJ-NPs and HDR-NPs.

Cas9 RNP was formed by complexing sNLS-*Sp*Cas9-sNLS nuclease (Aldevron, LLC) with sgRNA (Integrated DNA Technologies, Inc.) at a molar ratio of 1/1 at 20 ºC for 5 min. For HDR-NP synthesis, ssODN (Integrated DNA Technologies, Inc.) was mixed with Cas9 RNP at a molar ratio of 1/1. The payload solution (5 mg/mL) was then diluted with 100 mM Tris·HCl buffer solution to 2.5 mg/mL. Thereafter, the mPEG-PC7A aqueous solution (20 mg/mL) was mixed with the payload solution at 0.625/1 (vol/vol). The resulting mixture solution was vortexed for 1 min, incubated at 20 ºC for 15 min, diluted with Tris·HCl buffer solution, and then vortexed again for 1 min. After another incubation at 20 ºC for 15 min, solutions containing NHEJ-NPs or HDR-

NPs were directly used for cell treatments or animal injections without further purification. CPP-NHEJ-NP was prepared by using CPP-PEG-PC7A instead of mPEG-PC7A following the same process. The final NHEJ-NP or HDR-NP solution was isotonic and contained 1.0 mg/mL Cas9 nuclease. Sequences of sgRNAs and ssODNs used in this work were summarized in **Table 2.1 and 2.2**.

2.4.7 Nanoparticle characterization.

The hydrodynamic diameters and zeta potentials of NHEJ-NPs and HDR-NPs were measured by dynamic light scattering (DLS, ZetaSizer Nano ZS90, Malvern Panalytical Ltd) and analyzed using Zetasizer software v7.01 (Malvern Panalytical Ltd). The morphology of NHEJ-NPs and HDR-NPs was studied by transmission electron microscopy (FEI Tecnai 12, 120 kV, Fischione Instruments, Inc.) and analyzed by ImageJ 1.51j8 (NIH).

2.4.8 Gel retardation assay.

Gels were cast using 2% (w/v) agarose solution in tris-acetate-ethylenediaminetetraacetic acid (TAE) buffer solution containing SYBR Safe DNA Gel Stain (Thermo Fisher Scientific). Free Cas9 RNP, sgRNA, ssODN, Cas9 RNP + ssODN, NHEJ-NP, and HDR-NP with an equivalent dosage of 0.5 μg nucleic acids per well were loaded in the gel, respectively. Electrophoresis was conducted with a voltage at 110 V for 30 min using Mini-Sub Cell GT Horizontal Electrophoresis System (Bio-Rad Laboratories, Inc.). Retardation of all tested samples was visualized by a UV Illuminator (Bio-Rad Laboratories, Inc.) and analyzed by Image Lab software (Bio-Rad).

2.4.9 Cell culture.

Human embryonic kidney (HEK293) cells, GFP-expressing HEK293 cells, and BFP-expressing HEK293 cells were cultured at 37 ^{o}C in a 5% CO_2 atmosphere with the Dulbecco's Modified Eagle

Medium (Thermo Fisher Scientific) supplemented with 10% (v/v) fetal bovine serum (Thermo Fisher Scientific) and 1% (v/v) Penicillin-Streptomycin (Thermo Fisher Scientific). BFP-expressing WA09 human embryonic stem cells (hESCs) were maintained at 37 ºC in a 5% CO_2 atmosphere in the StemFlex™ Medium (Thermo Fisher Scientific) on Matrigel (Corning) coated tissue culture polystyrene plates (BD Falcon). Cells were passaged every 3–4 days at a 1:10 ratio using Versene solution (Thermo Fisher Scientific). ROCK inhibitor Y-27632 (10 μM) was periodically supplemented to the culture media to enhance the viability of stem cells.

2.4.10 Assaying gene editing efficiency of NHEJ-NPs and HDR-NPs.

GFP-expressing or BFP-expressing HEK293 cells were seeded in 96-well plates (5,000 cells per well). BFP-expressing hESCs were seeded in 96-well plates coated with Matrigel (5,000 cells per well). After 24 h, various NHEJ-NP or HDR-NP formulations were prepared freshly and added to the cells with dosages of RNP and ssODN (for HDR-NP only) both at 3.13 pmol per well. Lipofectamine 2000 (Thermo Fisher Scientific) or Lipofectamine CRISPRMAX (Thermo Fisher Scientific) formulations complexed with the same dosage of RNP or RNP+ssODN were prepared according to the manufacturer's manual. After 96 h, cells were detached by Trypsin-EDTA (0.25%, Thermo Fisher Scientific, for HEK293 cells) or Versene solution (for hESCs) and collected for flow cytometry analysis (Attune NxT, Thermo Fisher Scientific). The percentage of GFP-negative cells was used for NHEJ efficiency assay in GFP-expressing HEK293 cells. The percentage of GFP-positive cells was used for HDR efficiency assay in BFP-expressing HEK293 cells and BFP-expressing hESCs. Data were analyzed by FlowJo.

2.4.11 Cell viability.

HEK293 cells were seeded in 96-well plates (10,000 cells per well). After 24 h, cells were treated with Lipofectamine 2000, Lipofectamine CRISPRMAX, NHEJ-NP, and HDR-NP all at 6.25 pmol, respectively. After 48 h of incubation, a standard cell counting kit-8 assay (CCK-8, Dojindo Molecular Technologies, Inc.) was performed according to the manufacturer's instructions. Each well was added with 10 μl CCK-8 solution and incubated at 37 ºC for 4 h. Thereafter, the absorbance at 450 nm and 650 nm (as a reference) of each well was measured using a microplate reader (Promega Corporation). The cell viability relative to the untreated cells was finally calculated.

2.4.12 Cellular uptake study.

To prepare fluorophore-labeled NHEJ-NP and CPP-NHEJ-NP, negative control crRNA and Atto 550-labeled tracrRNA (Integrated DNA Technologies, Inc.) were first complexed at a 1/1 molar ratio for 10 min at 20 ºC to form gRNA and then complexed with Cas9 nuclease at 1/1 molar ratio to form Atto 550-labeled Cas9 RNP. Thereafter, Atto 550-labeled NHEJ-NP and CPP-NHEJ-NP were prepared following the same protocol mentioned above. HEK293 cells were seeded in 96-well plates (10,000 cells per well) 24 h before treatments. For endocytosis pathway study, a variety of inhibitors including wortmannin (10 μg/mL), chlorpromazine (10 μg/mL), genistein (100 μg/mL), and methyl-β-cyclodextrin (5 mM) dissolved in serum-containing cell culture media were added to HEK293 cells, respectively. The cells were then incubated at 37 ºC for 30 min and washed thoroughly with 1X DPBS three times. Atto 550-labeled NHEJ-NP or CPP-NHEJ-NP was then added to the cells with a dosage of RNP at 6.25 pmol per well. After 4 h incubation at 37 ºC, the media were aspirated, and the cells were washed with 1X DPBS three times and collected after

trypsinization. For incubation at 4 ºC, cells were pretreated at 4 ºC for 30 min. Atto 550-labeled NHEJ-NP or CPP-NHEJ-NP was then added to the cells (6.25 pmol RNP per well), which were incubated at 4 ºC for 4 h before media removal. The cells were washed with 1X DPBS three times and collected after trypsinization. The cellular uptake of NHEJ-NP and CPP-NHEJ-NP in HEK293 cells was assayed by flow cytometry to quantify Atto 550-positive cells.

2.4.13 Intracellular trafficking.

HEK293 cells were seeded in an 8-well chamber slide (20,000 cells per well) and cultured for 24 h before use. Atto 550-labeled NHEJ-NP was formulated as mentioned above and added to the cells at 6.25 pmol RNP per well. At certain time points (i.e., 0.5 h, 2 h, and 4 h), the cells were washed with 1X DPBS three times and treated with LysoTracker Green DND-26 (75 nM, Thermo Fisher Scientific) and Hoechst 33342 (1 μg/mL, Thermo Fisher Scientific) to stain endosomes/lysosomes and nuclei, respectively. Cells were washed with 1X DPBS three times again and then imaged using an AR1 confocal microscope (Nikon). Images were exported using NIS Viewer v5.21 (Nikon).

2.4.14 Animals.

All animal studies strictly conformed to the Guide for the Care and Use of Laboratory Animals (National Institutes of Health) and protocols approved by the Institutional Animal Care and Use Committee (IACUC) at the University of Wisconsin-Madison. B6.Cg-*Gt(ROSA)26Sor*$^{tm14(CAG-tdTomato)Hze}$/J mice (Ai14 mice, 4-8 weeks old, male and female, JAX stock #007914) were randomly divided into groups and used to assay the in vivo gene editing efficiency of NHEJ-NP. C57BL/10ScSn-*Dmd*^{mdx}/J (*mdx* mice, 4 weeks old, male, JAX stock #001801) and C57BL/6J (wild-type mice, 4 weeks old, male, JAX stock #000664) were randomly divided into

groups and used to assay the in vivo gene editing efficiency of HDR-NP for DMD treatments. All mice were maintained under a tightly controlled temperature (22 °C), humidity (40–50%), light/dark (12/12 h) cycle conditions, with water and food *ad libitum*. The *mdx* mice were specially fed with a diet containing 6% fat (LabDiet® 5K52). Before injections, the mice were anesthetized with 3% isoflurane for 8-10 min followed by 1% isoflurane during the injection.

2.4.15 In vivo gene editing in Ai14 mice.

Cas9 nuclease was complexed with synthetic sgRNA (Integrated DNA Technologies, Inc.) designed for the excision of SV40 polyA blocks to form Cas9 RNP. NHEJ-NP was then prepared as described above and used for intravenous and intramuscular injections. For intravenous injections, two groups of Ai14 mice (n = 3 per group, ~20 g in body weight) were injected with 100 μl of PBS (negative control) and NHEJ-NP solutions (containing 1.2 μg/μl Cas9 RNP, equivalent to 6 mg/kg) via retro-orbital injections. For intramuscular injections, mice were administered with 1X DPBS (negative control) or NHEJ-NP solutions (containing 1.2 μg/μl Cas9 RNP) in the tibialis anterior muscle (40 μl, n = 3 muscles per group) using 32-gauge syringes. After 7 days, the whole blood of mice was collected from the sublingual vessel into heparin-coated collection tubes and the serum was separated by centrifugation at 1,500 x g for 10 min for hematological analysis. Thereafter, mice were euthanized and their major organs and tissues including heart, liver, spleen, lung, kidney, and muscles were stored immediately in 4% neutral-buffered formalin at 4 ºC (for fixation and cryosection), or flash-frozen by liquid nitrogen and stored at -80 ºC (for other studies).

2.4.16 In vivo imaging assay.

TdTomato expression in the organs and tissues of the mice was first assayed by in vivo imaging system (IVIS) equipped with an excitation wavelength at 554 nm and an emission wavelength at 581 nm. Thereafter, small portions of the livers were collected, treated with lysis buffer, and sonicated for tissue homogenization. The fluorescence intensity of homogenized samples was then quantified again by IVIS.

2.4.17 Cell isolation and staining for flow cytometry.

To test the cell types that were edited by NHEJ-NP in the liver of Ai14 mice, live cells were isolated from mouse liver 7 days after the injection of 1X DPBS or NHEJ-NP (n = 3 per group) and stained for flow cytometry [51, 52]. For cell isolation, the mouse was anesthetized with 3% isoflurane and then perfused with liver perfusion medium (Thermo Fisher Scientific) for the first 10 min followed by liver digestion medium (Thermo Fisher Scientific) for another 10 min. The liver was then collected in a centrifuge tube and cut into pieces, which were washed with an ice-cold hepatocyte wash medium (Thermo Fisher Scientific) and centrifuged at 300 x g for 5 min. The supernatant was removed, and the pellet was resuspended using an ice-cold hepatocyte wash medium. The cell suspension was filtered through 70 μm cell strainers to a new tube. Cells in the filtrate were washed twice with ice-cold hepatocyte wash medium, and collected by centrifugation at 300 x g for 5 min. Thereafter, the cells were resuspended in 1X DPBS and counted by Countess Automated Cell Counter (Thermo Fisher Scientific). For cell staining, the cells were incubated with Alexa Fluor 488 anti-mouse CD31 antibodies for endothelial cells (BioLegend, 102414), and Pacific Blue anti-mouse CD45 antibody (BioLegend, 103126) for immune cells, both at a 1:300 dilution (100 μl total volume) for 30 min in the dark at 4 ºC. Ghost Dye Red 780 (Tonbo

Biosciences, 13-0865-T500) was used for staining to identify live cells. The cell suspension was finally analyzed using flow cytometry (Attune NxT, Thermo Fisher Scientific).

2.4.18 In vivo gene editing in *mdx* mice.

Cas9 nuclease was complexed with synthetic sgRNA (Integrated DNA Technologies, Inc.) targeting the exon 23 in the *Dmd* gene and ssODN for gene correction. HDR-NP was then prepared as described above. For intramuscular injections, mice were administered with 1X DPBS (negative control, n = 7 animals) or HDR-NP solutions (containing 1.2 μg/μl Cas9 RNP and 0.36 μg/μl ssODN (Cas9 RNP/ssODN = 1/1, mol/mol), n = 11 animals) in both tibialis anterior muscles (20 μl), both gastrocnemius muscles (20 μl) and both triceps brachii muscles (40 μl) using 32-gauge syringes (total 6 muscles per mouse). Wild-type mice (n = 6 animals) were used as the positive control without injections. The hanging times for these mice were tested weekly. After 28 days, mice were euthanized and their major organs including heart, liver, spleen, lung, and kidney, and muscles (including tibialis anterior, gastrocnemius, and triceps brachii muscles) were collected and stored immediately in 4% neutral-buffered formalin at 4 ^{o}C (for fixation and cryosection), or flash-frozen by liquid nitrogen and stored at -80 ^{o}C (for other studies). For the gene sequencing study, *mdx* mice were intramuscularly injected with 40 μl of 1X DPBS (negative control) or HDR-NP solutions (containing 1.2 μg/μl Cas9 RNP and 0.36 μg/μl ssODN) in tibialis anterior muscle. After 7 days, mice were euthanized, and the tibialis anterior muscles were collected for genomic DNA extraction.

2.4.19 Hanging time assay.

Four-limb hanging time assays were performed on untreated wild-type mice and *mdx* mice with or without HDR-NP treatments weekly after the treatments, following the previously reported

method [15, 53]. In brief, the apparatus was set up by positioning a metal grid 25 cm above a big cage for rats. Soft bedding was placed at the cage bottom to prevent mice from harming themselves when falling. Thereafter, a mouse was placed on the grid and the grid was inverted above the cage, so the mouse started to hang. The test session ended if the mouse was able to hang for 600 seconds. Each mouse was tested three times to determine the representative hanging time.

2.4.20 Sanger Sequencing.

The genomic DNA was isolated from muscles using Monarch® Genomic DNA Purification Kit (New England Biolabs, #T3010) following the manufacturer's protocol. Genomic PCR was performed using Q5® High-Fidelity 2X Master Mix (New England Biolabs, #M0492) with genomic DNA templates (1 μg) and customized primers (0.5 μM, Integrated DNA Technologies, Inc.), following the manufacturer's protocol and thermocycling conditions: 30 cycles of 98 °C for 10 s, 63 °C for 30 s, and 72 °C for 30 s with a final extension time at 72 °C for 2 min. PCR products were purified using AMPure XP (Beckman Coulter, Inc.) and quantified by Nanodrop One Microvolume UV-Vis Spectrophotometer (Thermo Fisher Scientific). Sanger sequencing was finally performed with a sample containing 10 ng purified PCR product and 25 pmol primers by GENEWIZ. The sequencing results were analyzed using ApE software v3.0.5 (https://jorgensen.biology.utah.edu/wayned/ape/), SnapGene Viewer v5.3, and TIDE web tool (http://shinyapps.datacurators.nl/tide/) [15].

2.4.21 Immunofluorescence staining.

TdTomato expression was further investigated via immunofluorescence staining. The collected tissues and organs were embedded in optimal cutting temperature (OCT) compound blocks (Thermo Fisher Scientific), and the blocks were sectioned into 8 μm slices. For samples from Ai14

mice, sections were stained with anti-RFP primary antibody (Abcam, ab152123, 1:1,000) for TdTomato. Hepatocytes, Kupffer cells and endothelial cells in the liver were further stained by HepPar1 (NBP2-45272, diluted at 1:100, Novus Biologicals), anti-F4/80 antibody [CI:A3-1] (Abcam, ab152123, 1:100) and anti-CD31 antibody (Abcam, ab56299, 1:400). For samples from the DMD mice, the sections were stained with dystrophin antibody (Santa Cruz Biotechnology, sc-47760, 1:100). All sections were further stained by secondary antibodies (Abcam, ab150113, ab150080, ab150155, all 1:1,000) and DAPI (Abcam, ab228549, 1:1,000) for visualization. After mounting on glass slides, the sections were imaged using a Nikon AR1 confocal microscope (for Ai14 mouse samples) or Zeiss LSM 710 confocal microscope (for *mdx* mouse and wild-type mouse samples). Images were exported using NIS Viewer v5.21 (Nikon) or ZEN blue v3.3 (Zeiss).

2.4.22 Trichrome staining.

Trichrome staining of muscle sections was performed using Masson's Trichrome Stain Kit (G-Biosciences, BAQ085) following the manufacturer's protocol. The stained sections were observed under an optical microscope.

2.4.23 In vivo biocompatibility assay.

Hematological analysis was performed using the collected mouse serum to evaluate the key elements of the blood biochemical profile using VetScan Preventive Care Profile Plus rotors (Abaxis) in a VetScan VS2 blood chemistry analyzer (Abaxis), following the manufacturer's protocol. Moreover, to evaluate the systemic or local toxicity, dehydrated and fixed organs (i.e., heart, liver, spleen, lung, kidney) and tibialis anterior muscles were embedded in OCT and the blocks were sectioned. The sections were stained with hematoxylin and eosin (H&E) and observed under an optical microscope.

2.4.24 In vivo immunogenicity assay.

The immunogenicity of HDR-NPs in treated muscles was analyzed by RT-PCR. In brief, the muscle samples collected from *mdx* mice were stored in RNAlater solution (Thermo Fisher Scientific) at -20 ºC until RNA extraction. RNA in these samples was extracted using TRIzol reagent (Thermo Fisher Scientific) following manufacturer's protocol and quantified by Nanodrop One Microvolume UV-Vis Spectrophotometer. cDNA was then synthesized using iScript™ Reverse Transcription Supermix for RT-PCR (Bio-Rad Laboratories, Inc.) following the manufacturer's protocol. Quantitative RT-PCR was finally performed using iTaq Universal SYBR Green Supermix (Bio-Rad Laboratories, Inc.) with cDNA templates (10 ng) and customized primers (0.5 μM, Integrated DNA Technologies, Inc.) for genes of interest on a CFX96 Touch Real-Time PCR Detection System (Bio-Rad Laboratories, Inc.). The thermocycling conditions used for PCR were 40 cycles of 95 °C for 5 s and 60 °C for 30 s. Melt curve analysis was performed at the end of PCR experiments. Glyceraldehyde 3-phosphate dehydrogenase (GAPDH) was selected as the reference gene for data analysis. Data were analyzed using CFX Maestro 2.0 (Bio-Rad). Sequences of primers used in this work are summarized in **Table 2.3**.

2.4.25 Statistical analysis.

Results are presented as mean ± standard deviation. Statistical differences between experimental groups were analyzed using one-way ANOVA test or two-way ANOVA test followed by Tukey's post hoc comparison test. Statistical analyses were performed using GraphPad Prism 9.0 software. Significant differences between groups were indicated by $*P < 0.05$, $**P < 0.01$, $***P < 0.001$ and $****P < 0.0001$, respectively. $P \geq 0.05$ was considered not statistically significant in all analyses (95% confidence level).

2.5 Supplementary Figures

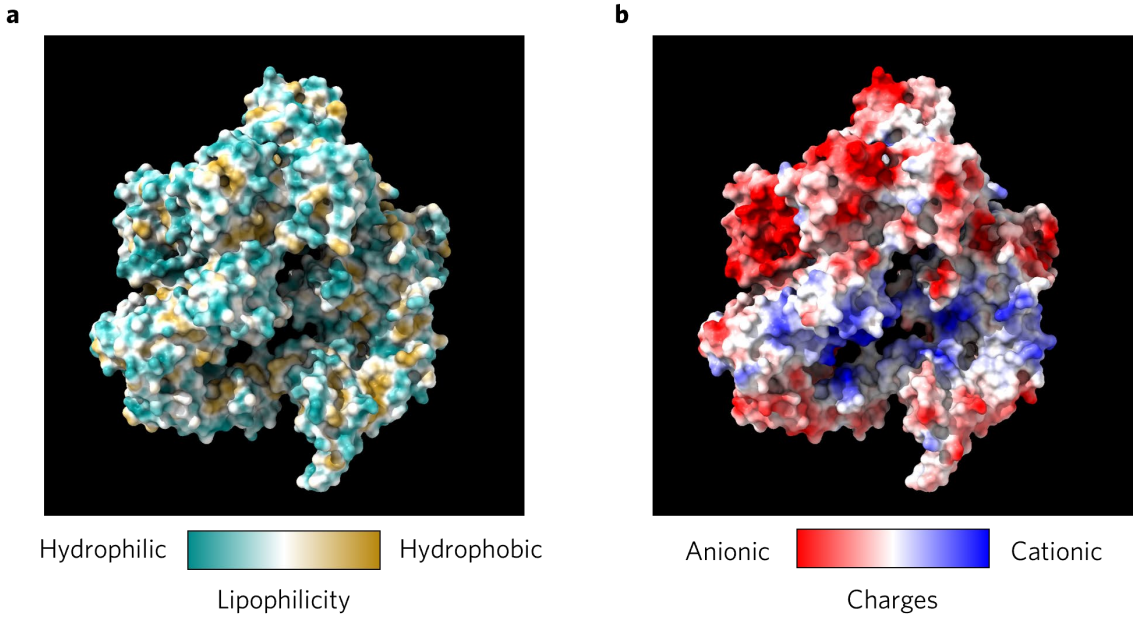

c

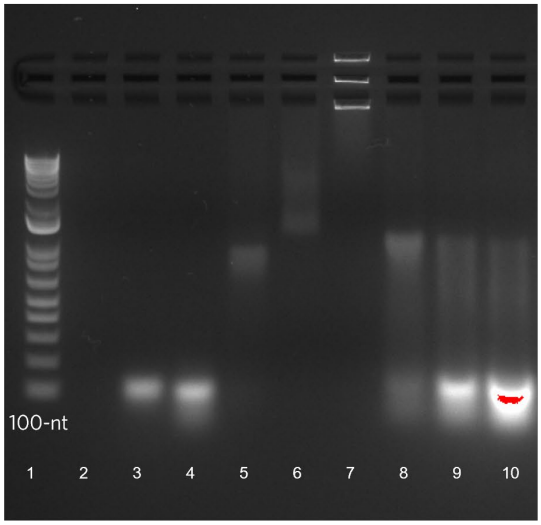

#	Cas9	sgRNA	ssODN
1	Ladder		
2	+		
3		+	
4			+
5	+	++	
6	+	+	
7	++	+	
8	+	+	+
9	+	+	++
10	+	+	++++

"+" = 1 molar equivalent

Figure 2.6 | Surface properties of the SpCas9 nuclease and the complexation of SpCas9 nuclease with sgRNA and ssODN.

a, Illustration of the surface lipophilicity of the SpCas9 nuclease. There are abundant lipophilic (hydrophobic) amino acids present on the SpCas9 which can interact with the amphiphilic polymer

through hydrophobic interaction. **b,** Illustration of the surface charge distribution on SpCas9 nuclease. Negatively charged surface domains can efficiently complex with cationic polymers via electrostatic interactions. After forming the Cas9 RNP with sgRNA, the anionic charge density on Cas9 RNP is further enhanced and thus the electrostatic interactions can be strengthened. **b,** Gel retardation assay of Cas9 nuclease, sgRNA, ssODN, and their complexes indicates: (1) aggregation can form (Sample #7) when the molar ratio of Cas9 : sgRNA < 1, and (2) no complexation occurs between Cas9 RNP and ssODN. The Illustrations shown in (**a**) and (**b**) were generated using UCSF ChimeraX Software v1.1.

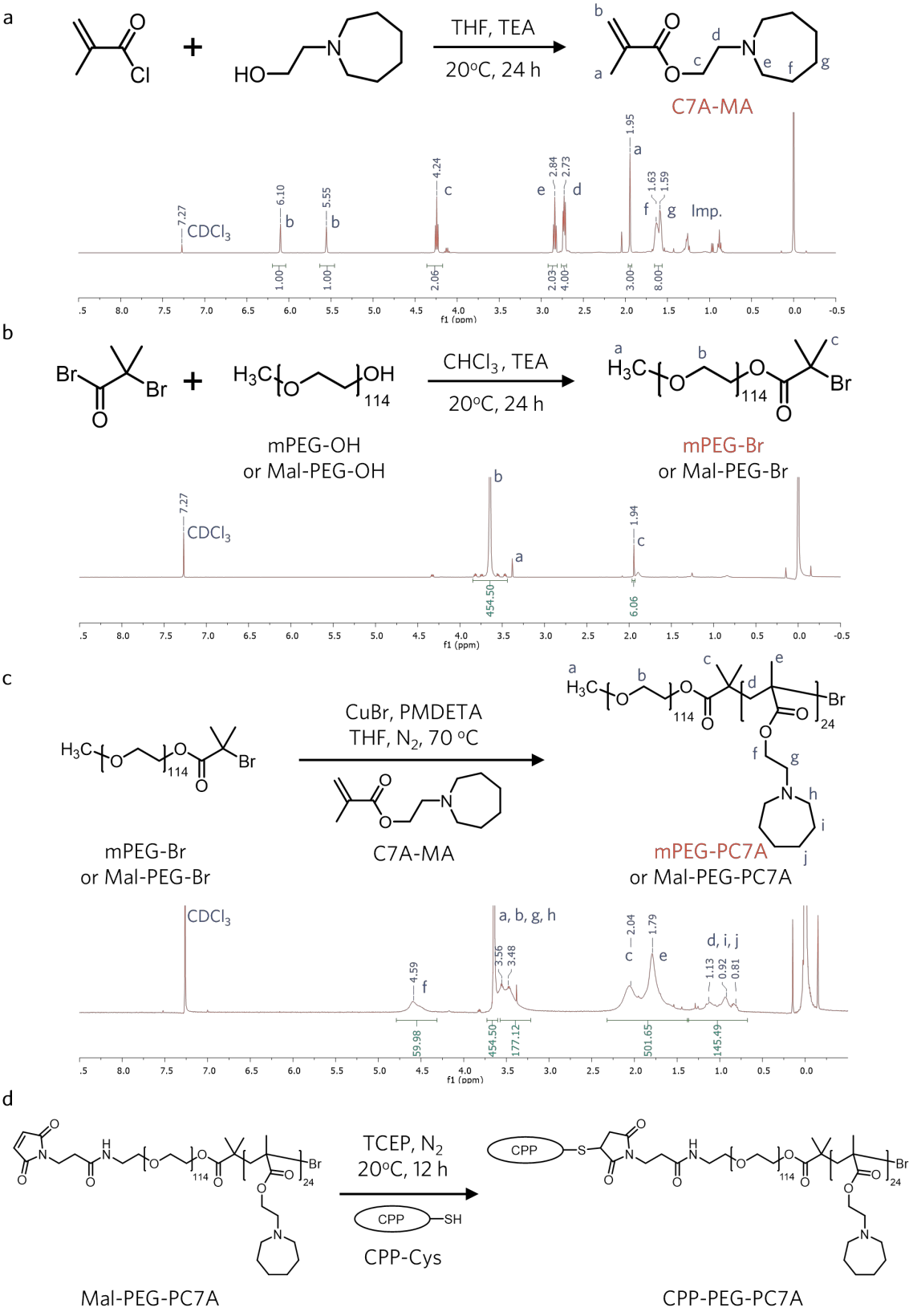
a
THF, TEA
20°C, 24 h
C7A-MA
CDCl3
Imp.
b
CHCl3, TEA
20°C, 24 h
mPEG-OH
or Mal-PEG-OH
mPEG-Br
or Mal-PEG-Br
c
CuBr, PMDETA
THF, N2, 70 °C
C7A-MA
mPEG-Br
or Mal-PEG-Br
mPEG-PC7A
or Mal-PEG-PC7A
d
TCEP, N2
20°C, 12 h
CPP-Cys
Mal-PEG-PC7A
CPP-PEG-PC7A

Figure 2.7 | Synthesis and ^{1}H-NMR characterization of the monomer and polymers.

a, 2-(azepan-1-yl)ethyl methacrylate (C7A-MA); **b,** methoxy- or maleimide-poly(ethylene glycol)-bromide (mPEG-Br or Mal-PEG-Br); **c,** methoxy- or maleimide-poly(ethylene glycol-***b***-2-(azepan-1-yl)ethyl methacrylate) (mPEG-PC7A or Mal-PEG-PC7A); **d,** cell-penetrating peptide (CPP)-conjugated polymer (CPP-PEG-PC7A). Imp., impurities.

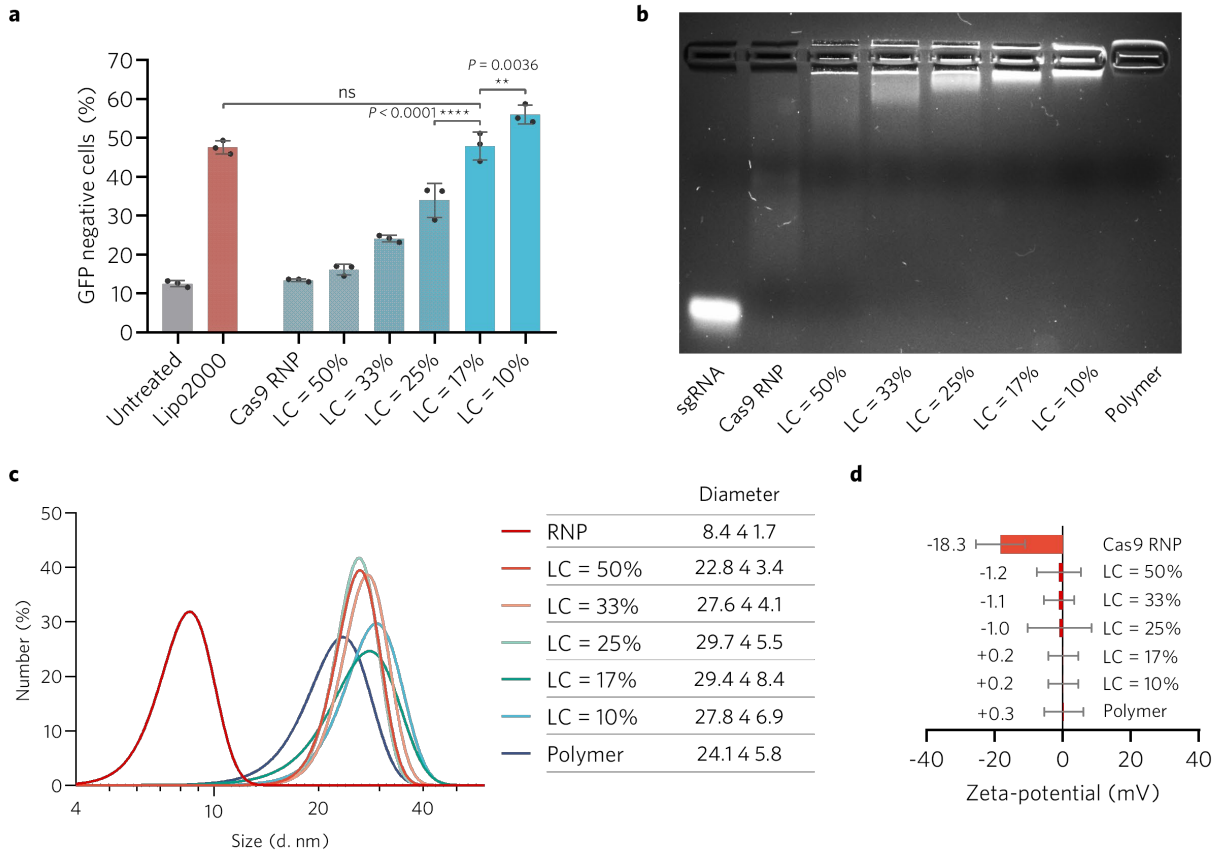

Figure 2.8 | Optimization of the loading content for NHEJ-NP.

a, Gene editing efficiency of NHEJ-NPs with different loading content of the Cas9 RNP in GFP-expressing HEK293 cells. Generally, formulations with a lower loading content (more polymers) led to higher editing efficiency. The loading contents for both NHEJ-NP and HDR-NP were set at

17% for in vitro and in vivo studies. **b,** Electrophoresis assay of NHEJ-NPs with different loading contents of Cas9 RNPs in 2% agarose gel. The result suggests that more polymers can lead to better encapsulation of the Cas9 RNP in the NPs, and thus lead to better editing efficiency. (**c**) Hydrodynamic diameters and (**d**) zeta-potentials of NHEJ-NPs with different loading contents of Cas9 RNPs indicate that nanoparticles were formed even with LC = 50%. Therefore, the ineffectiveness of the formulations with high loading contents may also be attributed to their instability in the serum-containing cell culture media. Statistical significance was calculated via one-way ANOVA with Tukey's post hoc test. $^{**}P < 0.01$, $^{****}P < 0.0001$. ns, not significant.

Loading content (LC) is defined as:

$$\mathrm{LC} = \frac{mass\ (Cas9\ RNP)}{mass\ (Cas9\ RNP) + mass(Polymer)} \times 100\%$$

For example, "LC = 17%" is equivalent to "Cas9 RNP/Polymer = 1/5 (weight/weight)".

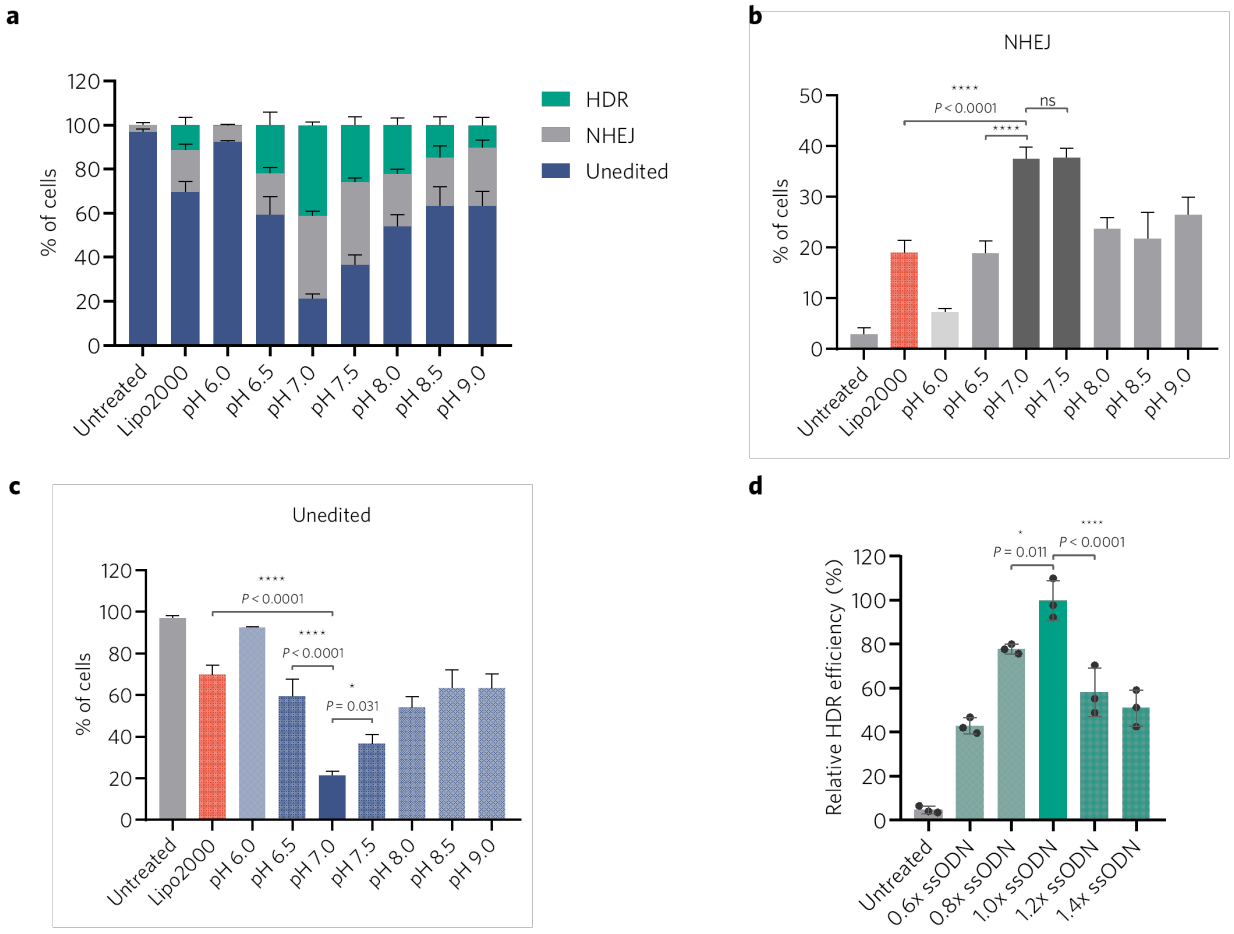

Figure 2.9 | The NHEJ efficiency and HDR efficiency induced by HDR-NPs in BFP-expressing HEK293 cells.

a, Percentages of cells edited via HDR, NHEJ, or unedited cells, respectively, after 96 h incubation with HDR-NPs formed at different pH values. **b-c,** The respective (**b**) NHEJ efficiency and (**c**) percentage of unedited cells after treatments. Data were collected and analyzed by flow cytometry. Data are presented as mean ± s.d. (n=3). **d,** Normalized HDR efficiency by HDR-NPs formed by different Cas9 RNP/ssODN molar ratios in BFP-expressing HEK293 cells. Statistical significance was calculated via one-way ANOVA with Tukey's post hoc test. *$P < 0.05$, ****$P < 0.0001$. ns, not significant.

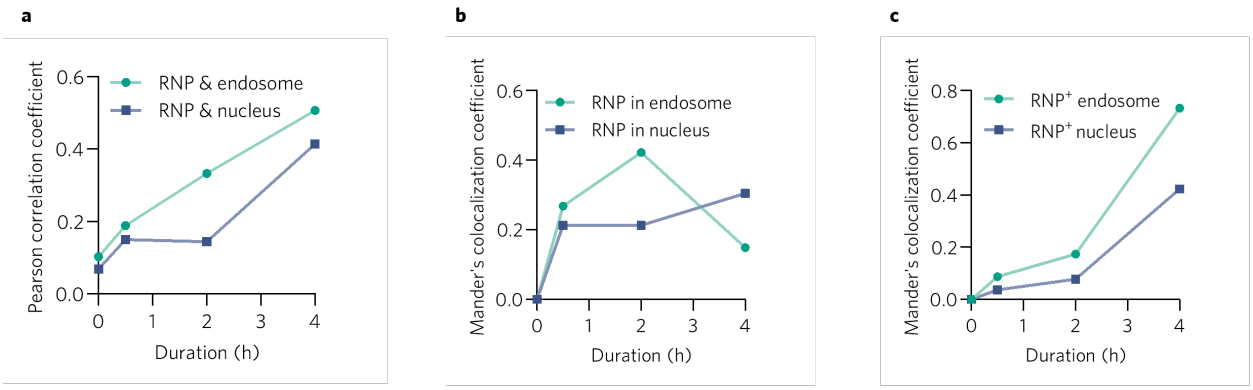

Figure 2.10 | The Pearson correlation coefficient and Mander's colocalization coefficient used to analyze the colocalization of the intracellular fluorescence signals of RNP and those of endosomes or nuclei in HEK293 cells.

(**a**) The Pearson correlation coefficient ranges from -1 to +1, with -1 for anti-correlation, 0 for no correlation, and +1 for perfect correlation. The data suggests the correlations of signals between RNPs and endosomes and those between RNPs and nuclei increased with longer incubation time, indicating increasing cellular uptake and nuclear transport of RNPs. (**b, c**) The Mander's colocalization coefficient (MCC) ranges from 0 to 1, quantifying the fraction of intensity of one color that is co-localized with the other color in the same pixel of the image. (**b**) The MCC suggests more RNPs were distributed in endosomes than those in nuclei at 0.5 and 2 h post-treatment, but more RNPs were colocalized with nuclei at 4 h post-treatment, indicating effective endosomal escape and nuclear transport of RNPs. (**c**) The MCC suggests that the overlap between signals from endosomes or nuclei and signals from RNP increased with incubation time, as the result of continuous cellular uptake and nuclear transport of RNPs. The MCCs of (b) and (c) are defined as:

$$\text{for (b), } \mathrm{MCC} = \frac{\sum \mathrm{RNP\ (signals\ colocalized\ with\ endosomes\ or\ nuclei)}}{\sum \mathrm{RNP\ (all\ signals)}}$$

$$\text{for (c), MCC} = \frac{\sum \text{endosomes or nuclei (signals colocalized with RNP)}}{\sum \text{endosomes or nuclei (all signals)}}$$

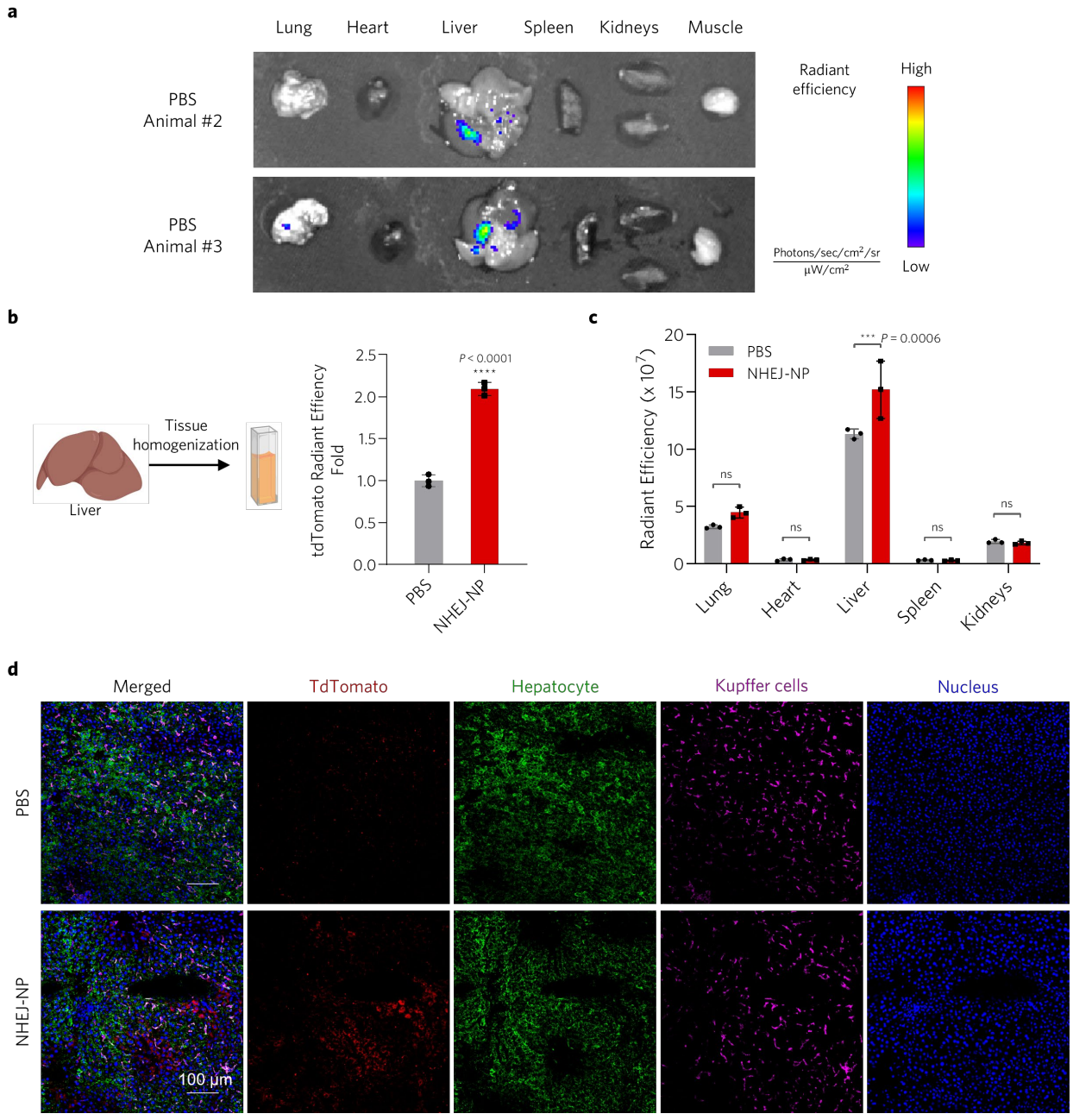

Figure 2.11 | Supplementary liver data from Ai14 mice i.v. injected with NHEJ-NP.

a, IVIS images acquired from the other two PBS-injected mice are presented, supplementary to Figure 3c. **b,** The fluorescence intensities of the homogenized suspension from livers of the PBS-injected and NHEJ-NP-injected mice. The tdTomato fluorescence intensity was 2-fold higher than the PBS-injected group. Data are presented as mean ± s.d. (n=3). Statistical significance was calculated via a t-test. ****$P < 0.0001$. **c,** The radiant efficiency of tdTomato in major organs. Significant tdTomato fluorescence enhancement was only found in liver, not other organs. **d,** Immunofluorescence staining of the liver sections from the PBS-injected and NHEJ-NP-injected mice shows robust gene editing in liver. Sections were stained with anti-RFP antibodies for tdTomato (red), anti-hepatocyte specific antigen (green), anti-F4/80 antibodies for Kupffer cells (magenta, pseudo-color), and DAPI for nuclei (blue), respectively. Representative images are shown. Scale bar: 100 μm. Data are presented as mean ± s.d. (n=3). Statistical significance was calculated via (b) t-test or (c) two-way ANOVA with Tukey's post hoc test. ***P < 0.001. ns, not significant. IVIS, in vivo imaging systems.

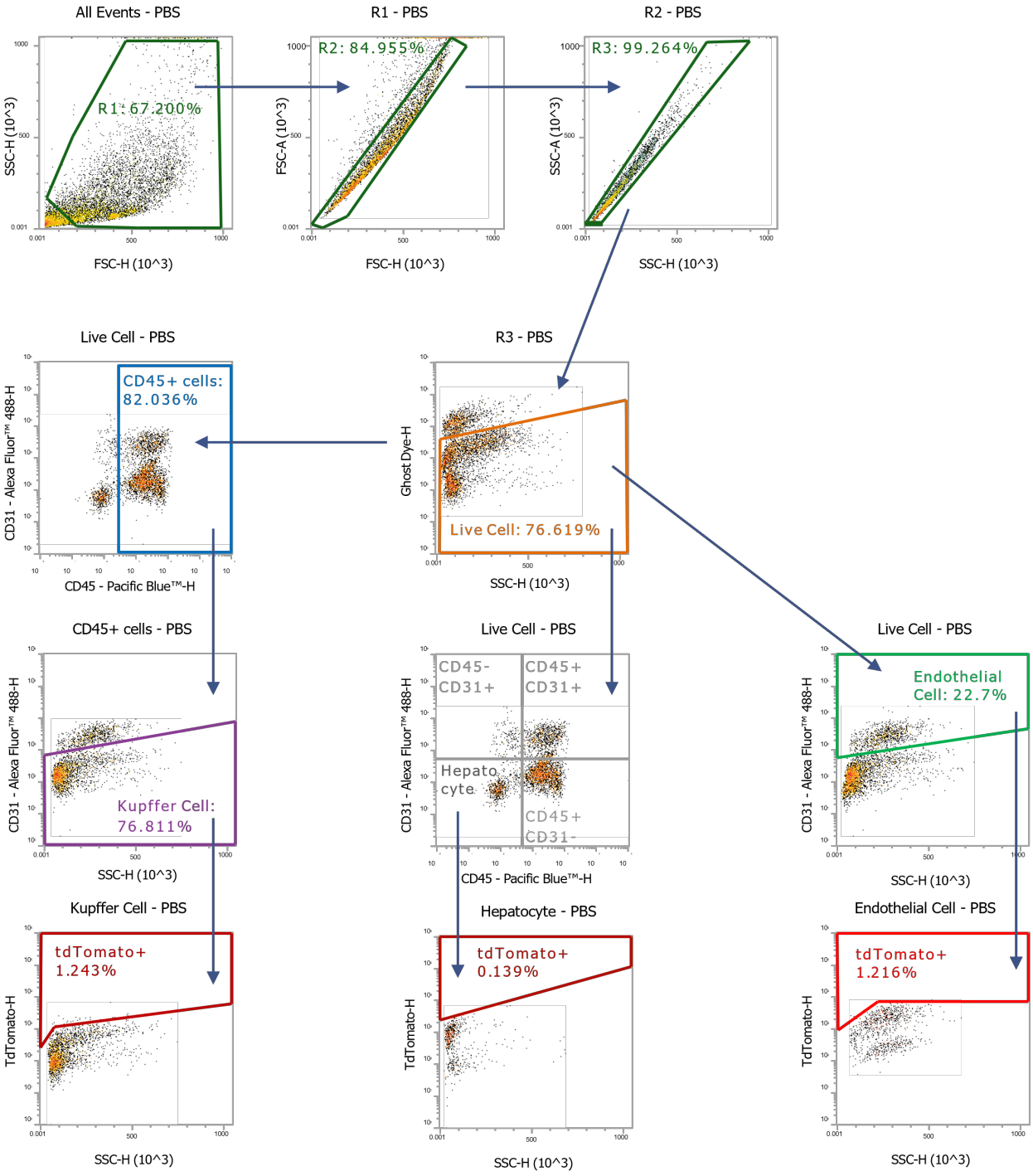

Figure 2.12 | The gating strategy for flow cytometry analyzing liver cells from Ai14 mice.

Markers for live cells (Ghost Dye Red 780), endothelial cells (Alexa Fluor 488-conjugated anti-CD31 antibodies), Kupffer cells (Pacific blue-conjugated anti-CD45 antibodies) were used to

distinguish cell types. Data shown here was from one Ai14 mouse which received an intravenous injection of PBS on Day 0, with its cells collected and analyzed on Day 7.

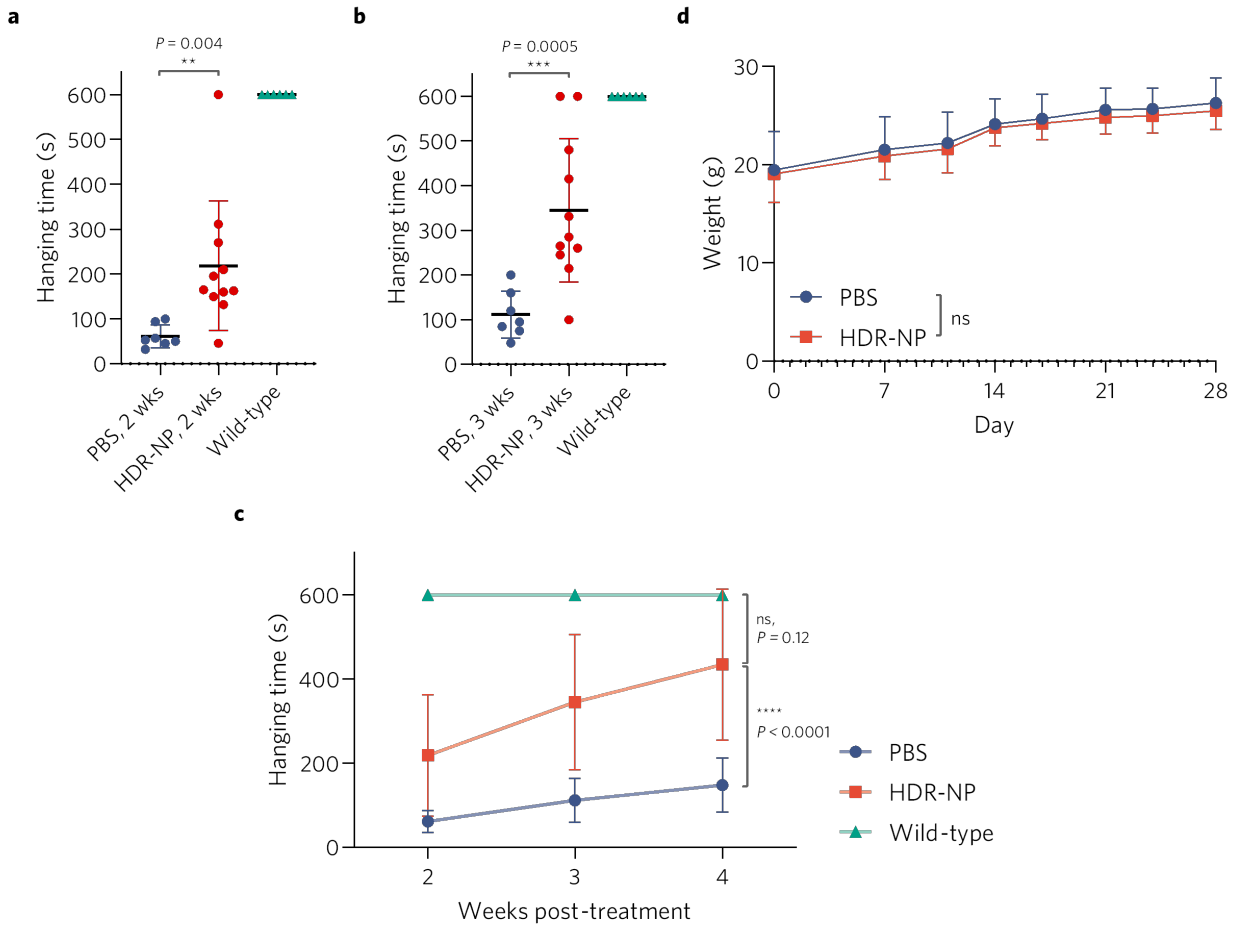

Figure 2.13 | Change of hanging times and body weights for mdx mice with or without HDR-NP treatment.

a-c, The four-limb hanging time assay of the PBS-injected *mdx* mice (n = 7, negative control), HDR-NP-injected *mdx* mice (n = 11), and untreated wild-type mice (n = 6, positive control) demonstrates the restoration of muscle strength of *mdx* mice (**a**) 2 weeks and (**b**) 3 weeks after injections with HDR-NPs. (**c**) The hanging time changes for all tested mice are summarized. **d,**

The body weights of PBS-injected and HDR-NP-injected *mdx* mice. Data are presented as mean ± s.d. Statistical significance was calculated via (**a, b**) one-way or (**c, d**) two-way ANOVA with Tukey's post hoc test. **P* < 0.05, ***P* < 0.01, ****P* < 0.001, *****P* < 0.001. ns, not significant.

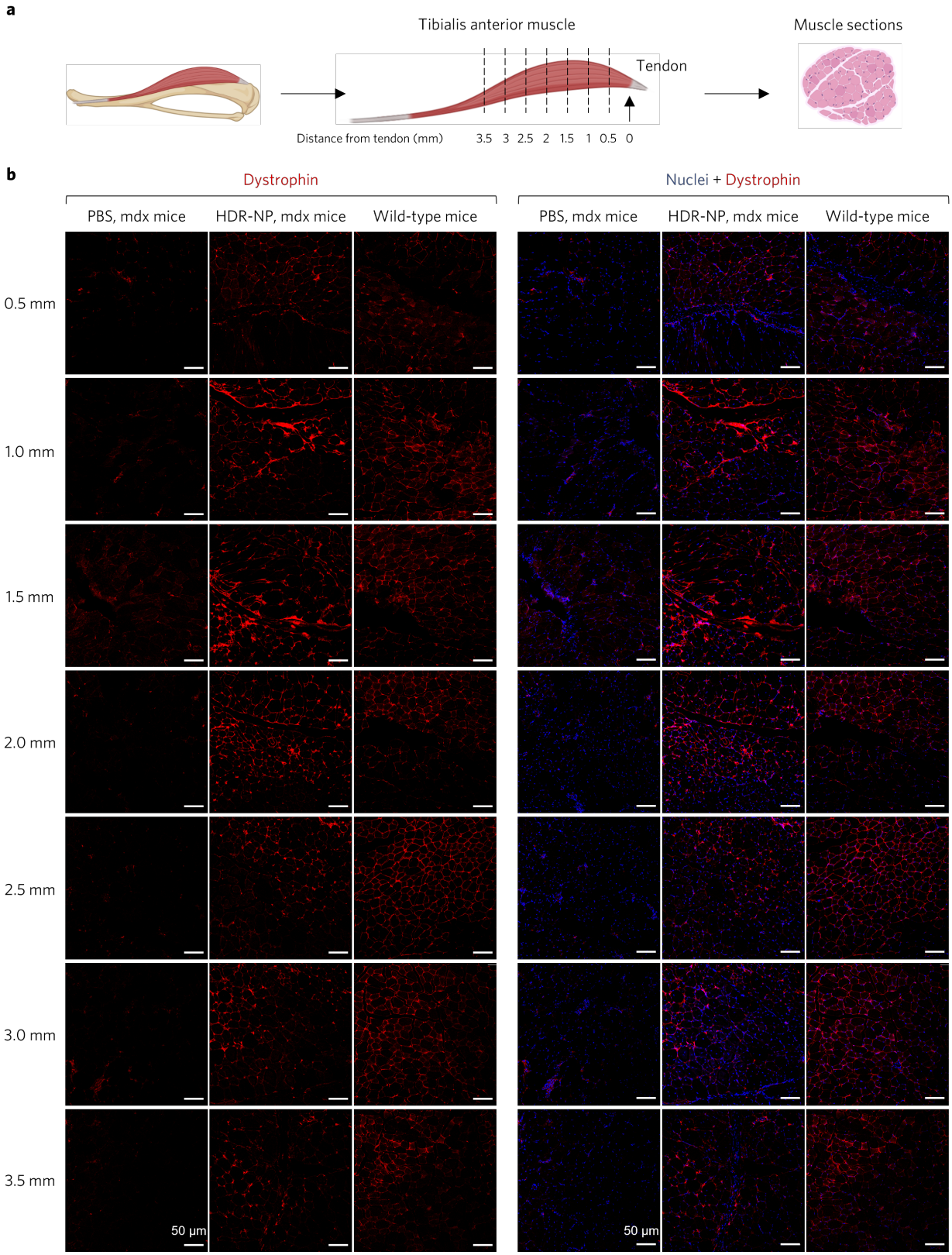
a
Tibialis anterior muscle
Muscle sections
Tendon
Distance from tendon (mm)
3.5 3 2.5 2 1.5 1 0.5 0
b
Dystrophin
Nuclei + Dystrophin
PBS, mdx mice
HDR-NP, mdx mice
Wild-type mice
0.5 mm
1.0 mm
1.5 mm
2.0 mm
2.5 mm
3.0 mm
3.5 mm
50 µm
50 µm

Figure 2.14 | Immunofluorescence staining of dystrophin in TA muscle sections collected at different distances away from tendon.

a, Tibialis anterior muscle sections were collected by sectioning the muscle at different distances from tendon. **b**, The distribution of dystrophin expression within the tibialis anterior muscle sections collected at different distances from the tendon. Immunofluorescence staining of muscle sections from the PBS-injected and HDR-NP-injected *mdx* mice and untreated wild-type mice was performed. Muscle sections were stained with anti-dystrophin antibodies for dystrophin (red) and DAPI for nuclei (blue), respectively. Results indicate robust restoration of dystrophin expression after HDR-NP treatments almost in the entire muscle. Representative images are presented. Scale bar: 50 μm.

PBS,
mdx mice

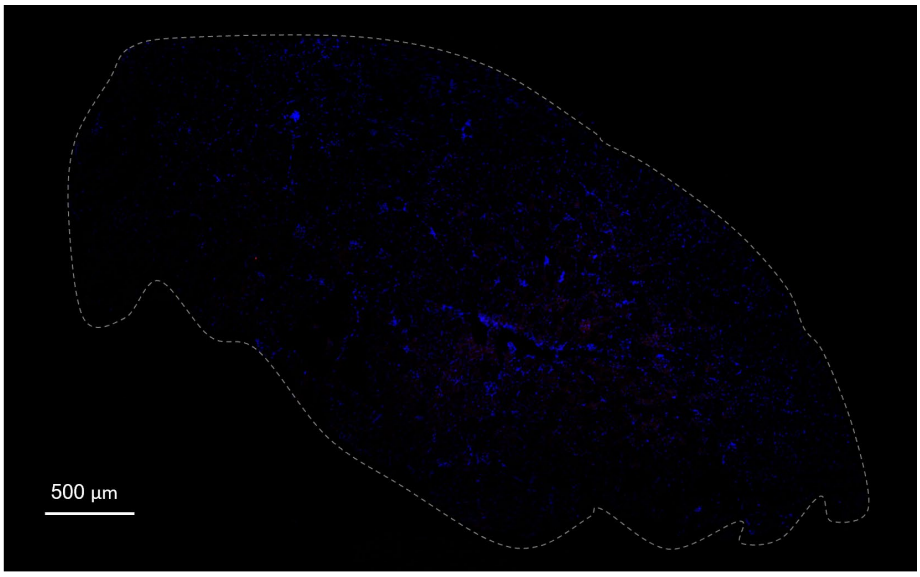

HDR-NP,
mdx mice

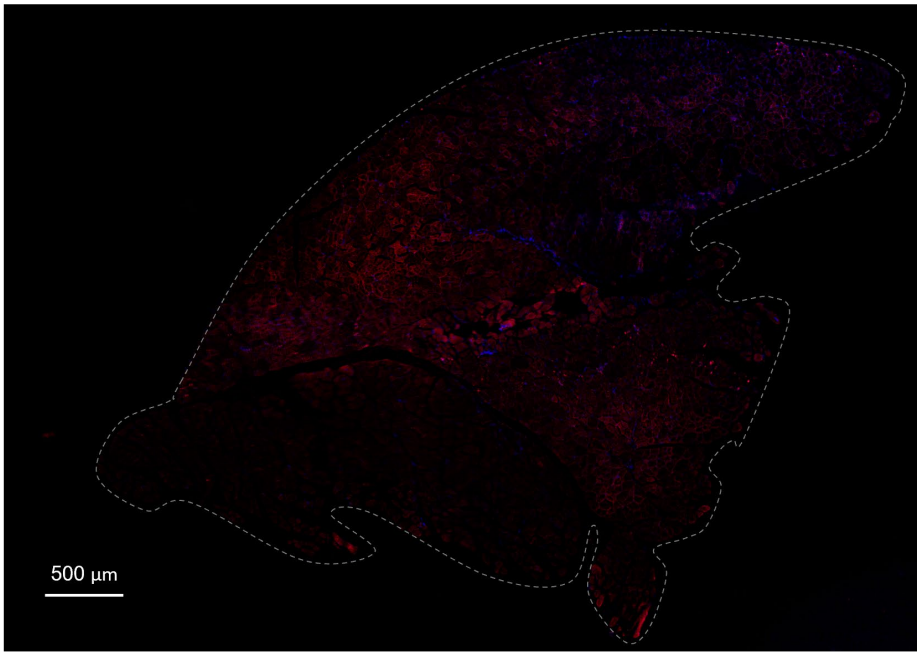

Untreated,
wild-type mice

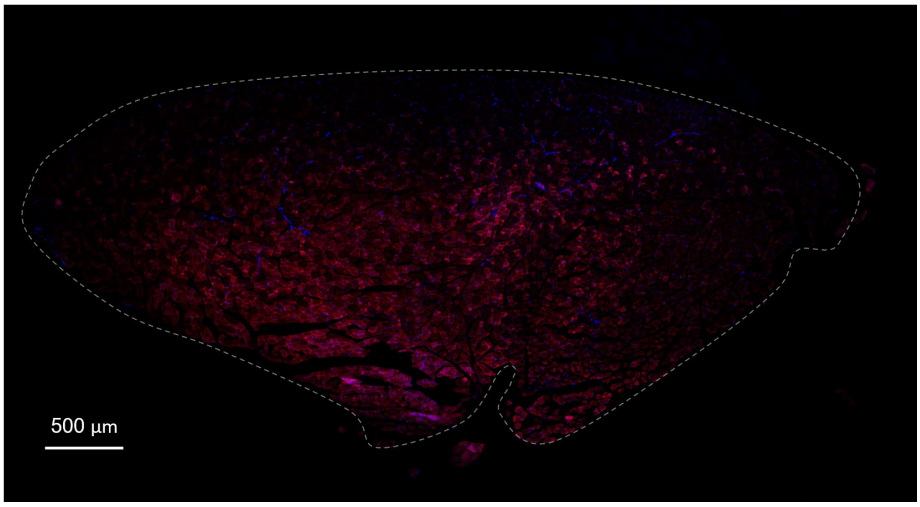

Figure 2.15 | Immunofluorescence staining of dystrophin in whole TA muscle sections.

The distribution of dystrophin expression within tibialis anterior muscle sections was investigated. Immunofluorescence staining of sections from the PBS-injected and HDR-NP-injected *mdx* mice and untreated wild-type mice was performed. Muscle sections were stained with anti-dystrophin antibodies for dystrophin (red) and DAPI for nuclei (blue), respectively. Results indicate robust restoration of dystrophin expression after HDR-NP treatments almost in the entire muscle. All three TA sections were located ~2.0 mm away from the tendon. Contours of muscle sections are labeled with dotted lines. Scale bar: 500 μm.

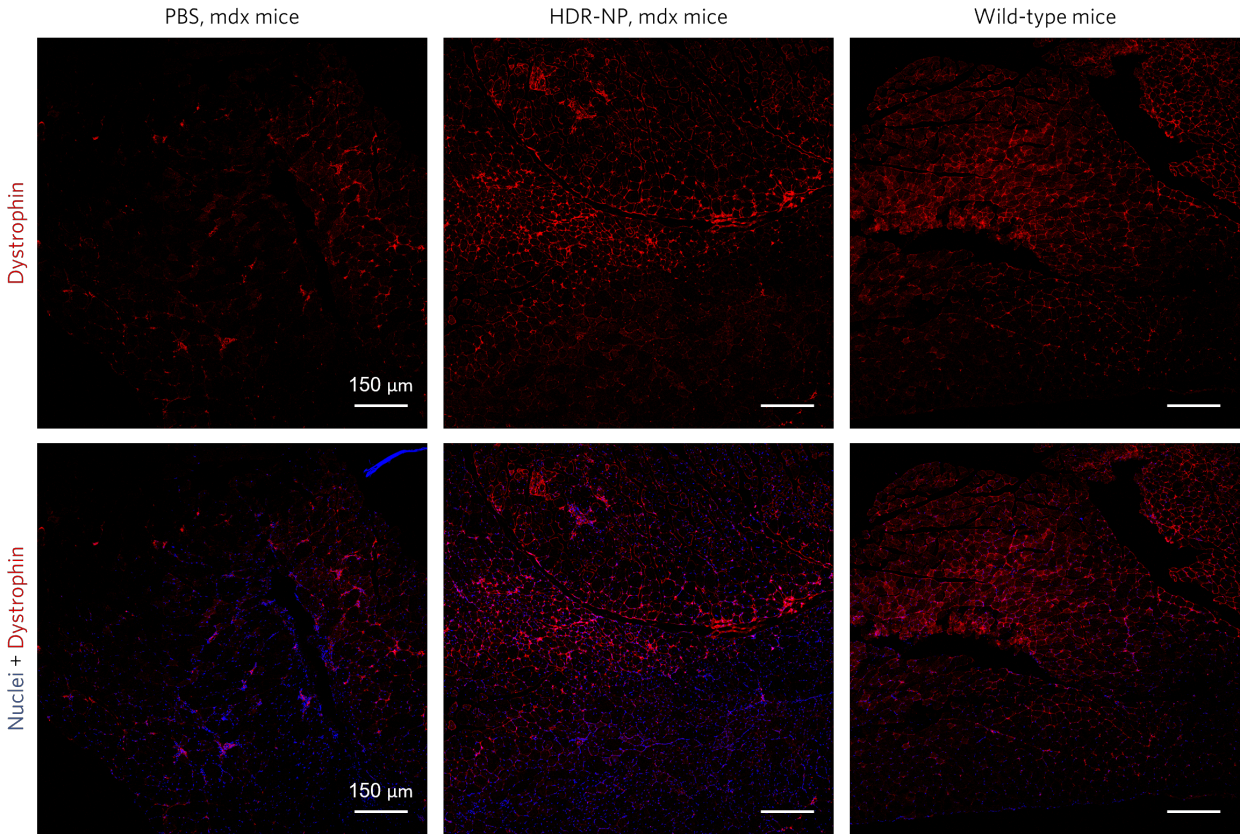

Figure 2.16 | Immunofluorescence staining of dystrophin in TA muscle at low magnification.

Immunofluorescence staining of sections from the PBS-injected and HDR-NP-injected *mdx* mice and untreated wild-type mice was performed. Muscle sections were stained with anti-dystrophin antibodies for dystrophin (red) and DAPI for nuclei (blue), respectively. Results indicate robust restoration of dystrophin expression after HDR-NP treatments in the muscle section (presented image size: 1.1 mm x 1.1 mm). Representative images are presented. Scale bar: 150 µm.

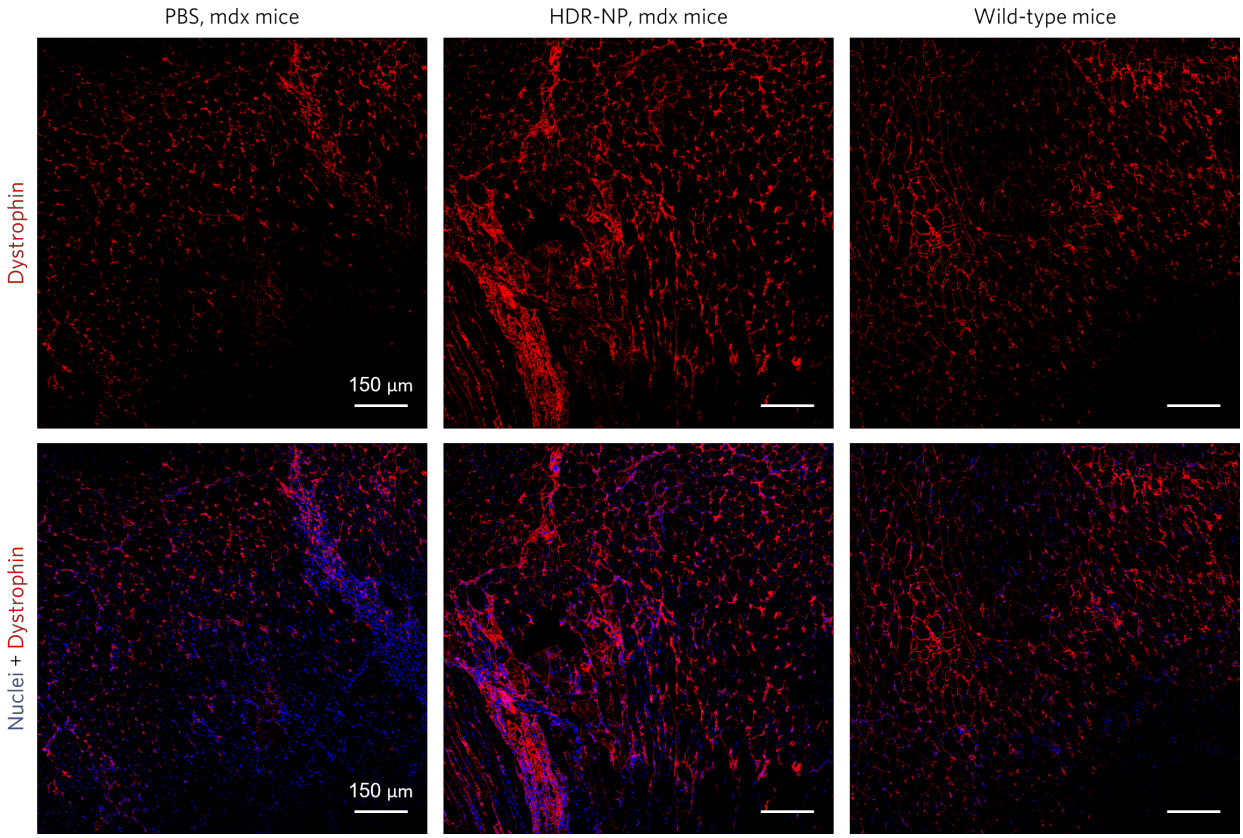

Figure 2.17 | Immunofluorescence staining of dystrophin in triceps brachii muscle at low magnification.

Immunofluorescence staining of sections from the PBS-injected and HDR-NP-injected *mdx* mice and untreated wild-type mice was performed. Muscle sections were stained with anti-dystrophin antibodies for dystrophin (red) and DAPI for nuclei (blue), respectively. Results indicate robust restoration of dystrophin expression after HDR-NP treatments in the muscle section (presented image size: 1.1 mm x 1.1 mm). Representative images are presented. Scale bar: 150 µm.

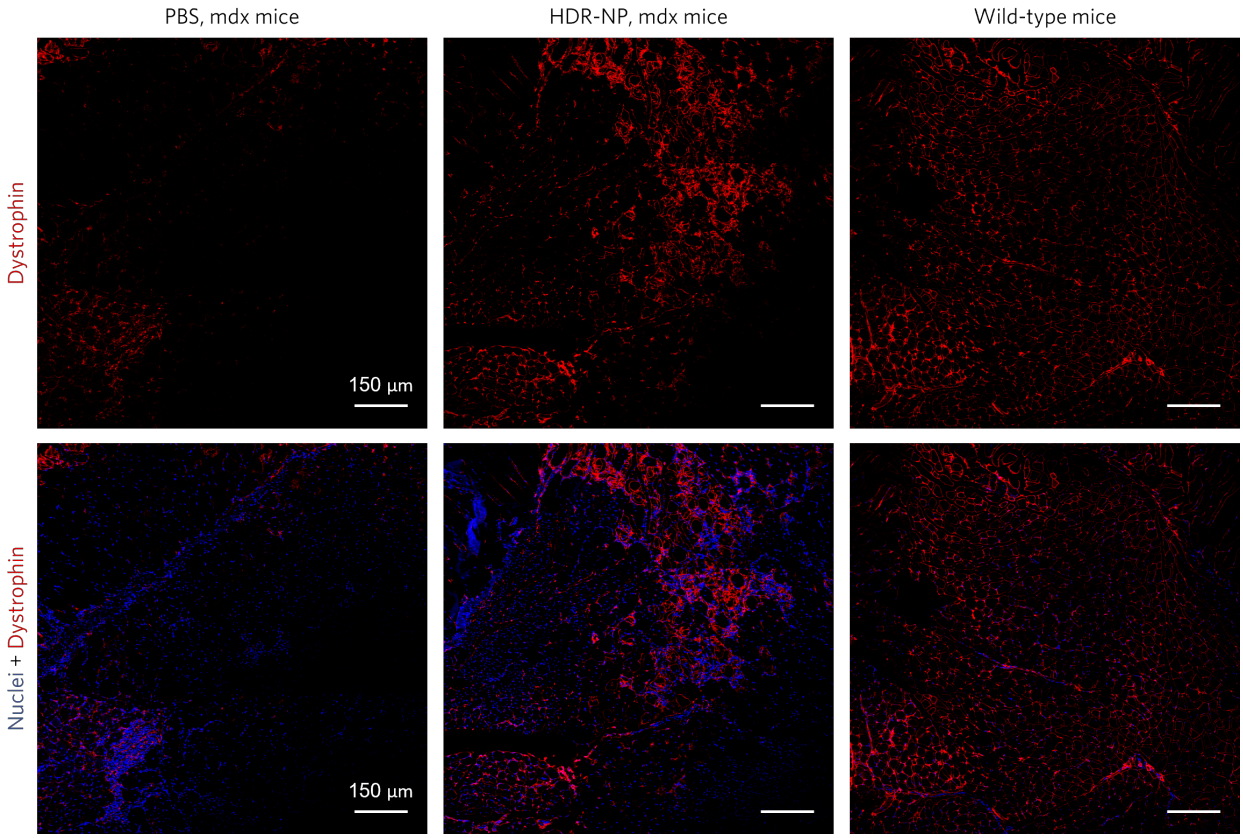

Figure 2.18 | Immunofluorescence staining of dystrophin in gastrocnemius muscle at low magnification.

Immunofluorescence staining of sections from the PBS-injected and HDR-NP-injected *mdx* mice and untreated wild-type mice was performed. Muscle sections were stained with anti-dystrophin antibodies for dystrophin (red) and DAPI for nuclei (blue), respectively. Results indicate robust restoration of dystrophin expression after HDR-NP treatments in the muscle section (presented image size: 1.1 mm x 1.1 mm). Representative images are presented. Scale bar: 150 µm.

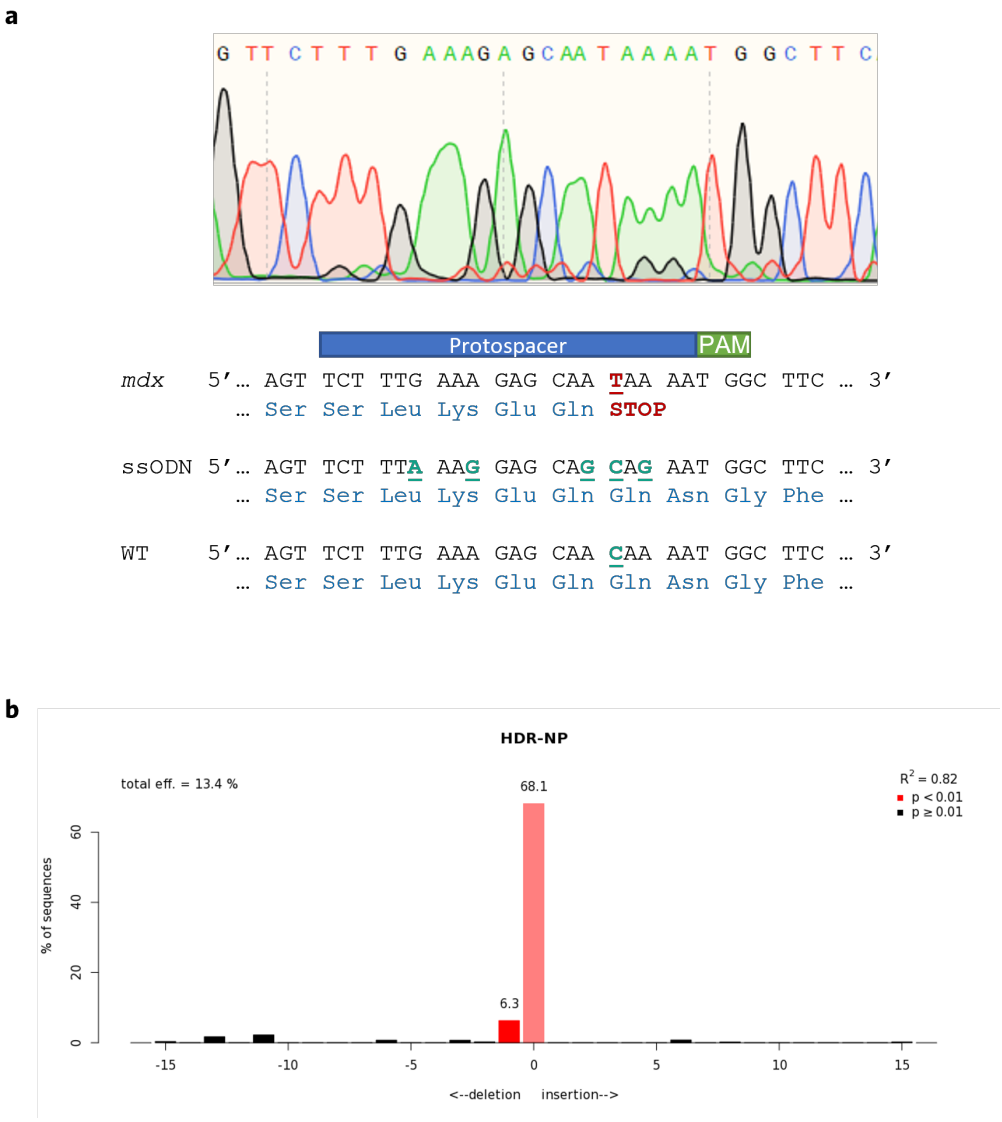

Figure 2.19 | Sanger sequencing of genomic DNA from TA muscle of PBS- or HDR-NP-injected *mdx* mice.

The in vivo gene editing efficiency of HDR-NP in TA muscle of *mdx* mice was analyzed by Sanger sequencing. *Mdx* mice possess a nonsense mutation in exon 23 in *Dmd* gene. HDR-NP-mediated gene editing via either HDR or NHEJ can correct or disrupt this nonsense mutation, and lead to restoration of dystrophin expression. (**a**) Sanger sequencing results indicate that HDR-NP induced

2.6% HDR and 13.3% NHEJ in TA muscles. (**b**) The profile of insertions and deletions in the edited sample was analyzed by TIDE.

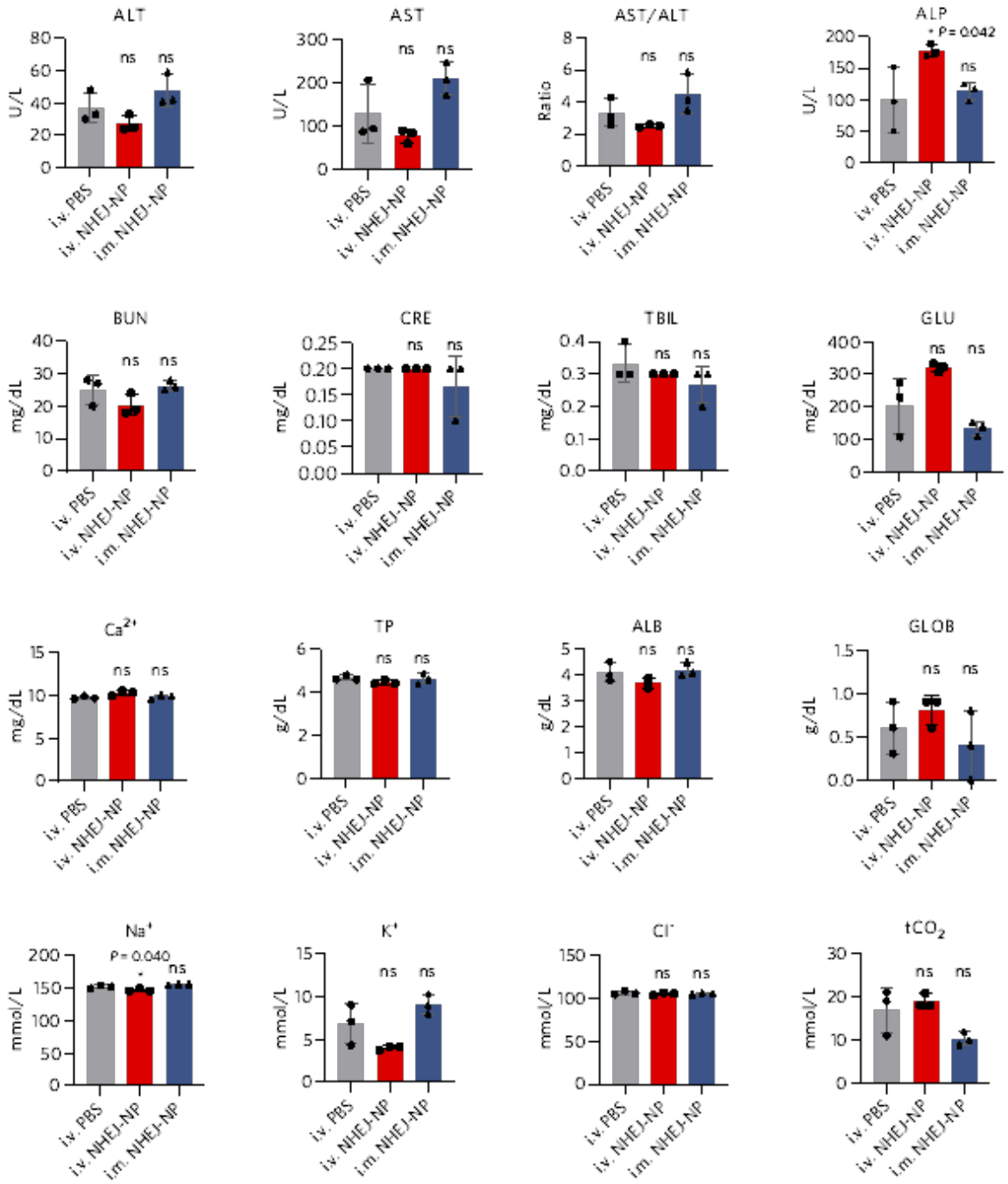

Figure 2.20 | The blood biochemical parameter panel for NHEJ-NP injected Ai14 mice.

Fresh whole blood was collected from Ai14 mice on Day 7. No significant variations in these biochemical parameters were found in animals treated with NHEJ-NPs via both administration

routes. ALT, alanine aminotransferase. AST, aspartate aminotransferase. AST/ALT, the ratio of AST/ALT. ALP, alkaline phosphatase. BUN, blood urea nitrogen. CRE, creatinine. TBIL, total bilirubin. GLU, glucose. Ca^{2+}, total calcium. TP, total protein. ALB, albumin. GLOB, globulin. Na^{+}, sodium. K^{+}, potassium. Cl^{-}, chloride. tCO_2, total carbon dioxide. Data are presented as mean ± s.d. (n=3). Statistical significance was calculated with PBS-injected as the control via one-way ANOVA with Tukey's post hoc test. $*P < 0.05$. ns, not significant.

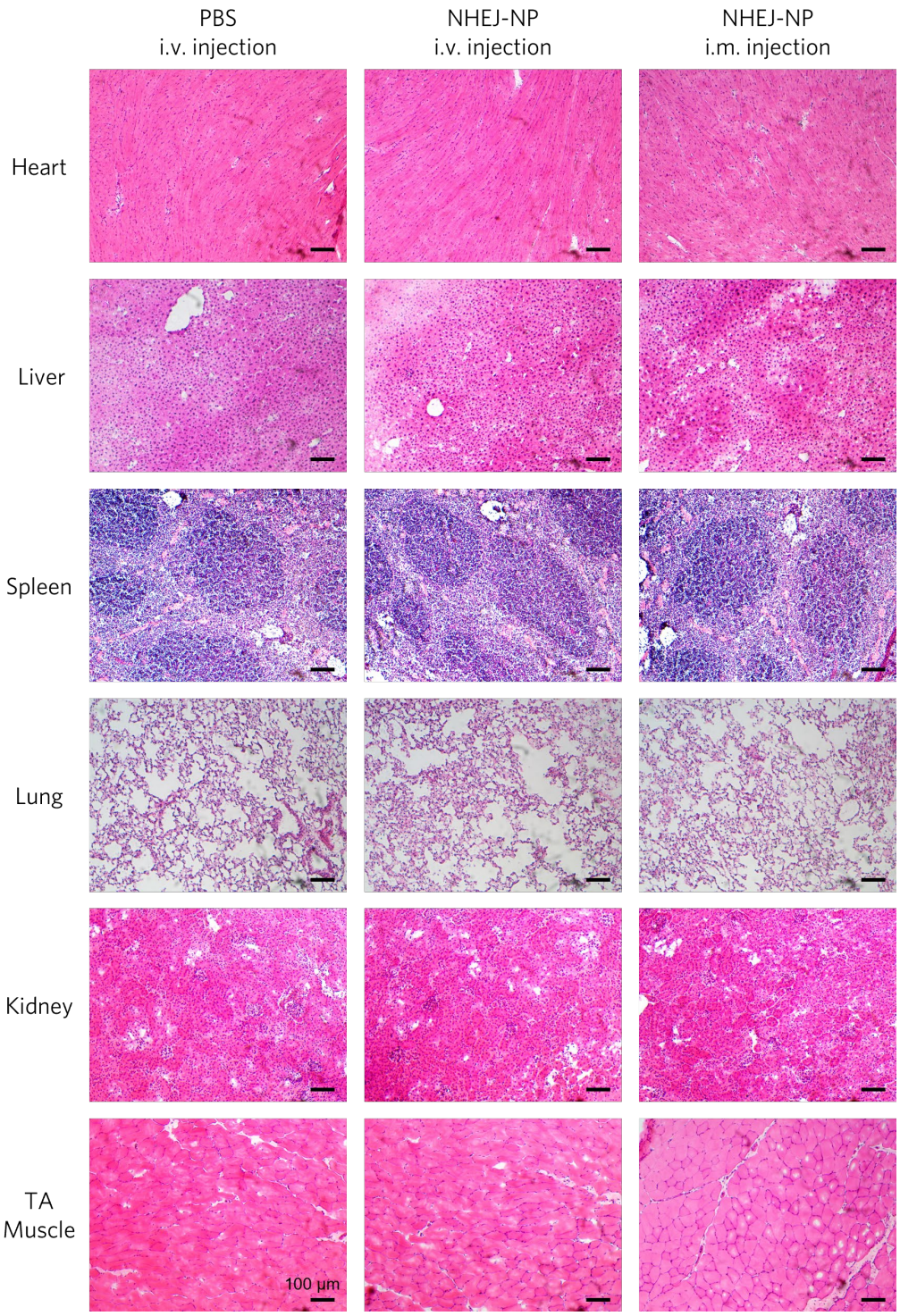

Figure 2.21 | H&E staining for major organs and TA muscles from PBS-injected and NHEJ-NP injected Ai14 mice.

No pathological changes were found in the mouse major organs and muscles treated with NHEJ-NPs through both i.v. and i.m. injections. TA, tibialis anterior. i.v., intravenous. i.m., intramuscular. Scale bar: 100 μm.

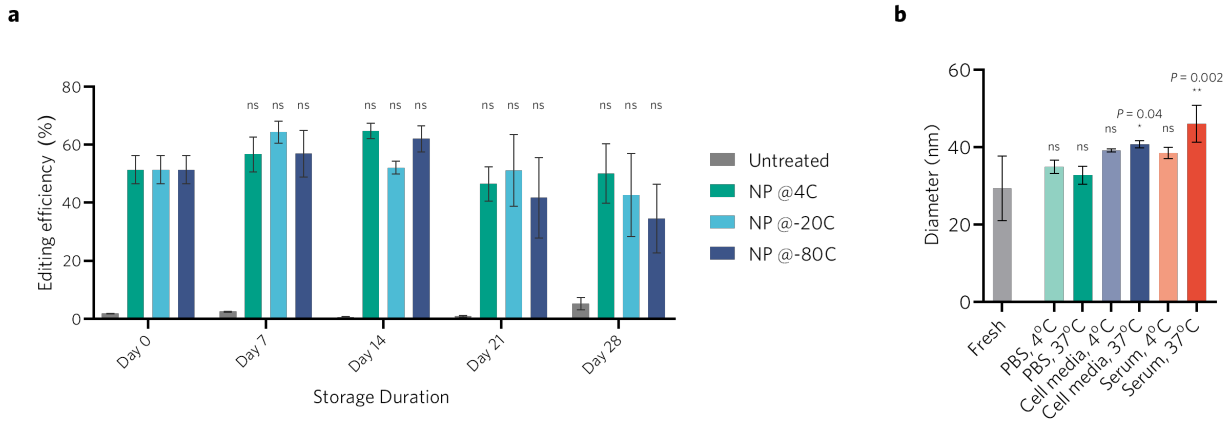

Figure 2.22 | The stability and storability of NHEJ-NP.

a, The NHEJ-NP was stored in Tris-EDTA buffer (pH 7.5) with 8% (v/v) glycerol at different temperatures for certain durations and then was used to treat BFP-HEK 293 cells. The editing efficiency was assayed by flow cytometry to quantify BFP-negative cells. Data are presented as mean ± s.d. (n = 3). **b,** The size variation of NHEJ-NP was studied in PBS, serum-containing cell culture media, and serum solutions at 4 ºC and 37 ºC, respectively. DLS data were collected 24 h after storage. The NHEJ-NP exhibits good stability against serum at 4ºC, but showed an increased particle size at 37 ºC. Data are presented as mean ± s.d. Statistical significance was calculated using "Fresh" or "Day 0" as the control via (**a**) one-way ANOVA or (**b**) two-way ANOVA with Tukey's post hoc test. *$P < 0.05$, **$P < 0.01$. ns, not significant. Serum was prepared by dissolving bovine serum albumin in PBS at 40 mg/mL.

2.6 Supplementary Tables

Table 2.1 | Protospacers of sgRNAs.

Gene	Protospacer (5' to 3')
GFP	GCACGGGCAGCTTGCCGG
BFP	GCTGAAGCACTGCACGCCAT
SV40 PolyA (Ai14)	AAGTAAAACCTCTACAAATG
Dmd	TCTTTGAAAGAGCAATAAAA

Table 2.2 | Sequences of ssODNs.

Gene	Sequence (5' to 3')
BFP	AAGTTCATCTGCACCACCGGCAAGCTGCCGGTGCCCTGGCCCACCCTCGTGACCACC CTGACGTACGGCGTGCAGTGCTTCAGCCGCTACCCCGACC
Dmd	TGATATGAATGAAACTCATCAAATATGCGTGTTAGTGTAAATGAACTTCTATTTAAT TTTGAGGCTCTGCAAAGTTCTTTAAAGGAGCAGCAGAATGGCTTCAACTATCTGAGT GACACTGTGAAGGAGATGGCCAAGAAAGCACCTTCAGAAATATGCCAGAAATATCTG TCAGAATTT

Table 2.3 | Sequences of primers for PCR and RT-PCR.

Gene	Sequence (5' to 3')
Dmd	GCGTGTTAGTGTAAATGAACTTCTA
	CCACCAACTGGGAGGAAAG
GAPDH	TGAGGCCGGTGCTGAGTATGTCG
	CCACAGTCTTCTGGGTGGCAGTG

Eotaxin	GCTACAGGAGAATCACCAGTGG
	GGAATCCTGCACCCACTTCTTC
IFN-γ	CAGCAACAGCAAGGCGAAAAAGG
	TTTCCGCTTCCTGAGGCTGGAT
IL-1α	CGAAGACTACAGTTCTGCCATT
	GACGTTTCAGAGGTTCTCAGAG
IL-1β	TGGACCTTCCAGGATGAGGACA
	GTTCATCTCGGAGCCTGTAGTG
IL-6	CTGCAAGAGACTTCCATCCAG
	AGTGGTATAGACAGGTCTGTTGG
IL-9	TCCACCGTCAAAATGCAGCTGC
	CCGATGGAAAACAGGCAAGAGTC
IL-10	CGGGAAGACAATAACTGCACCC
	CGGTTAGCAGTATGTTGTCCAGC
IL12-p35	ACGAGAGTTGCCTGGCTACTAG
	CCTCATAGATGCTACCAAGGCAC
IL12-p40	TTGAACTGGCGTTGGAAGCACG
	CCACCTGTGAGTTCTTCAAAGGC
IL-13	AACGGCAGCATGGTATGGAGTG
	TGGGTCCTGTAGATGGCATTGC
IL-17A	GAAGCTCAGTGCCGCCA
	TTCATGTGGTGGTCCAGCTTT
CXCL1	TCCAGAGCTTGAAGGTGTTGCC

	AACCAAGGGAGCTTCAGGGTCA
CCL2	GCTACAAGAGGATCACCAGCAG
	GTCTGGACCCATTCCTTCTTGG
CCL3	ACTGCCTGCTGCTTCTCCTACA
	ATGACACCTGGCTGGGAGCAAA
CCL4	ACCCTCCCACTTCCTGCTGTTT
	CTGTCTGCCTCTTTTGGTCAGG
CCL5	CCTGCTGCTTTGCCTACCTCTC
	ACACACTTGGCGGTTCCTTCGA
TNF-α	GGTGCCTATGTCTCAGCCTCTT
	GCCATAGAACTGATGAGAGGGAG
NF-κB	CTGGCAGCTCTTCTCAAAGC
	TCCAGGTCATAGAGAGGCTCA

Chapter 3. An Injectable Hydrogel Capable of In Situ Covalent Crosslinking for Permanent Embolization

3.1 Introduction

Endovascular embolization has been a standard of care and well-established technique to treat internal bleeding, aneurysm, and vascular malformation, in which an occlusive material or agent is delivered into the target vessel through the catheter [21, 22]. Embolic materials can be categorized as solid materials (e.g., metallic coils) and liquid materials (e.g., Onyx^{TM}). Solid materials are considered to be effective in controlled and precise deployment into the target vessel, enabled by its radiopacity [23, 24]. Solid materials are thus preferred for precise occlusion of small aneurysms and bleeding arteries caused by vascular injury. The major disadvantage of solid materials is that it is difficult to achieve complete thrombosis of the vessel, especially in large vessels and aneurysms [25]. Additionally, other complications can occur after embolization with metallic coils, including coil migration and coil compaction. These metallic coils can also produce extensive streak artifacts and thus cause interference of accurate follow-up assessment of the treated area with imaging techniques including fluoroscopy, computerized tomography (CT), and magnetic resonance imaging (MRI). Particularly, for endovascular treatment of large aneurysms (e.g., abdominal aortic aneurysms), the use of metallic coils can lead to lengthy and costly procedures [32]. In contrast to solid embolic materials, the major advantage of liquid embolic materials is the quick inducement of thrombosis of the target vessel. Liquid materials also have the capability to occlude large vessels and arteriovenous malformations and manage endoleak during or after endovascular aortic aneurysm repair (EVAR) [26-29]. However, liquid embolic materials are difficult to deploy in a controlled manner. They may incidentally embolize non-

targeted vessels [30], and/or cause dangerous entrapment of the delivering catheter which may lead to surgical difficulties [31]. Complications including recanalization and incomplete embolization can happen.

To resolve limitations of solid embolic materials and liquid embolic agents, we sought to develop an embolic material that can (1) be deployed via needles or catheters; (2) maintain mechanical stability and integrity and remain at the injection site after deployment; (3) rapidly induce blood coagulation and thrombosis; (4) gradually induce fibrosis for permanent embolization and tissue regeneration; (5) allow visibility during endovascular surgery by X-ray imaging for target deployment; and (6) possess good biocompatibility. One type of materials that are of particular interest for our design criteria is hydrogel. Injectable hydrogels and in situ gelling hydrogels formed by liquid precursors can potentially fulfill these requirements, taking advantages of their tunable viscoelastic nature and chemical versatility. Up to date, several hydrogel systems have been reported for endovascular embolization [25, 32-37]. However, previously reported hydrogel systems still have room to improve to fulfill clinical requirements. Hydrogels that are formed in situ typically require two respective injections or a double-lumen syringe to administrate liquid hydrogel precursors, which can complicate the deployment process and induce undesirable off-target embolization. Hydrogels formed only by physical interactions for crosslinking are less reliable than the ones with covalently crosslinked structures in terms of mechanical stability for long-term embolization. Additionally, embolization that relies on tissue fibrosis instead of physical occlusion by embolic materials is more desirable for permanent embolization and tissue regeneration.

To achieve injectability through needles and catheters, the hydrogel should exhibit a shear-thinning behavior. However, while the hydrogel needs to be extruded and deployed easily through a shear

force generated by physicians using a catheter during surgery, the hydrogel also needs to possess sufficient mechanical strength and modulus to withstand the shear force from blood flow and body movement of the patient after surgery. In fact, in most cases, the need for hydrogel injectability is only one time. These seemingly contradictory requirements can be resolved by an initially injectable hydrogel that can be retained at the injection site and then undergo in situ covalent crosslinking under physiological conditions, which can lead to enhanced mechanical stability. To achieve in situ covalent crosslinking, thiol-ene coupling via a Michael-addition reaction can be a promising approach due to its biocompatible nature for in vivo applications [54, 55]. Notably, the thiol-ene reaction kinetics is highly tunable by adjusting the pH value, the molar ratio of thiol to ene groups, and the chemical structure of the alkene groups. We hypothesized that methacrylate groups are suitable for our purpose because previous studies demonstrated that the coupling reaction between thiol and methacrylate groups takes 30 to 60 min, which can not only provide an operation window for endovascular surgery but is also rapid enough for in situ covalent crosslinking [54, 55].

In this work, we designed an injectable hydrogel that is robust enough to remain at the target site upon injection and subsequently undergoes in situ covalent crosslinking, leading to the formation of a dual-crosslinking network (DCN) hydrogel (**Figure 3.1**). The DCN hydrogel was formed through two sequential crosslinking processes: the initial reversible crosslinking process to achieve shear-thinning property and hence injectability, and the secondary irreversible in situ covalent crosslinking to achieve desirable mechanical property. The alginate-calcium sulfate hydrogel system was selected for this application due to its reversible crosslinking capability. Moreover, both alginate and calcium ions are able to promote hemostasis, which is an important property for embolic agents. Since the water solubility of alginate is limited, another biocompatible and

hemostatic polysaccharide, carboxymethylcellulose, was also mixed in the hydrogel matrix to strengthen the mechanical performance of the hydrogel both before and after deployment. To harness the secondary irreversible, in situ covalent crosslinking capability, both polysaccharides were covalently conjugated with methacrylate groups (i.e., Alg-MA and CMC-MA). Thiolate molecules (i.e., dithiothreitol (DTT)) and tris(2-carboxyethyl)phosphine (TCEP, a catalyst for thiol-ene reaction) were mixed in the formulated hydrogel prior to the injection. After injection and at 37 ºC, DTT rapidly reacts with the methacrylate groups on both Alg-MA and CMC-MA catalyzed by TCEP, forming a DCN hydrogel at the injection site within an hour, and thereby providing necessary mechanical properties and stability for endovascular embolization. The ease of injectability and the mechanical behavior after in situ covalent crosslinking were demonstrated by rheological studies and mechanical testing, respectively. The DCN hydrogel exhibited efficient hemostatic capability with good biocompatibility. Moreover, the DCN hydrogel was radiopaque, and thus allows X-ray imaging for target embolization during surgery. Endovascular embolization efficacy was finally evaluated in rabbit arteries in vivo, where the DCN hydrogel effectively embolized the arteries and induced tissue fibrosis and regeneration for permanent embolization.

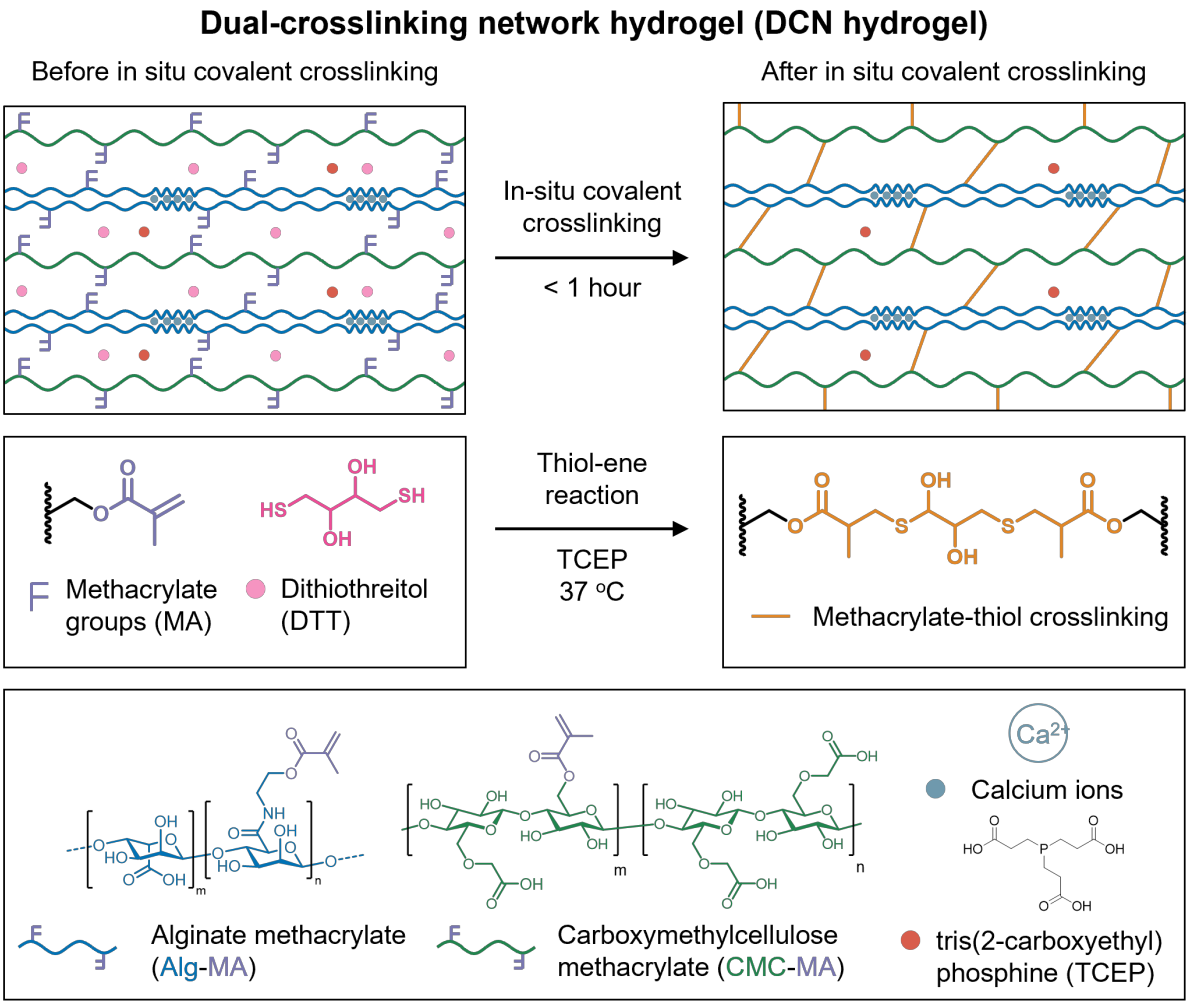

Figure 3.1 | Schematic illustration of the DCN hydrogel structure.

The DCN hydrogel is composed of two biocompatible polymers, i.e., alginate methacrylate (Alg-MA) and carboxymethylcellulose methacrylate (CMC-MA). The DCN hydrogel is formed via a two-step gelling process. First, calcium sulfate was mixed with Alg-MA and CMC-MA to generate a shear-thinning, and thus injectable hydrogel network through alginate-calcium coordination interactions. The injectable hydrogel is then mixed with dithiothreitol (DTT) and tris(2-carboxyethyl)phosphine (TCEP) right before injection. DTT serves as a crosslinker for in situ covalent crosslinking via a thiol-ene Michael-addition reaction. After injection and under

physiological conditions, the thiol groups in DTT can react with the methacrylate groups on both Alg-MA and CMC-MA catalyzed by TCEP, forming a DCN hydrogel at the injection site, thereby providing desirable mechanical properties and stability for endovascular embolization.

3.2 Results and Discussion

3.2.1 The DCN hydrogel can be synthesized, prepared, and applied straightforwardly.

As shown in **Figure 3.1**, the DCN hydrogel was formulated with two biocompatible polymers, i.e., alginate methacrylate (Alg-MA) and carboxymethylcellulose methacrylate (CMC-MA). Both polymers were synthesized through simple one-step modification of natural polysaccharides. Specifically, Alg-MA was synthesized by amidation between its carboxyl group with 2-aminoethyl methacrylate in an aqueous solution, with 27% substitution degree of methacrylate group (**Figure 3.8**). CMC-MA was synthesized by esterification between its β-hydroxyl group with methacrylic anhydride, with 18% substitution degree of methacrylate group (**Figure 3.9**). Both polymers were then purified by dialysis against ultrapure water and lyophilized as dry powders. To prepare the DCN hydrogel, solutions of Alg-MA and CMC-MA in triethanolamine (50 mM, pH 8.5) buffer were mixed with calcium sulfate ($CaSO_4$) suspension under mechanical stirring. The final concentrations of Alg-MA, CMC-MA, and $CaSO_4$ were 4%, 4%, and 0.8% (w/v), respectively. $CaSO_4$ crosslinked Alg-MA through alginate-calcium coordination interactions and generated a shear-thinning and injectable hydrogel network. The concentrations of these two components were determined based on previous work [56]. The CMC-MA macromolecules within this alginate-calcium matrix are not crosslinked at this stage. The injectable hydrogel was mixed with dithiothreitol (DTT, a thiolate crosslinker) and tris(2-carboxyethyl)phosphine (TCEP, a catalyst)

before injection to activate the in situ Michael-addition crosslinking reaction between CMC-MA, Alg-MA, and DTT. The addition of TCEP at 2.5 mM as a catalyst can significantly accelerate the in situ thiol-ene reaction [55, 57]. The thiol-ene reaction in the as-prepared DCN hydrogel can be halted at 4ºC for more than one hour without inducing premature crosslinking or impacting its in situ covalent crosslinking capability, thereby providing a time window for surgical operation. Right before use, the pre-mixed DCN hydrogel was warmed at 37 ºC. Thereafter, upon deployment, the body temperature at 37 ºC triggered in situ thiol-ene reactions between DTT and the methacrylate groups on Alg-MA and CMC-MA, leading to a covalently crosslinked tough hydrogel within one hour after deployment. Notably, preparation of the DCN hydrogel only involves dissolving the Alg-MA and CMC-MA polymers and mixing the polymer solution with $CaSO_4$, DTT, and TCEP, and the in situ covalent crosslinking can be inhibited at low temperature (i.e., $\leq$ 4 ºC). Thus, the DCN hydrogel is easy to prepare, store, transport, and use, all desirable features for clinical translation.

3.2.2 The DCN hydrogel can be easily injected via needles or catheters and rapidly crosslinked in situ upon injection.

Even without in situ covalent crosslinking, the hydrogel crosslinked with only the alginate-calcium coordination interaction was already visually observed as a solid hydrogel instead of a liquid polymer solution. It was able to stay at the bottom of a centrifuge tube which was placed upside down for 7 days at 20 ºC without flowing down, and still injectable thereafter (**Figure 3.2A**). Due to its shear-thinning property resulting from the alginate-calcium interactions, we predicted that the DCN hydrogel can be injectable using needles and catheters. The injectability of the DCN

hydrogel was first investigated by manual injections. The DCN hydrogel can be injected easily via needles at 18-, 22-, and 26-gauge (**Figure 3.2B**). It can also be smoothly injected with a single hand through a 6-French catheter that is 1.25 meters long, which is used clinically for endovascular surgeries in patients (**Figure 3.2C**). To quantitatively study the influence of injection conditions on the injection force required for the DCN hydrogel, the injection forces under different injection conditions were measured using a mechanical tester by varying the size of the needle, the rate of injection, and the volume of the syringe (**Figure 3.2D**). Under a specific set of injection conditions, the injection force increased linearly until it reached a plateau indicating the maximum force needed to extrude the DCN hydrogel from different types of needles or catheters. As expected, needles with smaller diameters required a higher force to inject the DCN hydrogel. It required 16.3 N for injection via a 26-gauge needle, but only 3.3 N via an 18-gauge one (**Figure 3.2E**). For injection via a 6-French catheter, a higher injection rate led to a higher injection force (**Figure 3.2F**). Using a 1-mL syringe, the DCN hydrogel required 12.4 N for injection at 0.1 mL/min, but 32.9 N for injection at 1.0 mL/min. The volume of the syringe for injection also mattered. When the injection rate was 0.1 mL/min, the force required to inject the DCN hydrogel with a 1-mL and a 3-mL syringe was 32.9 N and 36.0 N, respectively. Collectively, the forces needed to inject the DCN hydrogel were within the range that can be generated manually by a surgeon without the need for additional equipment, and the injection forces were tunable by varying injection conditions.

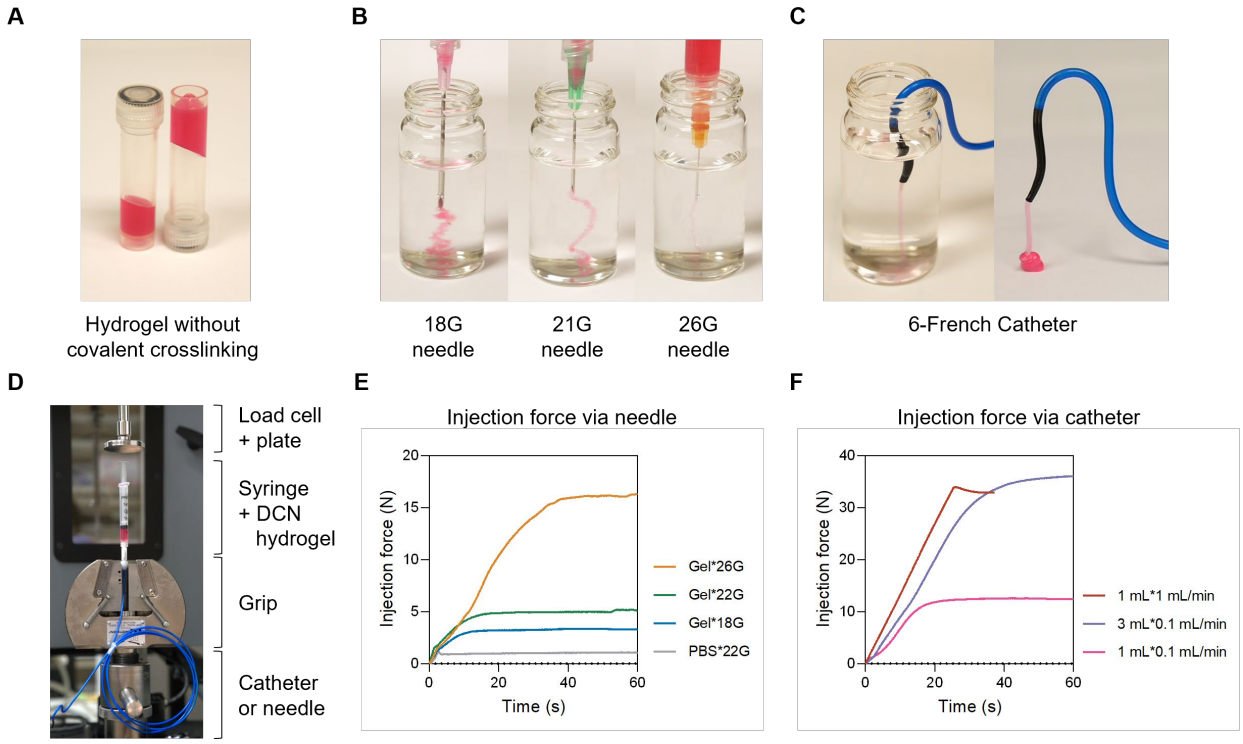

Figure 3.2 | Injectability studies of the DCN hydrogel.

(**A**) Even without covalent crosslinking, the hydrogel was able to stay at the bottom of a centrifuge tube that was placed upside down for 7 days at 20 ºC without flowing down, and still injectable thereafter. The DCN hydrogel can be injected via (**B**) needles (18-, 22- and 26-gauge) and (**C**) catheters (6-French) easily using a single hand. (**D**) An Instron mechanical test setup was built to measure the injection forces of the DCN hydrogel through (**E**) needles and (**F**) catheters, with different needle sizes, syringe types and injection rates.

The viscoelastic property of the hydrogel without in situ covalent crosslinking was first investigated by a rheometer [58]. Representative results from large strain sweep experiments of the hydrogel measured at 0.1 Hz and 37 ºC are shown in **Figure 3.3A**. To investigate the non-linear viscoelasticity, the storage (G') and loss (G") moduli of the DCN hydrogel were measured

at a fixed frequency (**Figure 3.3A**). The G' exceeded G" at small strains, indicating dominant elastic behavior. As the strain increased, both G' and G" decreased and they eventually intersected at a crossover strain (51.9%). Beyond the crossover strain, the G" exceeded G', indicating a dominant viscous response. The recovery of the DCN hydrogel moduli under alternating high (100%) and low strain (0.1%) was also tested (**Figure 3.3B**). At high strains, both G' and G" significantly decreased. At low strains, both G’ and G” increased and were able to recover around 86% of its original value. This demonstrated the capability of the DCN hydrogel to recover its stability and integrity after injection. Furthermore, the viscosity of the DCN hydrogel decreased as the shear rate increased, demonstrating its shear-thinning behavior before in situ covalent crosslinking (**Figure 3.3C**). G' and G" as a function of frequency are shown in **Figure 3.3D**. It can be observed that G' > G", indicating viscoelastic solid-like behavior.

To study the in situ covalent crosslinking reaction, the real-time rheological performance of the DCN hydrogel undergoing the thiol-ene reaction was monitored by measuring the variation in its moduli at 37 ºC (**Figure 3.3E**). Both the storage (G’) and loss moduli (G”) of the DCN hydrogel were gradually increased over time, indicating continuous in situ secondary crosslinking mediated by the thiol-ene reactions between the thiol groups on DTT and methacrylate groups on Alg-MA and CMC-MA. After ~45 min, increments of G’ and G” both reached plateaus indicating complete thiol-ene reactions. The stress-strain curve of in situ covalently crosslinked DCN hydrogel was studied by a mechanical tester (**Figure 3.3F**). The DCN hydrogel had a Young’s modulus of ~5.7 MPa with 234% elongation at break. The microstructure of the DCN hydrogel before and after in situ covalent crosslinking was observed by scanning electron microscopy (SEM) using lyophilized DCN hydrogel samples (**Figure 3.3G**). Observable topological and morphological changes including reduced mesh sizes and thickened polymer fibers were noted under SEM, as a result of

in situ covalent crosslinking.

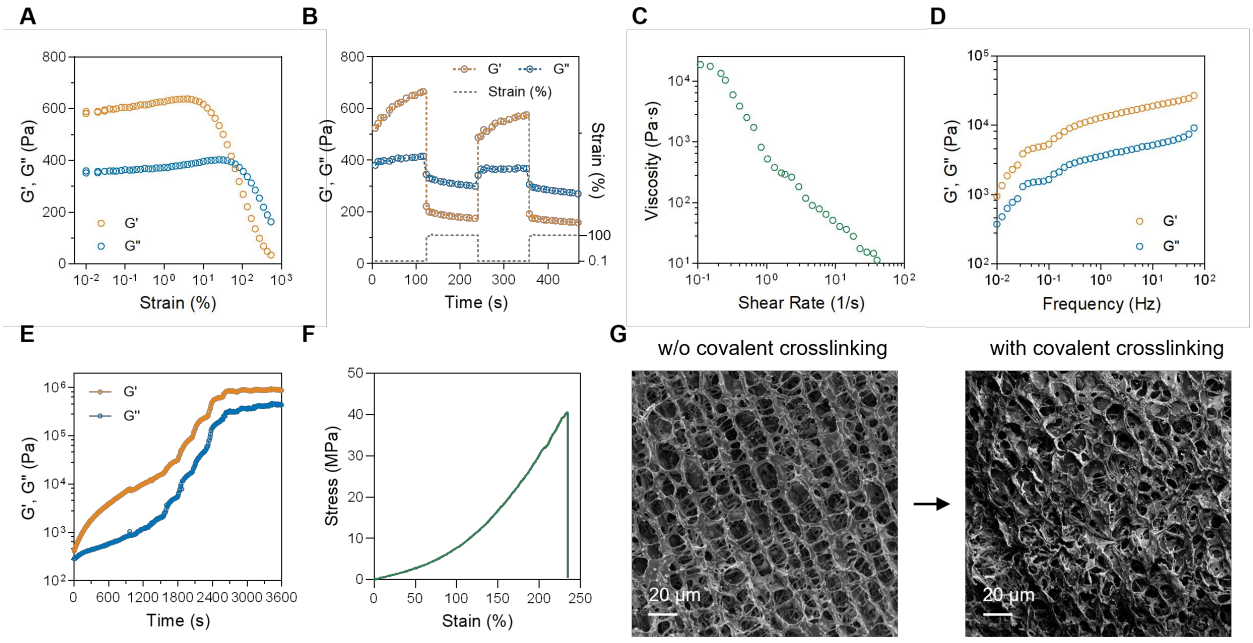

Figure 3.3 | Characterization of the DCN hydrogel.

A series of rheological studies (**A-D**) were performed to investigate the viscoelastic properties of the hydrogel without covalent crosslinking by measuring the storage moduli (G') and loss moduli (G"). (**A**) The strain sweep (strain: 0.01% - 500%, frequency: 0.1 Hz, 37 ^{o}C) suggests that the G' exceeded G" at small strains, indicating dominant elastic behavior. As the strain increased, G' and G" decreased, eventually intersecting at a crossover strain (51.9%), and beyond this strain, G" exceeded G', indicating a dominant viscous response. (**B**) Recovery of the hydrogel under alternating high and low strain conditions (100% strain and 0.1% strain (right Y-axis), frequency: 0.1 Hz, 37 ^{o}C) was studied, which demonstrated the capability of the hydrogel to recover its stability and integrity after injection. (**C**) The shear rate sweep reveals the viscosity of the hydrogel decreased as the shear rate increased, demonstrating its shear-thinning behavior before in situ

covalent crosslinking; (**D**) The frequency sweep (0.01 – 63.1 Hz, strain: 0.1%, 37 ^{o}C) indicates viscoelastic solid-like behavior of the hydrogel. (**E**) The in situ covalent crosslinking kinetics of the DCN hydrogel at 37 ^{o}C was studied by measuring the changes of G' and G". Both G' and G" of the DCN hydrogel were gradually increased over time and the increments reached plateaus after ~45 min, indicating complete thiol-ene reactions. (**F**) The mechanical behavior of the DCN hydrogel was investigated by measuring the stress-strain curve. (**G**) The microstructures of the hydrogel without and with covalent crosslinking were observed by SEM. Scale bar: 20 μm.

3.2.3 The DCN hydrogel efficiently induced blood coagulation and possessed good radiopacity and biocompatibility.

The DCN hydrogel was designed capable of efficiently inducing blood coagulation. Its major components, Alg-MA and CMC-MA, are both hydrophilic and anionic polysaccharides that can initiate surface-contact activation of the blood zymogen Factor XII, and thus lead to blood coagulation [59]. Moreover, the incorporation of calcium ions in the matrix of the DCN hydrogel further accelerates hemostasis by catalyzing multiple steps in the hemostasis cascade. The hemostatic capability of the DCN hydrogel was evaluated by monitoring the clotting time of human whole blood after contact with DCN hydrogel surfaces in a 96-well plate (**Figure 3.4A**). Notably, blood treated with the DCN hydrogel clotted within the first minute upon contact, while blood treated with physiological saline (0.9% NaCl) was clotted after 6 minutes. The hemostatic capability of the DCN hydrogel was further compared with clinically applied embolic agents for endovascular embolization, including Onyx^{TM}, an FDA-approved dimethyl sulfoxide solution of ethylene vinyl-alcohol copolymer with micronized tantalum powder, and metallic coils (**Figure**

3.4A). Onyx™ did not induce any observable hemostasis, due to its lack of components for hemostasis cascade activation. Metallic coils, on the other hand, successfully induced blood coagulation within 2 minutes after treatment, taking a longer time than the DCN hydrogel. In addition, the DCN hydrogel and Onyx™ did not induce hemolysis of red blood cells, in comparison with ultrapure water (positive control) and saline (negative control) (**Figure 3.4B**).

Radiopacity is an important property for embolic materials because endovascular surgery requires X-ray imaging for real-time tracking for accurate deployment and preventing dangerous non-target embolization [35]. Iohexol (product name: Omnipaque™), an FDA-approved and currently clinically used water-soluble contrast agent for X-ray imaging, was mixed in the DCN hydrogel at 21 wt%. The radiopacity of the DCN hydrogel was then evaluated by an X-ray inspection system. Under X-ray, the DCN hydrogel exhibited 85.6% radiopacity relative to the abdominal stent graft (**Figure 3.4C**), as quantified by the greyscale of the pixels in the X-ray imaging (**Figure 3.4D**).

The in vitro biocompatibility of the DCN hydrogel was assessed in vitro using NIH 3T3 fibroblast cells and cell counting kit-8 (CCK-8) (**Figure 3.4E**). Cells treated with solutions of Alg-MA, CMC-MA, or $CaSO_4$ did not show any significant reduction in cell viability. Cells seeded and cultured on the plate coated with covalently crosslinked DCN hydrogel did not exhibit any sign of cytotoxicity either, indicating excellent biocompatibility of DCN hydrogel.

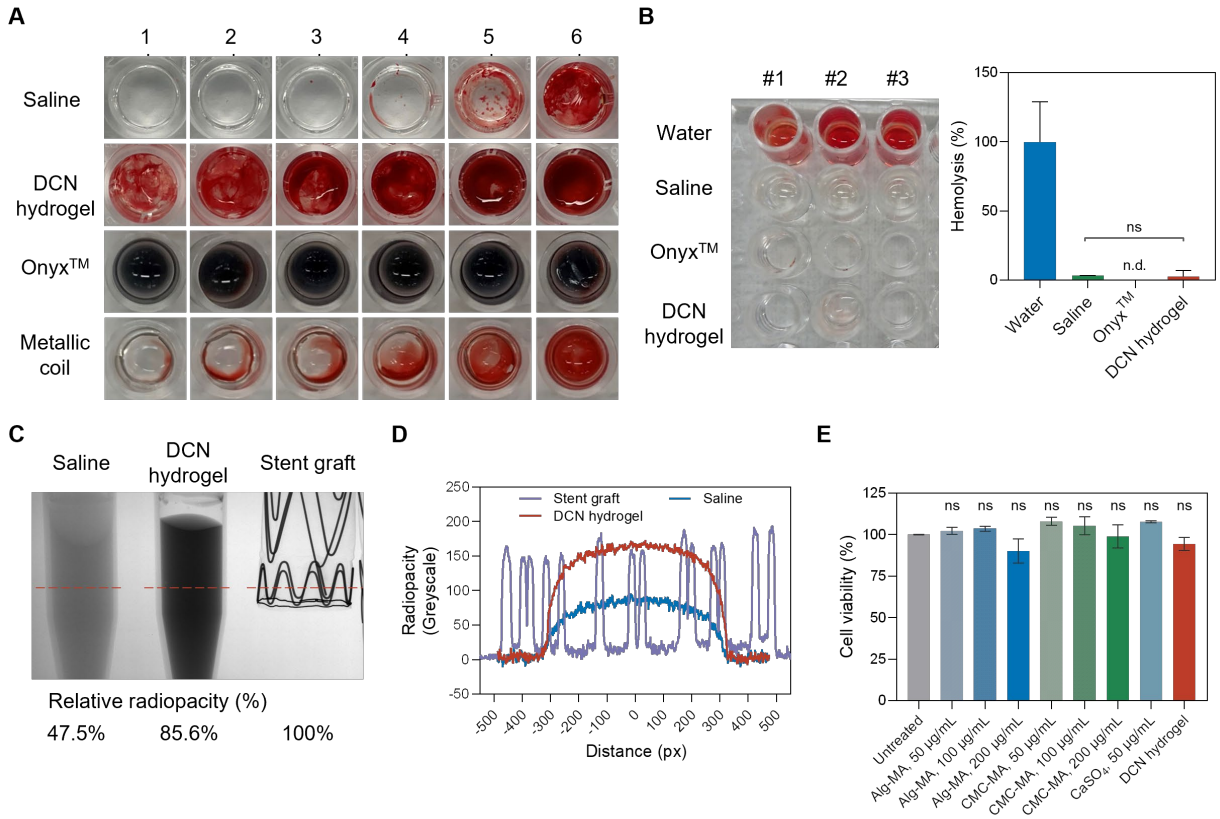

Figure 3.4 | The hemostasis, hemolysis, radiopacity and biocompatibility of the DCN hydrogel.

(**A**) Blood clot formation in contact with commercially available embolic agents (Onyx™ and metallic coils), DCN hydrogel and saline (0.9% NaCl) as a function of time (n = 3). (**B**) Hemolysis of human red blood cells in the presence of commercially available embolic agents (Onyx™), DCN hydrogel and PBS (n=3). (**C, D**) Radiopacity of saline (in a 1.7-mL Eppendorf tube, negative control), DCN hydrogel (loaded with 21 wt% Iohexol, in a 1.7-mL Eppendorf tube) and a metallic stent graft (positive control), measured by (**C**) X-ray images followed by (**D**) quantitative analysis. (**E**) The cell viability of the components used to form DCN hydrogel (Alg-MA, CMC-MA and $CaSO_4$) and DCN hydrogel on NIH 3T3 fibroblasts. Statistical significance was calculated via one-way ANOVA with a Tukey's post hoc test. ns, not significant. n.d., not detected.

3.2.4 The DCN hydrogel effectively embolized arteries and induced tissue fibrosis and regeneration in rabbits.

The in vivo endovascular embolization efficacy of the DCN hydrogel was tested in a rabbit model. The femoral artery of rabbit (n = 3) was embolized by the DCN hydrogel, Onyx^{TM}, and saline as a control, respectively (**Figure 3.5A, B**). The efficacy of arterial occlusion was analyzed 1, 7, and 28 days after surgery. The morphological character of the treated artery was assessed by H&E staining and Masson's trichrome staining (**Figure 3.5C, D** and **Table 3.1, 3.2**). Onyx^{TM} appeared as black color in both the H&E and Masson's trichrome staining images while the DCN hydrogel appeared as light purple color in the H&E staining images and light blue color in the Masson's trichrome staining images. Both Onyx^{TM} and the DCN hydrogel induced complete occlusion of the targeted artery on Day 1, 7, and 28. On Day 1, both Onyx^{TM} and the DCN hydrogel showed luminal occlusion with associated thrombosis (**Figure 3.5C**), while the saline group showed patency of the lumen. Moreover, Masson's trichrome staining indicated minimal to no fibrosis within the occluded lumen in both Onyx^{TM} and DCN hydrogel groups (**Figure 3.5D**). On Day 7, sustained thrombosis of the lumen was induced in both Onyx^{TM}- and DCN hydrogel-treated arteries, whereas patency of the lumen was found in the saline group. On Day 28, more fibrotic changes were found in the DCN hydrogel-treated artery than the Onyx^{TM}-treated one, which indicate the transition from material-based occlusion to fibrotic occlusion of the arterial lumen after 28 days. In contrast, the saline group exhibited patency of the lumen with marked intimal hyperplasia.

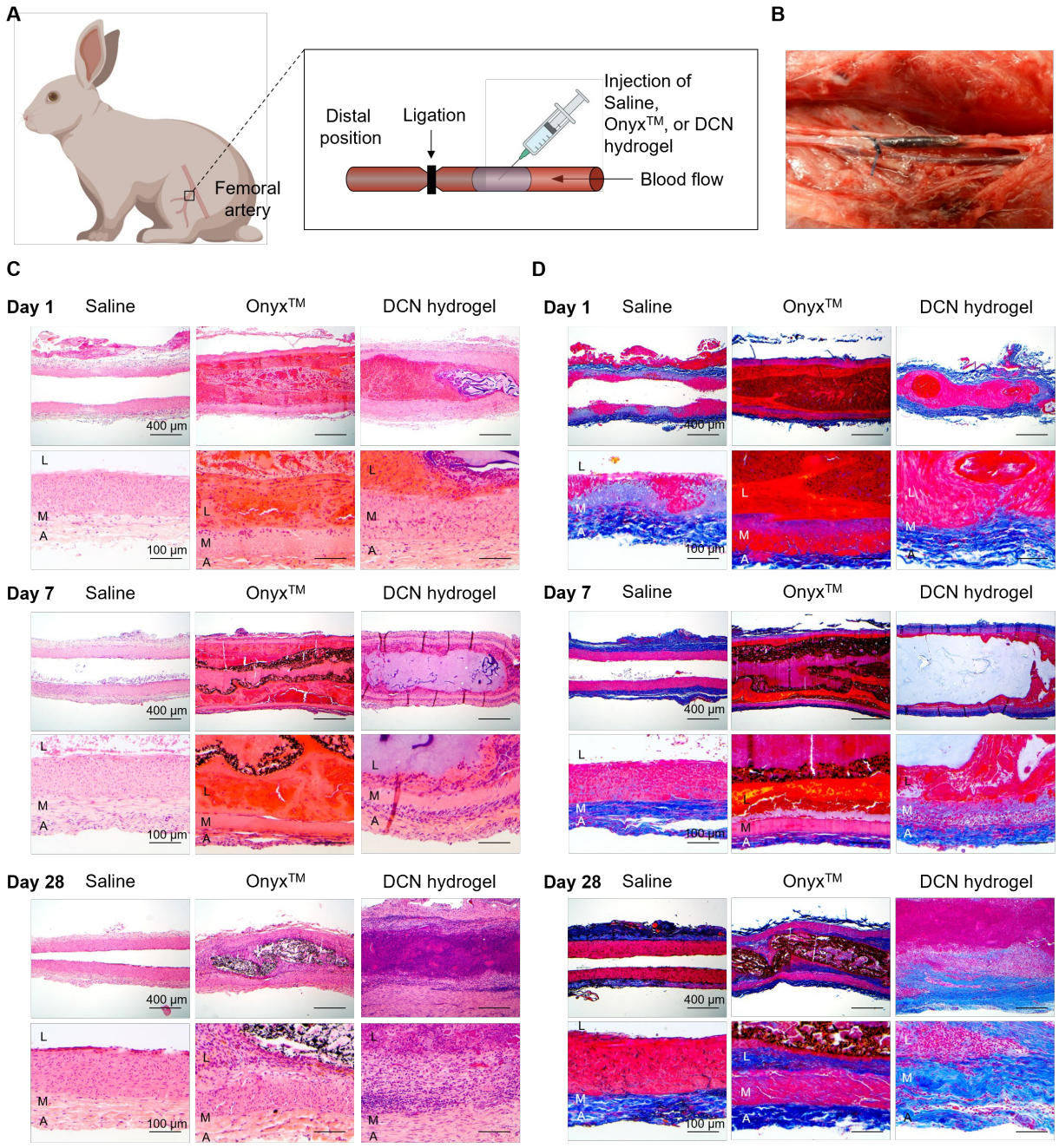

Figure 3.5 | H&E and Masson's trichrome staining results of the embolized rabbit arteries.

(**A**) Schematic representation of the rabbit arterial occlusion model. (**B**) Representative pictures of the DCN hydrogel injected artery after embolization. (**C**) H&E staining and (**D**) Masson's trichrome staining were performed, respectively, to evaluate the artery embolization efficacy.

Sections were collected from the arteries injected with saline, Onyx™ or DCN hydrogel in a rabbit model at different time point (n = 3 for each time point) post-treatment. Onyx™ was shown as black spots. The DCN hydrogel was shown as light purples in H&E staining and light purple in Masson's trichrome staining. Scale bars: 400 μm (low magnification, 5x) and 100 μm (high magnification, 20 x). Lumen (L), media (M), and adventitia (A) were labeled. Low magnification images of the DCN hydrogel group on Day 28 are presented in **Figure 3.13**.

Immunohistochemical analyses of the treated arteries are shown in **Figure 3.6** and **Table 3.3**. Inflammatory changes, cell proliferation, and cell apoptosis were analyzed by immunohistochemical staining of MAC387, PCNA, and TUNEL, respectively (n = 3). Acute inflammation was found in both Onyx™ and DCN hydrogel groups on Day 1 and Day 7, but the inflammatory response was decreased on Day 28. The activation of macrophages by the DCN hydrogel can be attributed to the polysaccharide components, as indicated by the in vitro study (**Figure 3.11**). Proliferative changes in the DCN hydrogel group were seen on Day 7 and Day 28, with cellular component-based luminal occlusion. In contrast, in the Onyx™ group, luminal occlusion was mostly induced by the embolic material itself, with minimal cellular components observed. TUNEL staining demonstrated similar apoptotic activity in the medial and adventitial layers in all three groups on Day 1 and Day 7. On Day 28, apoptotic activities were similar in the saline and Onyx™ group but were decreased to almost none in the DCN hydrogel group.

Collectively, the DCN hydrogel group showed acute occlusion of the treated artery and induced a continuous increase in collagen with cellular proliferation, which are histological characteristics of the luminal occlusion/narrowing by the intimal hyperplasia of the artery [60-62]. In the clinical

setting, recanalization of the treated artery and aneurysm is a major concern [63, 64], especially after the endovascular treatment of the large artery, like an aortic aneurysm [65]. The DCN hydrogel group showed both acute thrombosis of the targeted artery and delayed fibrotic changes with continued occlusion by the cellular component. At a later stage, successful embolization was achieved and maintained mostly by fibrous tissue, not by the DCN hydrogel. Together with the injectability and in situ covalent crosslinking capability of the DCN hydrogel which enables its deployment in the target artery including large cavity without the fear of distal micro-embolization of catheter entrapment, the DCN hydrogel is promising to be used as a preferred material for vascular embolization.

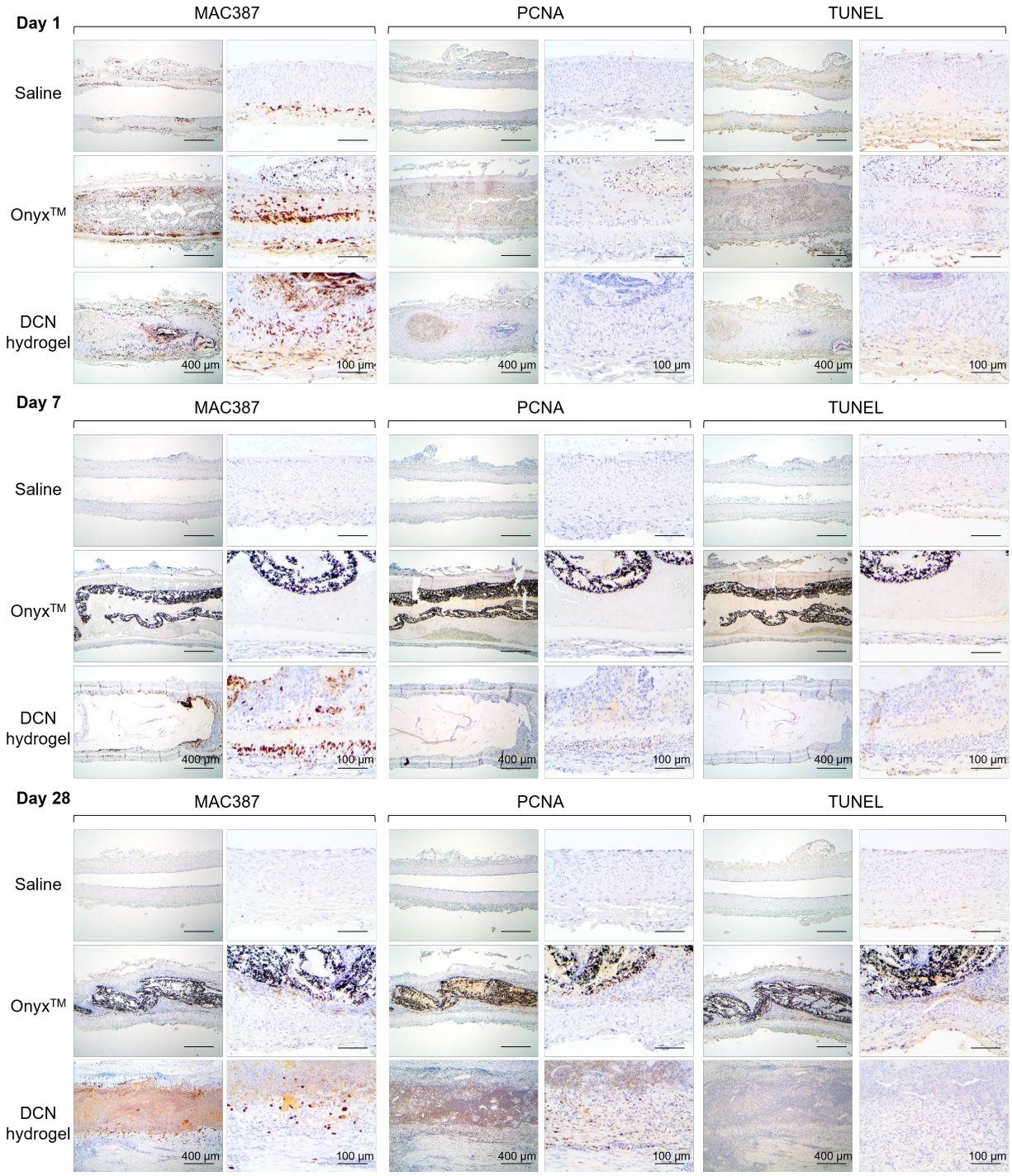

Figure 3.6 | Immunohistochemistry staining of the embolized rabbit arteries.

Immunohistochemistry staining was performed to assay macrophages (MAC387), proliferating cells (PCNA) and cell apoptosis (TUNEL) in the treated arteries, respectively. Sections were

collected from the arteries injected with saline, Onyx^{TM} and DCN hydrogel in a rabbit model at different time point (n = 3 for each time point) post-treatment. Scale bars: 400 μm (low magnification, 5x) and 100 μm (high magnification, 20 x). Low magnification images of the DCN hydrogel group on Day 28 are presented in **Figure 3.12**.

3.3 Conclusions

In this work, we developed and evaluated a dual-crosslinking network hydrogel (DCN hydrogel) for permanent endovascular embolization. The hydrogel was formed by two sequential gelling process: the initial reversible alginate-calcium crosslinking process ensuring injectability and hydrogel immobilization at the injection site followed by the secondary in situ covalent crosslinking through thiol-ene Michael-addition reaction under physiological condition to further strengthen the mechanical and chemical stability. The DCN hydrogel possesses a number of desirable features as a promising embolic material, including hemostasis inducing capability, visibility under X-ray, and good biocompatibility. Our in vivo study revealed that the DCN hydrogel can effectively and completely embolized femoral arteries in rabbits, not only by the DCN hydrogel itself, but also by inducing cell proliferation and tissue fibrosis with minimal cell apoptosis. Collectively, the DCN hydrogel provides a viable, biocompatible, and cost-effective alternative to existing embolic materials with clinical translation potential for endovascular embolization.

3.4 Methods

3.4.1 Synthesis of AMA·HCl.

2-Aminoethyl methacrylate hydrochloride (AMA·HCl) was synthesized using a previously reported protocol (**Figure 3.7A**) [66]. Ethanolamine hydrochloride (13.0 g, 0.13 mol), methacryloyl chloride (20.0 mL, 0.19 mol), and hydroquinone (0.13 g, 1.2 mmol, as an inhibitor to avoid polymerization) were added to a three-necked round bottomed flask fitted with a condenser. Ethanolamine hydrochloride salt was melted at 95 °C under nitrogen for 1 h, and the reaction was maintained at 70 °C for 2 h. Hydrogen chloride gas formed during the reaction was neutralized with 1M NaOH aqueous solution connected to the flask. The crude product was cooled to 40 °C, diluted with tetrahydrofuran (12.5 mL), and precipitated into *n*-pentane (100 mL). The resulting creamy white precipitate was isolated by centrifugation at 1,000 x g, washed thoroughly with ice-cold *n*-pentane (100 mL), and dried under vacuum. The crude product was then recrystallized twice using a 7:3 ethyl acetate/isopropanol mixture. The purified product AMA·HCl was dried under vacuum and characterized by ^{1}H-NMR (deuterium oxide, 400 MHz, **Figure 3.7B**).

3.4.2 Synthesis of alginate methacrylate (Alg-MA).

Alg-MA was synthesized through an amidation reaction (**Figure 3.8A**) [67]. In brief, sodium alginate (2.50 g, 12.5 mmol or 1 equiv. of carboxyl groups) was dissolved in 50 mM MES buffer (pH = 6.0) containing 0.5 M NaCl to yield a 1 wt% solution. EDC·HCl (1.20 g, 0.5 equiv.) and NHS (0.36 g, 0.25 equiv.) were introduced into the mixture. After 5 min, AMA·HCl (0.52 g, 0.25 equiv.) was added to the solution and the reaction was stirred at 20 ºC for 24 h. Thereafter, the mixture was dialyzed against ultrapure water (molecular weight cut-off, MWCO = 12-14 kDa) for

3 days, filtered through a 0.22-μm membrane and finally lyophilized. The purified product Alg-MA was characterized by ^{1}H-NMR (deuterium oxide, 400 MHz, **Figure 3.8B**).

3.4.3 Synthesis of carboxymethylcellulose methacrylate (CMC-MA).

CMC-MA was prepared through the conventional methacrylic anhydride route (**Figure 3.9A**) [55]. CMC (2.50 g, 6.3 mmol or 1 equiv. of β-hydroxyl groups) was dissolved in 125 mL ultrapure water and cooled on ice to yield a 2 wt% solution. The pH was adjusted to ~9.0 by adding 6 g (10 equiv.) sodium carbonate and 5M NaOH aqueous solution. Methacrylic anhydride (8.30 mL, 10 equiv. of total β-hydroxyl groups) was added to the solution and the pH was maintained around pH 8.0 by adding a certain amount of 5M NaOH aqueous solution. The reaction was carried out at room temperature with vigorous stirring for 12 hours. The modified CMC was precipitated with 500 mL of acetone to remove the remaining methacrylic anhydride and other byproducts. The precipitate was collected and rehydrated in ultrapure water, dialyzed against ultrapure water (MWCO = 12-14 kDa) for 3 days, filtered through a 0.22-μm membrane and finally lyophilized. The purified product CMC-MA was characterized by ^{1}H-NMR (deuterium oxide, 400 MHz, **Figure 3.9B**).

3.4.4 Preparation of dual-crosslinking network (DCN) hydrogels.

Two steps were involved for the preparation of DCN hydrogel: (1) the formation of injectable hydrogels, and (2) the addition of in situ covalent crosslinking reagents. First, the lyophilized Alg-MA and CMC-MA were dissolved in 50 mM triethanolamine buffer (pH = 8.5) by mechanical stirring at 100 rpm for 24 h. A slurry contains 240 mg/mL $CaSO_4 \cdot 2H_2O$ ($CaSO_4 \cdot 2H_2O$/Alg-MA = 1/5, wt/wt) was added dropwise into the polymer solution, and mechanically stirred for another 24 h. The resulting injectable hydrogel was collected for storage at 4 ^{o}C. Second, the in situ covalent

crosslinking reagents were added to the injectable hydrogel prior to animal injections. Specifically, DTT (100 mg/mL, final DTT/methacrylate groups = 1/1, mol/mol) and TCEP (100 mg/mL, final concentration at 2.5 mM in the DCN hydrogel) solutions were added to the injectable hydrogels. The hydrogel was thoroughly mixed by a spatula and adjusted to pH 8.5 by adding an appropriate amount of 2M NaOH solution. The mixture was then loaded into a Luer-Lok syringe using a spatula or syringe plunger and warmed at 37 ºC before injections.

3.4.5 Rheology.

All rheological measurements were performed using an AR2000 rheometer (TA instruments) with an environmental test chamber to maintain the temperature at 37 ºC, following reported protocols [32, 68]. All hydrogel samples were cast between a 25-mm diameter stainless steel upper plate and a lower Peltier plate with the gap between plates at 1.0 mm for all measurements. Examination of the hydrogel without in situ covalent crosslinking was performed by oscillatory strain sweeps (1.0 Hz, 0.1-500% strain), and frequency sweeps (0.01-63 Hz, 0.5% strain, in the linear viscoelastic region). The shear rate sweep was conducted to study the shear-thinning behavior. Thixotropic test was performed at 1.0 Hz under strain oscillation between 0.1 % for 2 minutes and 100 % for 2 minutes. For the DCN hydrogel undergoing in situ covalent crosslinking, the crosslinking kinetics was observed *in situ* via time sweeps (1.0 Hz, 0.1% strain).

3.4.6 Tensile test

The DCN hydrogel was cast in a dumbbell-shaped (ASTM D638 Type V) mold at 37ºC overnight. The tensile tests were carried out using a pre-tension of 0.1 N and an extension rate of 5.0 mm sec^{-1} (Instron, 5848, 10 N load cell). Young's modulus, elongation at break, and ultimate tensile strength were recorded.

3.4.7 Injectability.

The DCN hydrogel was loaded into a 1-mL or 3-mL Luer-Lok syringes (BD Biosciences) using a spatula or syringe plunger before injections. Several types of needles (BD Biosciences) and a 6-French catheter (Cook Medical LLC) were connected to the syringe, respectively. The injection forces were measured by Instron testing machines. The injection flow rates were set at 0.1 mL/min or 1 mL/min.

3.4.8 Scanning electron microscopy (SEM).

An SEM (Zeiss LEO 1530-1) was used to visualize the hydrogel microstructures with or without in situ covalent crosslinking. The hydrogel without in situ covalent crosslinking was prepared following the procedure used to prepare the DCN hydrogel but without the addition of DTT and TCEP. The DCN hydrogel was prepared and incubated at 37 ºC overnight to allow covalent crosslinking. Thereafter, hydrogel samples were flash-frozen in liquid nitrogen, cut into small pieces, and subsequently lyophilized (<0.1 mBar, and -80 °C, Labconco). The cross-sections of the lyophilized samples were then sputter-coated with 7 nm gold (Leica EM ACE600) and observed by SEM.

3.4.9 Swelling behavior.

The DCN hydrogel was prepared at 37 ºC overnight in an incubator for covalent crosslinking. The resulting hydrogel sample was cut into pieces (~ 5 x 5 x 3 mm in size). The hydrogel pieces were weighed and placed into 2 mL centrifuge tubes containing1 mL of DPBS 1X. Thereafter, the centrifuge tubes with the hydrogel samples were stored at 37 ºC. After certain periods, the swollen samples were taken out from the tube, and the water on the sample surface was carefully removed by a filter paper. Finally, the swollen samples were weighed to quantify the swelling ratios, defined

as:

$$\text{Swelling (\%)} = \frac{\text{m (samples)} - \text{m(original)}}{\text{m(original)}} \times 100\%$$

where *m* stands for the mass of the samples.

3.4.10 Cell culture.

NIH 3T3 fibroblasts were cultured at 37 ºC in a 5% CO_2 atmosphere with the Dulbecco's Modified Eagle Medium (Thermo Fisher Scientific) supplemented with 10% (v/v) fetal bovine serum (Thermo Fisher Scientific) and 1% (v/v) Penicillin-Streptomycin (Thermo Fisher Scientific). RAW 264.7 macrophages were cultured at 37 ºC in a 5% CO_2 atmosphere with the RPMI 1640 Medium (Thermo Fisher Scientific) supplemented with 10% (v/v) fetal bovine serum (Thermo Fisher Scientific) and 1% (v/v) Penicillin-Streptomycin (Thermo Fisher Scientific).

3.4.11 Cell viability.

To study the cell viability of the various hydrogel components, NIH 3T3 fibroblasts were seeded in 96-well plates (10,000 cells per well) in 100 μL of cell culture media 24 h prior to treatments. On the day of treatments, Alg-MA, CMC-MA, and $CaSO_4 \cdot 2H_2O$ dissolved/suspended in PBS were added to the cells at different concentrations, respectively. After 1 day of incubation, Cell Counting Kit-8 (CCK-8, Dojindo Molecular Technologies, Inc.) was used to quantify cell viability following the manufacturer's protocol, and the cells were further incubated at 37 ºC for 48 h. Thereafter, the absorbance of culture media in each well was measured at 450 nm using a microplate reader system (Promega Corporation), and the average absorbance and percentage of cell viability were calculated.

For hydrogel samples, 50 μL of the DCN hydrogel was first injected to the bottom of a well in a

96-well plate. The plate was then centrifuged at 300 x g for 10 min to ensure even distribution of hydrogel at the well bottom, and the DCN hydrogel was fully crosslinked at 37 ºC overnight in an incubator. Then, 10 uL of neutralized human whole blood was added to the top surface of the hydrogel. After blood clotted, the hydrogel surface was thoroughly rinsed with DPBS 1X. Cell seeding and CCK-8 treatments were carried out following the same procedures described above. The supernatant of cell culture media in the hydrogel-coated well was transferred to an empty well and subsequently, the absorbance at 450 nm was measured using a microplate reader system (Promega Corporation).

3.4.12 TNF-α assay.

RAW264.7 macrophages were seeded 24 h prior to treatments in 96-well plates at 10,000 cells per well with or without hydrogel-coated wells, following the aforementioned protocol. On the day of treatments, Alg-MA (200 μg/mL), CMC-MA (200 μg/mL), and $CaSO_4 \cdot 2H_2O$ (50 μg/mL) dissolved or suspended in PBS were added to the cell culture media, respectively. After 24 h of incubation, the cell culture media were collected. TNF-α level in the culture media was analyzed using an enzyme-linked immunosorbent assay (ELISA, R&D Systems, MTA00B) following the manufacturer's protocol.

3.4.13 In vitro hemostasis test.

The hemostasis test was conducted based on a previously reported protocol with some modifications [69]. Human whole blood containing sodium citrate (16.65 mM) as an anticoagulant was used for this study. The citrated blood was neutralized by mixing the blood with $CaCl_2$ solution (224.79 mM) at a 9/1 (vol/vol) ratio. The mixture was then vortexed for 10 s right before the test. Thereafter, 0.12 mL of the neutralized blood and 0.04 ml of the samples (for the saline, DCN

hydrogel and Onyx groups) or 0.04 cm^3 metallic coils (diameter = 2mm, length = 12.7 mm, Boston Scientific Interlock™ Fibered IDCTM, 2mm/4cm) were added into the wells in a 96-well plate. At different time points after treatments, the supernatant in each well was aspirated and the well was rinsed with PBS three times. The remaining blood clots, adhering to the bottom of the well, were then observed to evaluate the hemostatic capability of each group.

3.4.14 In vitro hemolysis test

Red blood cells were separated from the human whole blood by centrifugation at 2,500 rpm for 10 min. The separated cells were washed with PBS three times and re-suspended in PBS. For testing the hemolysis of materials, 0.1 mL of the cell suspension was mixed with 0.2 mL of ultrapure water, PBS, Onyx, and DCN hydrogel, respectively. The mixture was then incubated at 37 ºC for 3 h. The supernatant was collected by centrifugation at 2,500 rpm for 10 min and mixed with Drabkin's reagent at a ratio of 1/1 (vol/vol). Thereafter, the absorbance at 540 nm was measure by UV-Vis spectrometer and the hemolysis rate was finally calculated as:

$$\text{Hemolysis (\%)} = \frac{\text{Absorbance (Sample)} - \text{Absorbance (PBS)}}{\text{Absorbance (Ultrapure water)} - \text{Absorbance (PBS)}} \times 100\%$$

3.4.15 Radiopacity study.

The radiopacity of the DCN hydrogel was studied using X-ray inspection system μnRay 7600f (Matsusada Precision Inc.) with an output voltage at 90 kV and power at 18 W. Physiological saline and an abdominal metallic stent graft (GORE® EXCLUDER® AAA Endoprosthesis, W. L. Gore & Associates, Inc.) were used as references.

3.4.16 Animals.

All animal experiments were performed following the biosafety protocol and the animal protocol

approved by Kawasumi Laboratories, Inc. Japanese white rabbits (male and female, body weight 2.0 – 3.0 kg, Slc:JW/CSK, supplied by Japan SLC, Inc.) were randomly divided into 9 groups (3 treatments (i.e., saline, Onyx or DCN hydrogel) x 3 time points (i.e., 1 day, 1 week and 1 month); n = 3 per group and thus 27 rabbits total for this study) for the following experiments.

In vivo femoral arterial embolization in a rabbit model: On the day of treatments, rabbits were intravenously injected with Vetorphale (0.5 mg/kg) for pain-relief. The anesthesia was initiated through animal anesthesia mask with 4% - 5% isoflurane and maintained through tracheal intubation with 2% - 3% isoflurane. The neck and thigh of the animal were shaved, fixed, and disinfected. Thereafter, the animal was transfused with Ringer's lactate solution through auricular vein (1 droplet/2s) and intravenously injected with heparin (150 units/kg). For material injections, the femoral artery of the animal was first exposed, and the blood flow was stopped by clipping the distal position of the artery. Saline, Onyx or DCN hydrogel was then injected, respectively. After certain time points (i.e., 1 day, 1 week and 1 month), autopsy of the animal was performed. The animal was intravenously injected with Vetorphale and anesthetized by isoflurane as aforementioned. The left ventricle was thoracotomically punctured and circulated with physiological saline and 4% paraformaldehyde, respectively. The treated artery was then collected and preserved in 4% paraformaldehyde for histological analysis.

3.4.17 Histology Studies.

Artery samples were embedded into paraffin blocks, sectioned, and stained with hematoxylin and eosin (H&E) and Masson's trichrome, respectively. For immunohistochemical staining, macrophages were stained with primary antibodies (MAC387, Abcam, ab22506) and secondary antibodies (Nichirei Biosciences, 414171). Proliferating cells were stained with primary antibodies

(PCNA, Dako, M0879) and secondary antibodies (Nichirei Biosciences, 414171). Apoptotic cells were stained with ApopTag® Peroxidase In Situ Apoptosis Detection Kit (Sigma-Aldrich, S7100). All staining procedures followed the manufacturers' protocols.

3.4.18 Statistical analysis.

Results are presented as mean ± standard deviation. Statistical differences between experimental groups were analyzed using a one-way ANOVA test followed by Tukey's post hoc comparison test. Statistical analyses were performed using GraphPad Prism software. Significant differences between groups were indicated by * $p < 0.05$, ** $p < 0.01$, *** $p < 0.001$ and **** $p < 0.0001$, respectively. $p \geq 0.05$ was considered to be not statistically significant in all analyses (95% confidence level).

3.5 Supplementary Figures

A

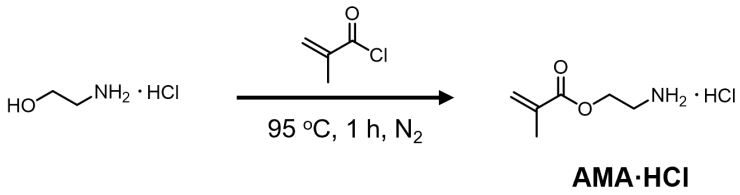

B

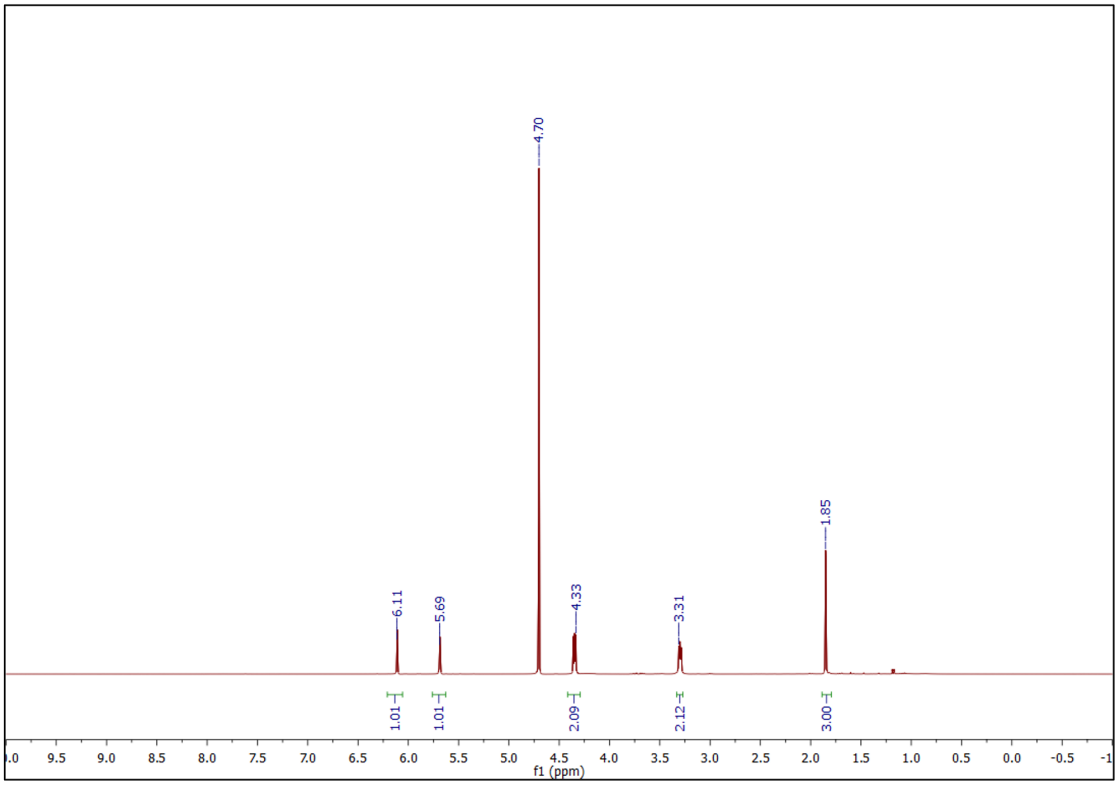

Figure 3.7 | Synthesis and characterization of 2-aminoethyl methacrylate hydrochloride (AMA·HCl).

(**A**) Synthesis scheme of AMA·HCl. (**B**) 1H-NMR spectrum of AMA·HCl.

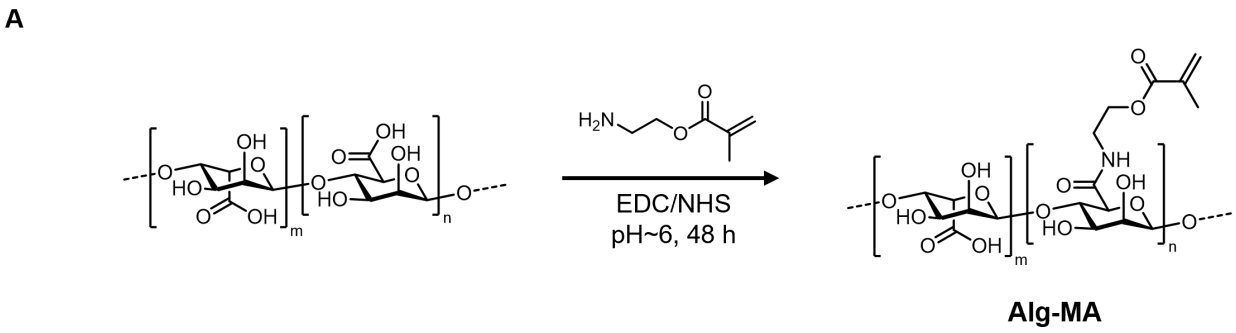

Figure 3.8 | Synthesis and characterization of alginate methacrylate (Alg-MA).

(**A**) Synthesis scheme of Alg-MA. (**B**) 1H-NMR spectrum of Alg-MA. The degree of methacrylate substitution in Alg-MA was characterized as 27%.

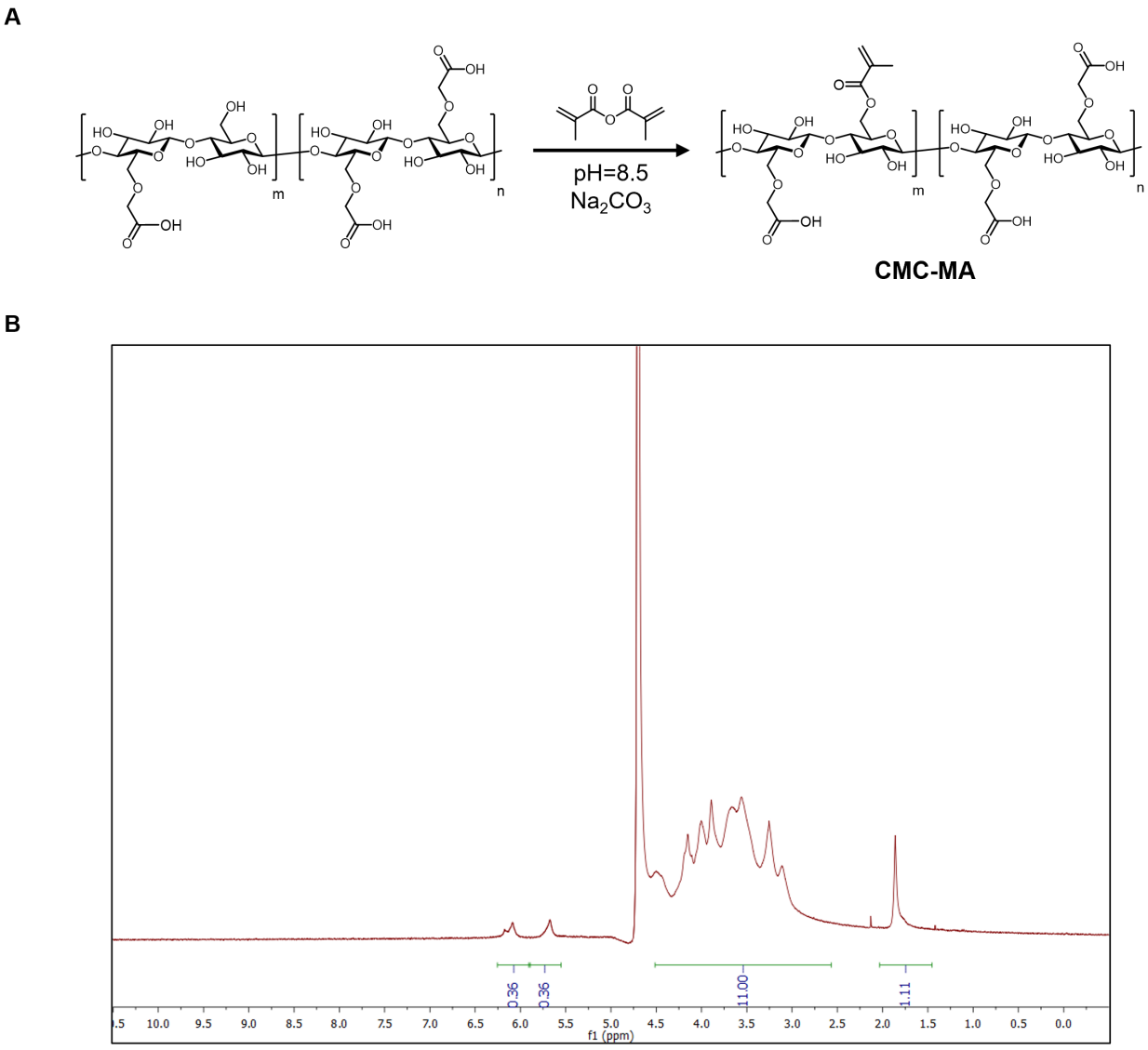

Figure 3.9 | Synthesis and characterization of carboxymethylcellulose methacrylate (CMC-MA).

(**A**) Synthesis scheme of CMC-MA. (**B**) 1H-NMR spectrum of CMC-MA. The degree of methacrylate substitution in Alg-MA was characterized as 18%.

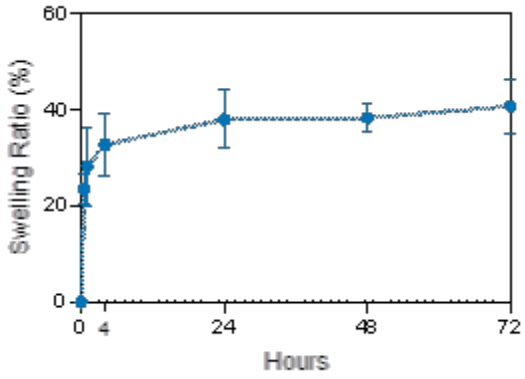

Figure 3.10 | The swelling behavior of the DCN hydrogel.

The swelling of the DCN hydrogel was limited to < 40 wt% at 37 ºC in 1X DPBS due to the dually crosslinked network.

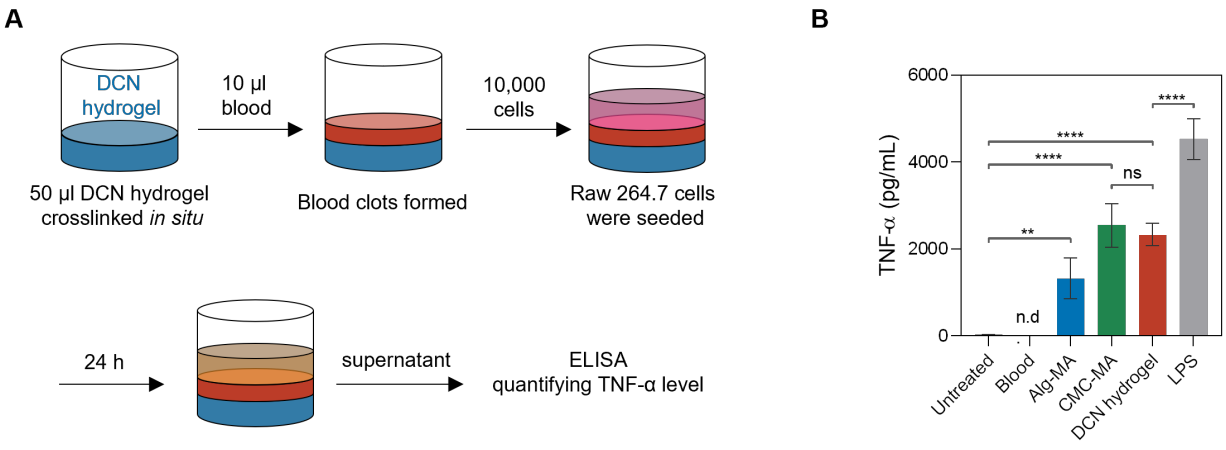

Figure 3.11 | TNF-α activation by the DCN hydrogel in Raw 264.7 macrophages.

(**A**) Schematic illustration of the method used to quantify TNF-α activation. (**B**) The TNF-α expression level quantified by ELISA. LPS (1 ng/mL) was used as a positive control. Statistical significance was calculated via one-way ANOVA with Tukey's post hoc test. ** $P < 0.01$. **** $P < 0.0001$. ns, not significant. n.d., not detected. LPS, lipopolysaccharides.

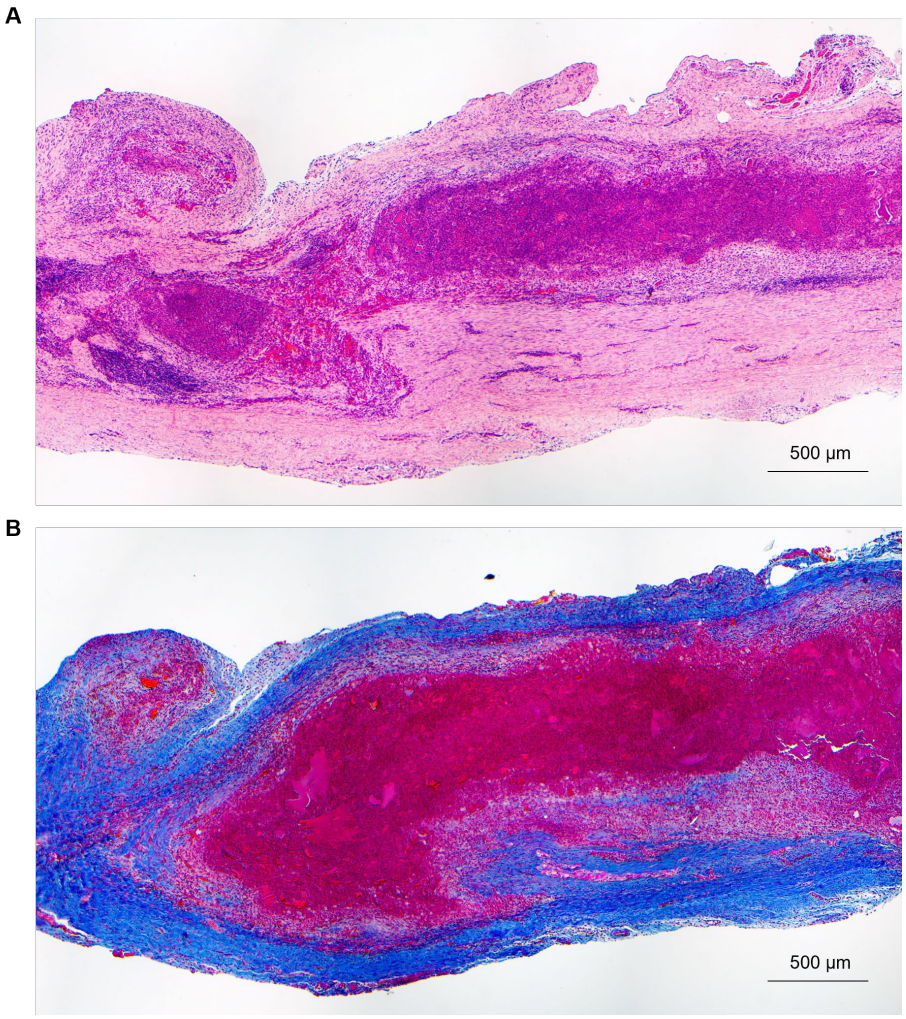

Figure 3.12 | H&E and Masson's trichrome staining results of the rabbit arteries embolized by the DCN hydrogel for 28 days.

(**A**) H&E staining; (**B**) Masson's trichrome staining.

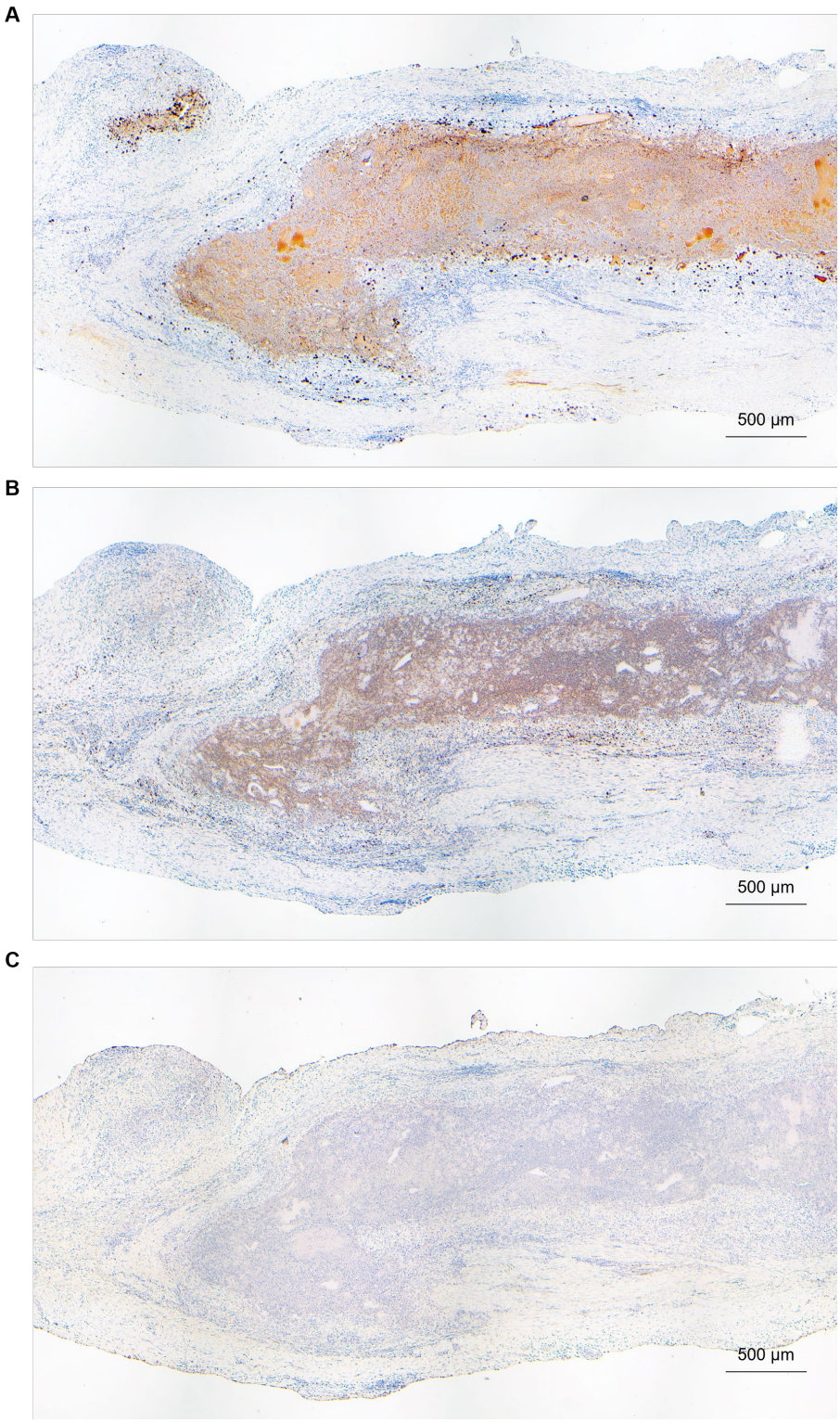

Figure 3.13 | Immunohistochemistry staining of the rabbit arteries embolized by the DCN hydrogel for 28 days.

(**A**) Macrophages were stained by MAC387; (**B**) Proliferating cells were stained by PCNA; (**C**) Apoptotic cells were stained by TUNEL.

3.6 Supplementary Tables

Table 3.1 | Assessment of the H&E staining results

Group	Saline			Onyx^{TM}			DCN hydrogel		
Period	Day 1	Day 7	Day 28	Day 1	Day 7	Day 28	Day 1	Day 7	Day 28
Blood clotting	3	0	0	3	3	0	3	3	0
Organized thrombus	0	1	3	0	0	3	0	1	3
Collection/infiltration of pseudo-eosinophil	1	0	0	2	1	1	2	2	1
Lymphocyte infiltration	0	0	1	0	1	1	0	0	3
Increasing macrophage	0	1	1	0	0	3	0	2	3
Foreign body giant cells	0	0	0	0	0	3	0	0	2
Necrosis of vessel wall	2	0	0	3	3	0	1	2	0
Cell debris	0	0	0	2	1	0	0	0	3
Fibrous tissue proliferation (fibrosis), thickening of vessel wall	0	3	3	0	0	1	0	0	3

0: none; 1: mild; 2: moderate; 3: high

Table 3.2 | Assessment of the Masson's trichrome staining results

Group	Saline			Onyx™			DCN hydrogel		
Period	Day 1	Day 7	Day 28	Day 1	Day 7	Day 28	Day 1	Day 7	Day 28
Fibrous tissue proliferation (fibrosis), thickening of vessel wall	0	4	4	0	1	3	0	2	4

0: none; 1: slight; 2: mild; 3: moderate; 4: high

Table 3.3 | Assessment of the immunohistochemistry staining results

Group	Saline			Onyx™			DCN hydrogel		
Period	Day 1	Day 7	Day 28	Day 1	Day 7	Day 28	Day 1	Day 7	Day 28
MAC387, macrophage	3	1	0	4	3	0	4	3	2
PCNA, proliferating cells	1	1	1	2	3	3	2	2	3
TUNEL, apoptotic cells	1	1	1	0	0	0	1	0	0

0: none; 1: slight; 2: mild; 3: moderate; 4: high

Chapter 4. Conclusion and Future Perspectives

In this dissertation, two types of biomaterials were developed for in vivo genome editing and endovascular embolization, respectively.

For in vivo genome editing, the pH-responsive amphiphilic polymer, mPEG-PC7A, was developed to encapsulate CRISPR-Cas9 RNP with or without ssODN, through a straightforward preparation process, and form NHEJ-NP and HDR-NP at the optimal pH conditions. Both NHEJ-NP and HDR-NP offer a safe and efficient approach for both in vitro and in vivo (via both local or systemic administration) genome editing and possess good biocompatibility and low immunogenicity. Particularly, the therapeutic efficacy of HDR-NP for treating Duchenne muscular dystrophy was also demonstrated. After intramuscular administration, HDR-NP effectively restored the expression of dystrophin and thus improved the muscle strength of diseased mice. NHEJ-NP and HDR-NP are easy to produce and can be conveniently stored, thus they are of great interest for various in vitro and in vivo genome editing applications with clinical translation potentials. Future work will focus on further optimization of this nanosystem by tailoring the polymer chemical structures to enhance its editing efficiency. In addition, aside from livers and muscles, the in vivo editing efficiency of NHEJ-NP or HDR-NP in other organs or tissues will be explored by taking the advantage of the chemical versatility in ligand conjugation. The potential of re-engineering this nanosystem for delivery of other genome editors, including CRISPR-Cas12, Cas13, and base editor systems, will be investigated as well.

For endovascular embolization, a dual-crosslinking network hydrogel (DCN hydrogel) was developed and evaluated. The DCN hydrogel was formed by two sequential gelling process: the initial reversible alginate-calcium crosslinking process ensuring injectability and hydrogel

immobilization at the injection site followed by the secondary in situ covalent crosslinking through thiol-ene Michael-addition reaction under physiological condition to further strengthen the mechanical and chemical stability. The DCN hydrogel possesses a number of desirable features as a promising embolic material, including hemostasis inducing capability, visibility under X-ray, and good biocompatibility. Our in vivo study revealed that the DCN hydrogel can effectively and completely embolized femoral arteries in rabbits, not only by the DCN hydrogel itself, but also by inducing cell proliferation and tissue fibrosis with minimal cell apoptosis. Collectively, the DCN hydrogel provides a viable, biocompatible, and cost-effective alternative to existing embolic materials with clinical translation potential for endovascular embolization. Future work will focus on further optimization of this hydrogel system in terms of the mechanical behavior and covalent crosslinking kinetics, by tuning the methacrylate substitution degree on polymers. Besides, the long-term embolization (e.g., 3 months and 1 year) efficacy induced by the DCN hydrogel will be explored. The potential of clinical translation of the DCN hydrogel will be further assessed in a large animal model (e.g., porcine model).

References

[1] M. Jinek, K. Chylinski, I. Fonfara, M. Hauer, J.A. Doudna, E. Charpentier, A Programmable Dual-RNA–Guided DNA Endonuclease in Adaptive Bacterial Immunity, Science 337(6096) (2012) 816-821.

[2] L. Cong, F.A. Ran, D. Cox, S. Lin, R. Barretto, N. Habib, P.D. Hsu, X. Wu, W. Jiang, L.A. Marraffini, F. Zhang, Multiplex Genome Engineering Using CRISPR/Cas Systems, Science 339(6121) (2013) 819-823.

[3] P. Mali, L. Yang, K.M. Esvelt, J. Aach, M. Guell, J.E. DiCarlo, J.E. Norville, G.M. Church, RNA-Guided Human Genome Engineering via Cas9, Science 339(6121) (2013) 823-826.

[4] G.J. Knott, J.A. Doudna, CRISPR-Cas guides the future of genetic engineering, Science 361(6405) (2018) 866-869.

[5] A.V. Anzalone, L.W. Koblan, D.R. Liu, Genome editing with CRISPR–Cas nucleases, base editors, transposases and prime editors, Nat. Biotechnol. 38(7) (2020) 824-844.

[6] C. Xue, E.C. Greene, DNA Repair Pathway Choices in CRISPR-Cas9-Mediated Genome Editing, Trends Genet. 37(7) (2021) 639-656.

[7] C.D. Yeh, C.D. Richardson, J.E. Corn, Advances in genome editing through control of DNA repair pathways, Nat. Cell Biol. 21(12) (2019) 1468-1478.

[8] G. Chen, A.A. Abdeen, Y. Wang, P.K. Shahi, S. Robertson, R. Xie, M. Suzuki, B.R. Pattnaik, K. Saha, S. Gong, A biodegradable nanocapsule delivers a Cas9 ribonucleoprotein complex for in vivo genome editing, Nat. Nanotechnol. 14(10) (2019) 974-980.

[9] M. Wang, J.A. Zuris, F.T. Meng, H. Rees, S. Sun, P. Deng, Y. Han, X. Gao, D. Pouli, Q. Wu, I. Georgakoudi, D.R. Liu, Q. Xu, Efficient delivery of genome-editing proteins using bioreducible lipid nanoparticles, Proc. Natl. Acad. Sci. U.S.A. 113(11) (2016) 2868-2873.

[10] R. Mout, M. Ray, G. Yesilbag Tonga, Y.-W. Lee, T. Tay, K. Sasaki, V.M. Rotello, Direct Cytosolic Delivery of CRISPR/Cas9-Ribonucleoprotein for Efficient Gene Editing, ACS Nano 11(3) (2017) 2452-2458.

[11] W. Sun, W. Ji, J.M. Hall, Q. Hu, C. Wang, C.L. Beisel, Z. Gu, Self-Assembled DNA Nanoclews for the Efficient Delivery of CRISPR–Cas9 for Genome Editing, Angew. Chem. Int. Ed. Engl. 54(41) (2015) 12029-12033.

[12] S.K. Alsaiari, S. Patil, M. Alyami, K.O. Alamoudi, F.A. Aleisa, J.S. Merzaban, M. Li, N.M. Khashab, Endosomal Escape and Delivery of CRISPR/Cas9 Genome Editing Machinery Enabled by Nanoscale Zeolitic Imidazolate Framework, J. Am. Chem. Soc. 140(1) (2018) 143-146.

[13] C. Xu, Z. Lu, Y. Luo, Y. Liu, Z. Cao, S. Shen, H. Li, J. Liu, K. Chen, Z. Chen, Targeting of NLRP3 inflammasome with gene editing for the amelioration of inflammatory diseases, Nat. Commun. 9(1) (2018) 4092.

[14] S. Tong, B. Moyo, C.M. Lee, K. Leong, G. Bao, Engineered materials for in vivo delivery of genome-editing machinery, Nat. Rev. Mater. 4 (2019) 726-737.

[15] K. Lee, M. Conboy, H.M. Park, F. Jiang, H.J. Kim, M.A. Dewitt, V.A. Mackley, K. Chang, A. Rao, C. Skinner, T. Shobha, M. Mehdipour, H. Liu, W.-c. Huang, F. Lan, N.L. Bray, S. Li, J.E. Corn, K. Kataoka, J.A. Doudna, I. Conboy, N. Murthy, Nanoparticle delivery of Cas9 ribonucleoprotein and donor DNA in vivo induces homology-directed DNA repair, Nat. Biomed. Eng. 1 (2017) 889-901.

[16] R. Shahbazi, G. Sghia-Hughes, J.L. Reid, S. Kubek, K.G. Haworth, O. Humbert, H.-P. Kiem, J.E. Adair, Targeted homology-directed repair in blood stem and progenitor cells with CRISPR nanoformulations, Nat. Mater. 18(10) (2019) 1124-1132.

[17] Y. Rui, D.R. Wilson, J. Choi, M. Varanasi, K. Sanders, J. Karlsson, M. Lim, J.J. Green, Carboxylated branched poly(β-amino ester) nanoparticles enable robust cytosolic protein delivery and CRISPR-Cas9 gene editing, Sci. Adv. 5(12) (2019) eaay3255.

[18] Y. Wang, P.K. Shahi, R. Xie, H. Zhang, A.A. Abdeen, N. Yodsanit, Z. Ma, K. Saha, B. Pattnaik, S. Gong, A pH-responsive silica–metal–organic framework hybrid nanoparticle for the delivery of hydrophilic drugs, nucleic acids, and CRISPR-Cas9 genome-editing machineries, J. Control. Release 324 (2020) 194-203.

[19] P. Yang, S.-J. Chou, J. Li, W. Hui, W. Liu, N. Sun, R.Y. Zhang, Y. Zhu, M.-L. Tsai, H.I. Lai, M. Smalley, X. Zhang, J. Chen, Z. Romero, D. Liu, Z. Ke, C. Zou, C.-F. Lee, S.J. Jonas, Q. Ban,

P.S. Weiss, D.B. Kohn, K. Chen, S.-H. Chiou, H.-R. Tseng, Supramolecular nanosubstrate–mediated delivery system enables CRISPR-Cas9 knockin of hemoglobin beta gene for hemoglobinopathies, Sci. Adv. 6(43) (2020) eabb7107.

[20] Y. Wang, B. Ma, A.A. Abdeen, G. Chen, R. Xie, K. Saha, S. Gong, Versatile Redox-Responsive Polyplexes for the Delivery of Plasmid DNA, Messenger RNA, and CRISPR-Cas9 Genome-Editing Machinery, ACS Appl. Mater. Interfaces 10(38) (2018) 31915-31927.

[21] A. England, R. Mc Williams, Endovascular aortic aneurysm repair (EVAR), Ulster Med. J. 82(1) (2013) 3.

[22] K.C. Kent, Abdominal aortic aneurysms, N. Engl. J. Med. 371(22) (2014) 2101-2108.

[23] J.E. Lopera, Embolization in trauma: principles and techniques, Semin. Interv. Radiol. 27(01) (2010) 014-028.

[24] S. Vaidya, K.R. Tozer, J. Chen, An overview of embolic agents, Semin. Interv. Radiol. 25(03) (2008) 204-215.

[25] J. Hu, H. Albadawi, B.W. Chong, A.R. Deipolyi, R.A. Sheth, A. Khademhosseini, R. Oklu, Advances in Biomaterials and Technologies for Vascular Embolization, Adv. Mater. 31(33) (2019) e1901071.

[26] Q. Guo, J. Zhao, Y. Ma, B. Huang, D. Yuan, Y. Yang, X. Du, A meta-analysis of translumbar embolization versus transarterial embolization for type II endoleak after endovascular repair of abdominal aortic aneurysm, J. Vasc. Surg. 71(3) (2020) 1029-1034 e1.

[27] Q. Li, P. Hou, Sac Embolization and Side Branch Embolization for Preventing Type II Endoleaks After Endovascular Aneurysm Repair: A Meta-analysis, J. Endovasc. Ther. 27(1) (2020) 109-116.

[28] C. Mascoli, A. Freyrie, M. Gargiulo, E. Gallitto, R. Pini, G. Faggioli, C. Serra, C. De Molo, A. Stella, Selective Intra-procedural AAA sac Embolization During EVAR Reduces the Rate of Type II Endoleak, Eur. J. Vasc. Endovasc. Surg. 51(5) (2016) 632-9.

[29] C. Marcelin, Y. Le Bras, F. Petitpierre, D. Midy, E. Ducasse, N. Grenier, F. Cornelis, Safety and efficacy of embolization using Onyx((R)) of persistent type II endoleaks after abdominal endovascular aneurysm repair, Diagn. Interv. Imaging 98(6) (2017) 491-497.

[30] G. Calugi, W. Dorigo, A. Capone, D. Esposito, E. Giacomelli, C. Pratesi, Acute limb ischemia due to ONYX 34 migration during embolization of a traumatic pseudoaneurysm of the superficial femoral artery, J. Surg. Case Rep. 2021(6) (2021) rjab231.

[31] A. Arat, B.E. Cil, I. Vargel, B. Turkbey, M. Canyigit, B. Peynircioglu, Y.O. Arat, Embolization of high-flow craniofacial vascular malformations with onyx, AJNR Am. J. Neuroradiol. 28(7) (2007) 1409-14.

[32] R.K. Avery, H. Albadawi, M. Akbari, Y.S. Zhang, M.J. Duggan, D.V. Sahani, B.D. Olsen, A. Khademhosseini, R. Oklu, An injectable shear-thinning biomaterial for endovascular embolization, Sci. Transl. Med. 8(365) (2016) 365ra156.

[33] B. Liu, Z. Xu, H. Gao, C. Fan, G. Ma, D. Zhang, M. Xiao, B. Zhang, Y. Yang, C. Cui, T. Wu, X. Feng, W. Liu, Stiffness Self-Tuned Shape Memory Hydrogels for Embolization of Aneurysms, Adv. Funct. Mater. 30(22) (2020) 1910197.

[34] L. Fan, M. Duan, Z. Xie, K. Pan, X. Wang, X. Sun, Q. Wang, W. Rao, J. Liu, Injectable and Radiopaque Liquid Metal/Calcium Alginate Hydrogels for Endovascular Embolization and Tumor Embolotherapy, Small 16(2) (2020) e1903421.

[35] J. Hu, I. Altun, Z. Zhang, H. Albadawi, M.A. Salomao, J.L. Mayer, L. Hemachandra, S. Rehman, R. Oklu, Bioactive-Tissue-Derived Nanocomposite Hydrogel for Permanent Arterial Embolization and Enhanced Vascular Healing, Adv. Mater. 32(33) (2020) e2002611.

[36] H. Albadawi, I. Altun, J. Hu, Z. Zhang, A. Panda, H.J. Kim, A. Khademhosseini, R. Oklu, Nanocomposite Hydrogel with Tantalum Microparticles for Rapid Endovascular Hemostasis, Adv. Sci. 8(1) (2020) 2003327.

[37] I. Altun, J. Hu, H. Albadawi, Z. Zhang, M.A. Salomao, J.L. Mayer, L. Jamal, R. Oklu, Blood-Derived Biomaterial for Catheter-Directed Arterial Embolization, Adv. Mater. 32(52) (2020) e2005603.

[38] D.N. Nguyen, T.L. Roth, P.J. Li, P.A. Chen, R. Apathy, M.R. Mamedov, L.T. Vo, V.R. Tobin, D. Goodman, E. Shifrut, J.A. Bluestone, J.M. Puck, F.C. Szoka, A. Marson, Polymer-stabilized Cas9 nanoparticles and modified repair templates increase genome editing efficiency, Nat. Biotechnol. 38(1) (2020) 44-49.

[39] H. Nishimasu, F.A. Ran, Patrick D. Hsu, S. Konermann, Soraya I. Shehata, N. Dohmae, R. Ishitani, F. Zhang, O. Nureki, Crystal Structure of Cas9 in Complex with Guide RNA and Target DNA, Cell 156(5) (2014) 935-949.

[40] K. Zhou, Y. Wang, X. Huang, K. Luby-Phelps, B.D. Sumer, J. Gao, Tunable, Ultrasensitive pH-Responsive Nanoparticles Targeting Specific Endocytic Organelles in Living Cells, Angew. Chem. Int. Ed. Engl. 50(27) (2011) 6109-6114.

[41] M. Luo, H. Wang, Z. Wang, H. Cai, Z. Lu, Y. Li, M. Du, G. Huang, C. Wang, X. Chen, M.R. Porembka, J. Lea, A.E. Frankel, Y.-X. Fu, Z.J. Chen, J. Gao, A STING-activating nanovaccine for cancer immunotherapy, Nat. Nanotechnol. 12(7) (2017) 648-654.

[42] J.E. Chung, S. Tan, S.J. Gao, N. Yongvongsoontorn, S.H. Kim, J.H. Lee, H.S. Choi, H. Yano, L. Zhuo, M. Kurisawa, J.Y. Ying, Self-assembled micellar nanocomplexes comprising green tea catechin derivatives and protein drugs for cancer therapy, Nat. Nanotechnol. 9(11) (2014) 907-912.

[43] H.-X. Wang, Z. Song, Y.-H. Lao, X. Xu, J. Gong, D. Cheng, S. Chakraborty, J.S. Park, M. Li, D. Huang, L. Yin, J. Cheng, K.W. Leong, Nonviral gene editing via CRISPR/Cas9 delivery by membrane-disruptive and endosomolytic helical polypeptide, Proc. Natl. Acad. Sci. U.S.A. 115(19) (2018) 4903-4908.

[44] E.M.M. MANDERS, F.J. VERBEEK, J.A. ATEN, Measurement of co-localization of objects in dual-colour confocal images, J. Microsc. 169(3) (1993) 375-382.

[45] J. Benesty, J. Chen, Y. Huang, I. Cohen, Pearson correlation coefficient, Noise reduction in speech processing, Springer2009, pp. 1-13.

[46] B.T. Staahl, M. Benekareddy, C. Coulon-Bainier, A.A. Banfal, S.N. Floor, J.K. Sabo, C. Urnes, G.A. Munares, A. Ghosh, J.A. Doudna, Efficient genome editing in the mouse brain by local delivery of engineered Cas9 ribonucleoprotein complexes, Nat. Biotechnol. 35(5) (2017) 431-434.

[47] C. Long, J.R. McAnally, J.M. Shelton, A.A. Mireault, R. Bassel-Duby, E.N. Olson, Prevention of muscular dystrophy in mice by CRISPR/Cas9–mediated editing of germline DNA, Science 345(6201) (2014) 1184-1188.

[48] Patrick D. Hsu, Eric S. Lander, F. Zhang, Development and Applications of CRISPR-Cas9 for Genome Engineering, Cell 157(6) (2014) 1262-1278.

[49] C.T. Charlesworth, P.S. Deshpande, D.P. Dever, J. Camarena, V.T. Lemgart, M.K. Cromer, C.A. Vakulskas, M.A. Collingwood, L. Zhang, N.M. Bode, M.A. Behlke, B. Dejene, B. Cieniewicz, R. Romano, B.J. Lesch, N. Gomez-Ospina, S. Mantri, M. Pavel-Dinu, K.I. Weinberg, M.H. Porteus, Identification of preexisting adaptive immunity to Cas9 proteins in humans, Nat. Med. 25(2) (2019) 249-254.

[50] H.H. Gustafson, D. Holt-Casper, D.W. Grainger, H. Ghandehari, Nanoparticle uptake: the phagocyte problem, Nano today 10(4) (2015) 487-510.

[51] Q. Cheng, T. Wei, L. Farbiak, L.T. Johnson, S.A. Dilliard, D.J. Siegwart, Selective organ targeting (SORT) nanoparticles for tissue-specific mRNA delivery and CRISPR–Cas gene editing, Nat. Nanotechnol. 15(4) (2020) 313-320.

[52] S. Liu, Q. Cheng, T. Wei, X. Yu, L.T. Johnson, L. Farbiak, D.J. Siegwart, Membrane-destabilizing ionizable phospholipids for organ-selective mRNA delivery and CRISPR–Cas gene editing, Nat. Mater. (2021).

[53] A. Aartsma-Rus, M. van Putten, Assessing functional performance in the mdx mouse model, J. Vis. Exp. (85) (2014) 51303.

[54] C.B. Rodell, J.W. MacArthur, S.M. Dorsey, R.J. Wade, L.L. Wang, Y.J. Woo, J.A. Burdick, Shear-Thinning Supramolecular Hydrogels with Secondary Autonomous Covalent Crosslinking to Modulate Viscoelastic Properties In Vivo, Adv. Funct. Mater. 25(4) (2015) 636-644.

[55] C.B. Rodell, N.N. Dusaj, C.B. Highley, J.A. Burdick, Injectable and Cytocompatible Tough Double-Network Hydrogels through Tandem Supramolecular and Covalent Crosslinking, Adv. Mater. 28(38) (2016) 8419-8424.

[56] J.-Y. Sun, X. Zhao, W.R.K. Illeperuma, O. Chaudhuri, K.H. Oh, D.J. Mooney, J.J. Vlassak, Z. Suo, Highly stretchable and tough hydrogels, Nature 489(7414) (2012) 133-136.

[57] A.B. Lowe, Thiol-ene “click” reactions and recent applications in polymer and materials synthesis, Polym. Chem. 1(1) (2010) 17-36.

[58] M.H. Chen, L.L. Wang, J.J. Chung, Y.-H. Kim, P. Atluri, J.A. Burdick, Methods To Assess Shear-Thinning Hydrogels for Application As Injectable Biomaterials, ACS Biomater. Sci. Eng. 3(12) (2017) 3146-3160.

[59] E. Sanfins, C. Augustsson, B. Dahlback, S. Linse, T. Cedervall, Size-dependent effects of nanoparticles on enzymes in the blood coagulation cascade, Nano Lett. 14(8) (2014) 4736-44.

[60] S. Franco, A. Stranz, F. Ljumani, G. Urabe, M. Chaudhary, D. Stewart, V.S. Pilli, M. Kelly, D. Yamanouchi, K.C. Kent, B. Liu, Role of FOXM1 in vascular smooth muscle cell survival and neointima formation following vascular injury, Heliyon. 6(6) (2020) e04028.

[61] D. Yamanouchi, H. Banno, M. Nakayama, M. Sugimoto, H. Fujita, M. Kobayashi, H. Kuwano, K. Komori, Hydrophilic statin suppresses vein graft intimal hyperplasia via endothelial cell-tropic Rho-kinase inhibition, J. Vasc. Surg. 42(4) (2005) 757-64.

[62] J. Shen, J.B. Song, J. Fan, Z. Zhang, Z.J. Yi, S. Bai, X.L. Mu, Y.B. Yang, L. Xiao, Distribution and Dynamic Changes in Matrix Metalloproteinase (MMP)-2, MMP-9, and Collagen in an In Stent Restenosis Process, Eur. J. Vasc. Endovasc. Surg. 61(4) (2021) 648-655.

[63] I. Rezek, G. Mousan, Z. Wang, M.H. Murad, D.F. Kallmes, Coil type does not affect angiographic follow-up outcomes of cerebral aneurysm coiling: a systematic review and meta-analysis, AJNR Am. J. Neuroradiol. 34(9) (2013) 1769-73.

[64] Z. Serafin, P. Strześniewski, W. Lasek, W. Beuth, Methods and time schedule for follow-up of intracranial aneurysms treated with endovascular embolization: a systematic review, Neurol. Neurochir. Pol. 45(5) (2011) 421-30.

[65] Q. Guo, X. Du, J. Zhao, Y. Ma, B. Huang, D. Yuan, Y. Yang, G. Zeng, F. Xiong, Prevalence and risk factors of type II endoleaks after endovascular aneurysm repair: A meta-analysis, PLoS One 12(2) (2017) e0170600.

[66] L. He, E.S. Read, S.P. Armes, D.J. Adams, Direct synthesis of controlled-structure primary amine-based methacrylic polymers by living radical polymerization, Macromolecules 40(13) (2007) 4429-4438.

[67] O. Jeon, K.H. Bouhadir, J.M. Mansour, E. Alsberg, Photocrosslinked alginate hydrogels with tunable biodegradation rates and mechanical properties, Biomaterials 30(14) (2009) 2724-34.

[68] C. Loebel, C.B. Rodell, M.H. Chen, J.A. Burdick, Shear-thinning and self-healing hydrogels as injectable therapeutics and for 3D-printing, Nat. Protoc. 12(8) (2017) 1521-1541.

[69] A.K. Gaharwar, R.K. Avery, A. Assmann, A. Paul, G.H. McKinley, A. Khademhosseini, B.D. Olsen, Shear-thinning nanocomposite hydrogels for the treatment of hemorrhage, Acs Nano 8(10) (2014) 9833-42.